Development and Optimization of Metal to Polymer Friction Stir Welded Joints

Beatriz Margarida Gaspar Ribeiro

Thesis to obtain the Master of Science Degree in

Mechanical Engineering

Supervisors: Prof. Virgínia Isabel Monteiro Nabais Infante
Eng. Arménio Neves Correia

Examination Committee

Chairperson: Prof. Luís Filipe Galrão dos Reis

Supervisor: Prof. Virgínia Isabel Monteiro Nabais Infante

Member of the Committee: Prof. Inês da Fonseca Pestana Ascenso Pires

July 2024

Declaration

I declare that this document is an original work of my own authorship and that it fulfills all the requirements of the Code of Conduct and Good Practices of the Universidade de Lisboa.

To those who persevere.

Acknowledgments

First and foremost, I would like to sincerely thank my supervisors, Professor Virginia Infante, and Arménio Correia, for the guidance, availability, and support you provided during the development of this work. Your knowledge and trust in my work gave me the confidence to ask questions and think beyond what was in front of me. Thank you for always being there to answer those questions. I am profoundly grateful that I had the opportunity to learn and work under your guidance.

Thank you for the projects, SMARTWAGONS C644940527-00000048 and PRODUTECH R3- ”Agenda Mobilizadora da Fileira das Tecnologias de Produção para a Reindustrialização” C645808870 – 00000067, and the scholarship, BI 08.PL692.2023.IDMEC, which ultimately allowed me to develop this work and further my academic endeavors.

I would also like to express my appreciation to the Institute of Science and Innovation in Mechanical and Industrial Engineering, especially to UMAI, for allowing me to bring to fruition the experimental work that was the basis of this project. Thank you to the team who received me and treated me like I already belonged, I will forever remember your generosity and helpfulness (especially the matrecos games).

I am eternally grateful to my family, without whom I would have never gotten to this point. To my brother and sister, thank you for always being there, no matter what, thank you for listening to me going on and on about whatever plagued my thoughts. Thank you for your kind words and firm corrections, you were my compass during this challenge and my comfort when everything was chaos. Thank you for loving me and never letting go. And thank you for giving me a primah for life (saúde e paz, o resto...).

And since we all know that IST is a team sport, I am profoundly grateful to all those who appeared in my path. To my elderly friends (specially Braz) who welcomed me into this university and the course that would become my home, thank you. To my *Djéssicas*, Alice and Mangas, who began this path by my side, and who are always in my thoughts despite the distance, thank you. To Sem Espigas, Martim, Alfredo, Careca, Miguel, Matias, Rita, and Valença, thank you for being by my side through most of this journey, through good times and the bad, I was able to grow by your side. And finally, to my little ones, Matilde, Luisa, Ana, Vitorino, Luis, and Festas, thank you for putting up with this crazy old lady.

To my dance girlies, my deepest appreciation, during these last few months, your kind words and warm hugs gave me solace and kept me focused on what truly mattered.

To my childhood friends, Madalena, Carolina, Teresa, Mariana, Tomás, Guimi, Miguel, Junior, and Benny, who were always there and accompanied me through every growing pain, my sincerest thank you. Even just seeing each other every blue moon gave me the knowledge that you would always be there for me, and brought me the comfort I so dreadfully needed in the most lonely moments.

And lastly, to myself, thank you so much for not quitting when everything was dark, and for keeping your chin high with every punch. The future holds endless possibilities. You deserve them.

Resumo

Dada a crescente necessidade de soluções mais leves, ecológicas e económicas, no setor dos transportes, engenheiros defendem a utilização de estruturas dissimilares inovadoras, que combinem materiais como ligas metálicas e polímeros/compósitos. No entanto, a união de materiais com propriedades dissimilares é um desafio. Tecnologias baseadas na fricção, incluindo Friction Stir Welding (FSW), oferecem vantagens distintas aos métodos tradicionais, como fixação mecânica ou por adesivo, e apresentam resultados promissores. Neste trabalho, foram produzidas juntas sobrepostas dissimilares entre um polímero reforçado com fibra de vidro (NORYL^{TM}) e uma liga de alumínio (AA6082-T6) utilizando FSW. Utilizou-se a metodologia Central Composite Design (CCD) para avaliar a resistência mecânica e a temperatura de processamento das juntas fabricadas, e analisar os principais efeitos, interações e influência dos parâmetros de processamento, nomeadamente, a velocidade de rotação e de soldadura e o ângulo de inclinação da ferramenta. Realizou-se análises sobre a temperatura de processamento, a resistência à tração, as macro e microestruturas, e a dureza das juntas, resultando num modelo estatístico. Por meio de um modelo de elementos finitos, determinou-se o fator de flexão do momento secundário e estudou-se o seu efeito na eficiência das juntas. A resistência mecânica das juntas variou entre 1698.20 ± 17.29 N e 3414.17 ± 317.15 N, atingindo uma eficiência máxima de junta de 84.55%, enquanto a temperatura de processamento variou entre 203.6±10.7°C e 277.0±25.4°C. Foi previsto um conjunto de parâmetros ótimo com velocidade de rotação de 1136 rpm, velocidade de soldadura de 154 mm/min e ângulo de inclinação de 1.7°, onde a resistência mecânica média atingida foi de 2645.24±232.14 N e a eficiência da junta foi de 69.78%.

Palavras-chave: Soldadura por Fricção Linear, Materiais Dissimilares, Juntas Sobrepostas, Temperatura de Processamento, Resistência Mecânica, Central Composite Design.

Abstract

Amidst the growing need for lighter, environmentally friendly, and cost-effective solutions in the transportation sector, engineers are adopting innovative dissimilar structures, combining materials like metal alloys and polymers/composites. However, joining dissimilar materials in multi-material structures poses an engineering challenge due to inherent property disparities. Friction stir-based technologies, including Friction Stir Welding (FSW), are showing promising results and offer advantages over traditional joining methods (mechanical fastening and adhesive bonding). In this work, overlap dissimilar joints were produced between a glass fiber-reinforced polymer (NORYL^{TM}) and an aluminum alloy (AA6082-T6), using FSW. A Central Composite Design (CCD) methodology was defined, to comprehensively evaluate the joints' mechanical strength and processing temperature and analyse the main effects, interactions, and influence of the processing parameters, namely, rotational speed, welding speed, and tool tilt angle. Analysis of the processing temperature and tensile strength resulted in a statistical model. The macro and microstructures, and hardness of the joints were also studied. The bending factor of the secondary bending moment was determined using a finite elements model (FEM) and its effect on the joint's efficiency was studied. The joints' mechanical strength ranged from 1698.20±17.29 N to 3414.17±317.15 N, with a maximum joint efficiency of 84.55%. The processing temperature was between 203.6±10.7°C and 277.0±25.4°C. The predicted optimal set of parameters encompassed a rotational speed of 1136 rpm, welding speed of 154 mm/min, and tilt angle of 1.7°. The joints fabricated with this set of parameters exhibited an average mechanical strength of 2645.24±232.14 N and a joint efficiency of 69.78%.

Keywords: Friction Stir Welding, Dissimilar Materials, Overlap Joints, Processing Temperature, Mechanical Strength, Central Composite Design.

Contents

List of Tables

List of Figures

Nomenclature

ϵ	Plastic Strain
ω	Rotational Speed
ρ	Density
σ_{local}	Local Stress
σ_{remote}	Remote Stress
σ_{SBM}	Secondary Bending Moment Stress
$\sigma_{tensile}$	Tensile Stress
σ_{UTS}	Ultimate Tensile Strength
E	Young's Modulus
K	Thermal Conductivity
k_b	Bending Factor
M_{SB}	Secondary Bending Moment
T_{melt}	Melting Temperature
T_{soft}	Softening Temperature
v	Welding Speed

Glossary

AA	Aluminum Alloy
ANOVA	Analysis of Variance
AS	Advancing Side
BEV	Battery-Based Electric Vehicle
BM	Base Material
CCD	Central Composite Design
CW	Clock-Wise
DoE	Design of Experiments
EDS	Energy Dispersive Spectroscopy
EU	European Union
FEM	Finite Elements Model
FFD	Full Factorial Design
FSW	Friction Stir Welding
GFR	Glass Fiber Reinforced
GHG	Greenhouse Gas
HAZ	Heat Affected Zone
HDPE	High-Density Polyethylene
hFCV	Hydrogen Fuel Cell Vehicle
HIPS	High Impact Polystyrene
ICE	Internal Combustion Engine
PC	Polycarbonate
PEEK	Polyether Ether Ketone
PMMA	Polymethyl Methacrylate
PP	Polypropylene
PPE	Polyphenylene Ether

PPS	Polyphenylene Sulfide
RS	Retreating Side
RSD	Response Surface Design
SEM	Scanning Electron Microscopy
SSW	Solid State Welding
SZ	Stir Zone
TMAZ	Thermo-Mechanically Affected Zone
UTL	Ultimate Tensile Load
UTS	Ultimate Tensile Strength

Chapter 1

Introduction

1.1 Background

Recent scientific and technological advances in material joining have revolutionized how engineers and designers combine dissimilar materials. Innovative structural concepts can now leverage the unique characteristics of various components, such as aluminum alloys and polymers/composites, instead of having to rely on a single material. This approach allows for the creation of structures with superior mechanical performance, reduced weight, and improved sustainability. Recent research work has been carried out to develop dissimilar joints, namely between metal alloys and polymers/composites through solid-state joining technologies, amongst them, Friction Stir Welding (FSW) technologies [1–10]. The FSW process is generally regarded as straightforward in concept. It relies on a non-consumable rotating tool, which generates heat through friction with the base materials, in addition to the energy released by the materials undergoing severe plastic deformation. This technology does not require filler materials or shielding gases making it a clean and environmentally friendly process [11, 12]. Applying this technology to the automotive industry, in the manufacturing processes of fuel cell system subframes, battery trays, and battery packs, has been successfully researched and proven to be of interest to the sector [13–16].

In the European Union (EU), the transport sector is responsible for almost 25% of all greenhouse gas (GHG) emissions, with road transport amounting to 70% of all GHG emissions in 2019. It is the only sector of the EU economy where emissions continue to surpass levels recorded in 1990, according to the European Environment Agency. With the EU's goal of reaching climate neutrality by 2050, set by the European Green Deal, the transportation system must become, as a whole, sustainable, and one of the many paths comes from the decarbonization of transport by finding alternatives to the current propulsion fossil fuel based systems [17, 18].

Both battery-based electric vehicles (BEVs) and hydrogen fuel cell vehicles (hFCVs) have emerged as key alternatives to internal combustion engine (ICE) vehicles, and with them came substantial research and investment in these technologies over the past few years [19–24]. In comparison with fossil fuel-based technologies, they are in the emerging phase of technological advancement and still have significant challenges to overcome for a full transition to occur.

Starting with BEVs, they still suffer from low energy density in their batteries compared to fossil fuels. This results in heavier vehicles than their ICE counterparts. This discrepancy is a factor that contributes to the diminishing of the vehicles' range and autonomy and also impacts their dynamic performance [25–27]. Another factor is the thermal management of the batteries which can negatively impact the BEVs' performance due to operating outside the optimal temperature range, jeopardizing their range and/or autonomy [28, 29]. Looking now at hFCVs, depending on the state in which the hydrogen is stored, either gas or liquid, technical challenges arise from it requiring extreme conditions like very high pressure or very low temperatures, respectively [21, 30]. Another difficulty regards the metallic reservoirs needed to store the hydrogen, which are prone to H_2 embrittlement resulting in deteriorating static and fatigue properties [31–33]. Similar to the BEVs, a significant increase in the vehicle weight is noted when accommodating the technical requirements that ensure the safety of the H_2 metallic reservoirs [34].

One way of overcoming these challenges is by developing new integral multi-purpose designs that extract the potential from dissimilar structures. When properly done, dissimilar structures offer the unique advantage of combining the qualities of each material, such as mechanical strength, and thermal or electrical insulation, all while decreasing the weight of the overall structure. However, the advantage of combining attributes is also the main difficulty for the joining processes. Divergent mechanical, thermal, and chemical properties make the traditional joining processes inherently difficult or less effective, requiring new manufacturing technologies to overcome these challenges [35], much like Friction Stir Welding.

Posing this, the scope of this thesis focused on designing the experiment and producing dissimilar aluminum-polymer FSW overlap joints and testing them, with the intent of optimizing the outcome and achieving joints with enhanced mechanical strength. This experimental work will be complemented by a thorough review of the available research on the subject to allow for a comprehensible and adjusted analysis of the results.

1.2 Objectives

With the main objective of understanding and optimizing the FSW parameters, when joining dissimilar materials, the following sub-objectives were drawn out:

- State of the art review on dissimilar joints between metals and polymers - joining technologies, mechanical strength, structural integrity, joint morphology, joint defects;
- Design of Experiment (DoE) based on the Central Composite Design methodology (CCD) to obtain the relation between the process parameters and the joint resistance;
- Production of dissimilar joints to be submitted to several tests, to characterize their structural integrity - static testing;
- Morphological and mechanical characterization of the dissimilar joints;
- Production of dissimilar joints with the found optimized parameters;

1.3 Thesis Structure

The remaining sections of this thesis are structured as described in Figure 1.1.

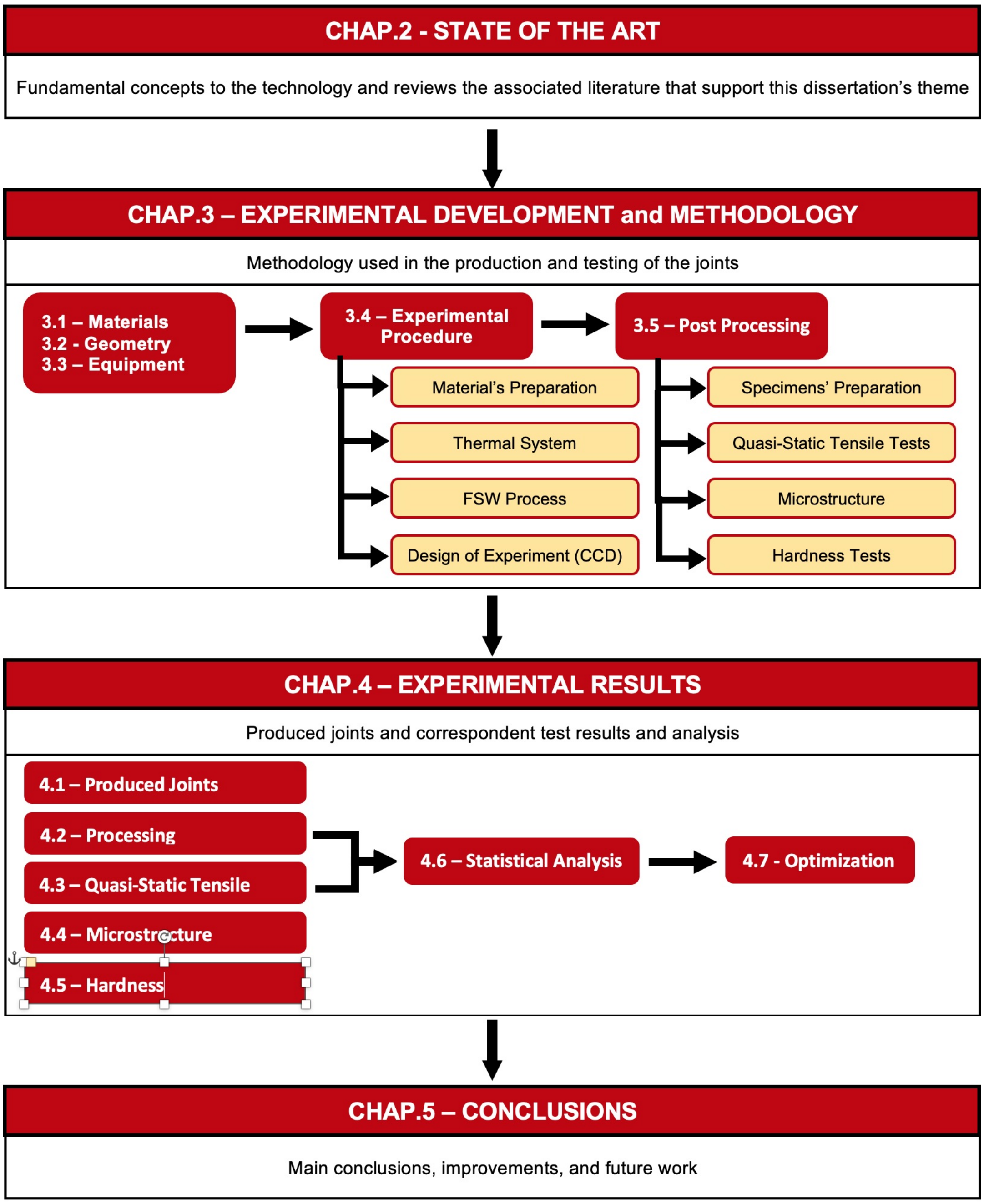

Figure 1.1: Thesis structure and organization of Chapters 2, 3, 4, and 5.

Chapter 2

State of the Art

In this chapter there will be an introduction to the main joining technologies, focusing particularly on joining dissimilar materials, followed by an in-depth presentation of the fundamental concepts and characteristics of the Friction Stir Welding (FSW) process. Prioritizing the study of dissimilar joints produced through FSW, different studies were analysed with the intent of summarizing the common and opposing views on the subject, particularly in aspects of hardness, temperature, tensile strength, joint morphology, and joint defects. Lastly, and in line with the optimization work to be done, there will be an initial explanation of design-of-experiments (DoE) followed by a more in-depth description of the chosen Central Composite Design (CCD) method.

2.1 Joining Technologies

In this section, different joining technologies will be introduced. A brief overview of adhesive bonding, mechanical fastening, and welding will be presented and a particular emphasis will be placed on the FSW process, its parameters, joint morphology, and tools. All these topics will be addressed aiming at the joining of dissimilar materials.

2.1.1 Adhesive Bonding

In 1987, A. J. Kinloch defined an adhesive to be “a material which when applied to surfaces of materials can join them together and resist separation” [36]. Similarly, in 2000, E. M. Petrie described the term adhesive as “a substance capable of holding at least two surfaces together in a strong and permanent manner” [37].

Adhesive bonding is a joining technology that can be characterized as the act of creating a bond between surfaces of similar or dissimilar materials, with the use of an adhesive agent. Said bond must be able to keep the surfaces together.

A joint bonded by adhesives is, generally, formed following three separate steps. Firstly, the adhesive is spread onto the surfaces being bonded, in order to create a good molecular contact between both adhesive and surface. Afterward, the adhesive must be hardened, a process that is dependent on the specific adhesive. Amongst others, it can harden by loss of solvent or water, cooling, chemical reaction, pressure variation, and physical absorption [38]. Lastly, in order to achieve good results in regards to the joint's durability and capability to carry loads, service conditions and joint design must be understood completely [39].

Apart from day-to-day applications, adhesive bonding, as a joining technology, is widely used in the automotive and aeronautical industries.

Some advantages of this joining technology are the ability to join dissimilar materials and or thin sheet materials, improve the stress distribution, appearance, and corrosion resistance of the joint, increase design flexibility, and reduce the weight and cost. On the other hand, some disadvantages are: the time necessary to create the joint, surfaces may require some degree of pretreatment, non-destructive test methods are scarce and a high service temperature or humidity may not be sustained [36, 39].

2.1.2 Mechanical Fastening

Mechanical joining creates an assembly through the use of either integral features of the components or the use of an external component, denominated as a fastener. This results in integral mechanical attachment or mechanical fastening, respectively [40]. Mechanical fastening is a joining technology that relies on supplemental devices to join the components in an assembly, without fusing the joint together [41, 42].

A broad way to categorize fasteners is by the existence of threads. When present they develop the needed interference forces, mainly through clamping, when absent, the same forces are developed through a pinning action [40].

Some examples of the first category are screws, nuts, bolts, and threaded studs. As for the second category: nails, pins, and rivets. Outside this classification exist other fasteners such as magnetic connection. Mechanical fastening can be applied in a variety of contexts where strength, appearance, and reusability are factors to be taken into consideration [43].

Some advantages of this joining technology are disassembly without damage, aiding in maintenance, disposal, or mobility, not changing materials' microstructure or composition, joining dissimilar materials easily and without pretreatment, and efficient joining method with a relatively low cost. In contrast, some disadvantages may be accidental disassembly, increase in weight, the concentration of stresses at joint points being more susceptible to corrosion, and being a labor-intensive technique making it time-consuming and, in some cases, difficult to automate [40, 41].

2.1.3 Welding Process

Welding can be defined as a process in which multiple parts are joined continuously by means of heat and/or pressure, with or without the addition of a filler material. Welded joints can be produced in various materials, e.g., metals and polymers, as a result of a combination of heat and/or pressure parameters [40, 44].

The continuous junction of material happens through the formation of primary and/or secondary atomic/molecular bonds, depending on the material in question, leading to an equilibrium of the attractive and repulsive interatomic/intermolecular forces. Metals are joined through metallic bonds. Thermoplastics through covalent bonds and considerable secondary bonds [40, 42].

Some advantages of this joining technology are delivering exceptional structural integrity, where some joint strength surpasses the base materials' strength, the number of processes, and the wide variety of materials that can be welded, as well as the possibility to be performed anywhere from manually to fully automatically. In opposition, some disadvantages could be the incapacity of disassembly, the increased cost for higher standard welds, the necessity for operator skill, and the possible degradation of materials' properties. [40]

Traditional welding techniques usually rely on melting the underlying material and/or the filler material, when present. Solid state welding (SSW) processes produce joints either below the melting point of the materials involved or without melting a significant part of said materials. Bonding happens through deformation and diffusion using mechanical, electrical, and/or thermal energy. This, usually, results in joints free of gas porosity, hot cracking, and nonmetallic inclusions, commonly known as solidification defects [11].

When joining dissimilar materials, SSW processes are a suitable alternative to fusion welding processes. Dissimilar materials tend to have dissimilar characteristics including, chemical composition, thermal expansion, and conductivity, these processes offer viable alternatives [11]. Since there is no significant melting of the base materials, joining mechanisms rely mostly on mechanical interlocking as well as adhesion of the base materials. SSW encases different processes, namely, Friction Stir Welding.

2.1.4 Friction Stir Welding

Friction Stir Welding (FSW), known for being a solid state welding process, was invented in 1991 by Wayne M. Thomas, at The Welding Institute in the United Kingdom [45, 46]. Its development has allowed the creation of new design concepts for joining metallic alloys and lightweight metallic materials, revolutionizing traditional methods such as mechanical fastening or fusion welding. The FSW technology has allowed for materials, which were previously considered very difficult or even impossible to join, to be welded whilst maintaining good mechanical properties [47] for example, welding aluminum from the 2XXX series [48, 49], the 7XXX series [50], steel and aluminum [51–53] or even aluminum and polymers/composites [1–10].

The quality of the welds produced through FSW is not dependent on the operator's skill. It is an autogenous process, meaning it does not require any filler material. As a result, with the advancement of the technology, FSW enables the joining of similar and dissimilar metallic alloys, dissimilar non-metals and even combinations of metallic alloys and non-metals [35].

Since FSW is a solid state welding process, issues commonly associated with re-solidification in fusion welding processes - cracking, excessive softening of the Heat Affected Zone, distortion, and/or residual stresses - can be minimized. During the FSW process, the mechanical energy, supplied by the tool, is converted into heat through friction between the surface of the tool and the base materials.

Moreover, the energy released by the materials undergoing severe plastic deformation is also converted into heat. Both actions generate the necessary heat input to achieve the desired joint. For these reasons, this joining technology is considered a clean and environmentally friendly process [11, 12].

FSW allows for the creation of joints with various geometries. The most commonly used geometries are butt and lap joints, which can be used in a wide range of applications. However, recent studies have demonstrated the feasibility of FSW in other geometries [54–56].

The process relies on a non-consumable tool with rotational movement, which is composed of a shoulder and a pin with specific geometries. The process begins with the tool being positioned. After the rotational movement starts, a vertical force is applied perpendicular to the weld plane. Once the tool penetrates the material, it follows a predetermined path along the joint. To achieve high-quality welds, it is essential to incorporate a clamping system that suits the geometry of the materials being joined, as well as the forces involved in the joining process.

The advantages of FSW processes include weight reduction and the production of welds with good mechanical properties. With the proper selection of welding parameters, these welds can match or even surpass the properties of the weakest base material [35].

Process

As schematized in Figure 2.1, the FSW process can be divided into four different phases:

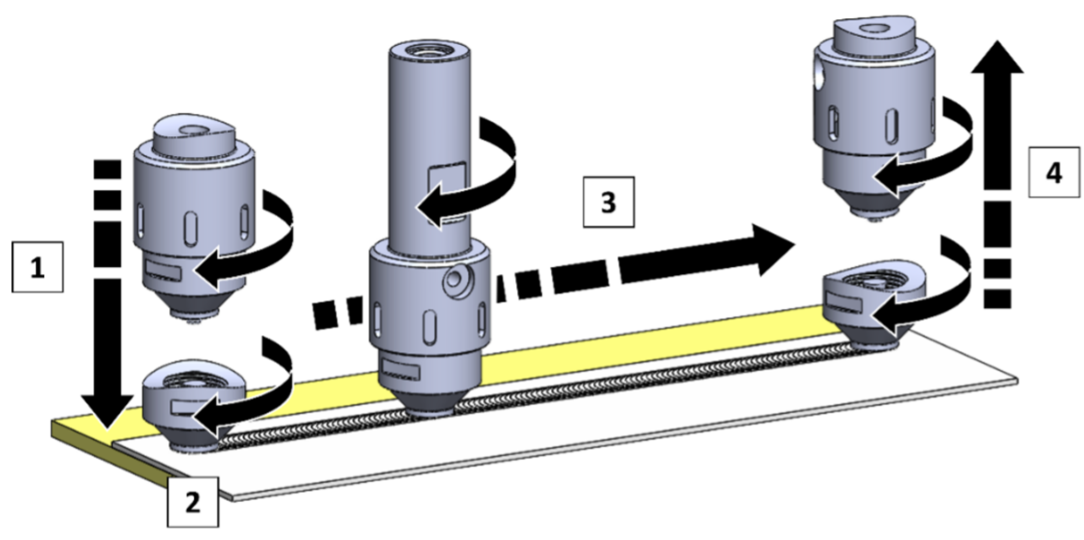

Figure 2.1: Diagram of FSW phases: 1 – Plunging; 2 – Dwelling; 3 – Welding; 4 – Retracting [10].

- **Plunging phase**: the tool is slowly lowered until the shoulder is in contact with the material. The pin penetrated the material, by action of a vertical force. Plastic deformation begins at this stage.
- **Dwelling phase**: after the predefined starting position is reached, the tool begins its rotational movement, whilst staying static in the plane. In this phase, friction generates heat which will gradually create the plastic deformation of the material. This stage's duration is defined before the process begins lasting, usually, a few seconds.
- **Welding phase**: whilst keeping its rotational speed, achieved in the previous phase, the tool is

animated by a constant translation velocity. The tool performs its trajectory, which has been previously drawn out, and will create the desired weld. The heat generated both by its movement, rotational and translation, and the vertical force applied, will promote the deformation of the plasticized material. Extrusion and cut phenomena may occur at this moment.

- **Retracting phase**: when the final location is reached, the tool is retracted. In its place remains a characteristic geometric deformation called a keyhole.

Parameters

The FSW process is characterized by many parameters which govern the resultant thermal and mechanical properties. Listed below are the main process parameters, some shown in Figure 2.2:

- **Rotational speed**, ω [rpm] - spinning velocity of the tool during the process. When increased, is associated with a higher generated friction which translates to more heat generation;
- **Welding speed**, v [cm/min] - tool traveling velocity along the weld line. Tendentiously, higher welding speeds are associated with less heat generation;
- **Plunge speed**, [mm/s] - velocity at which the tool makes contact with the materials. ;
- **Tilt angle**, [º] - degree of inclination between the shoulder surface and the materials. When correctly applied it can reduce the degree of material expelled from the weld line in the form of flash;
- **Dwell time**, [s] - time where the tool is stationary in the weld plane, with rotational speed present. Allows for the correct initial softening of the base materials;
- **Direction of rotation**, Clockwise or counterclockwise - decided upon the choice of position for the base materials and/ the type of threading in the pin;
- **Vertical force** [kN] - force produced by the FSW tool, perpendicular to the base materials. Assures uninterrupted contact during the process and, when increased, is linked to excessive softening of the base materials. Directly related to plunge depth;
- **Plunge depth**, [mm] - depth of insertion of the tool in the base material. Directly related to vertical force.

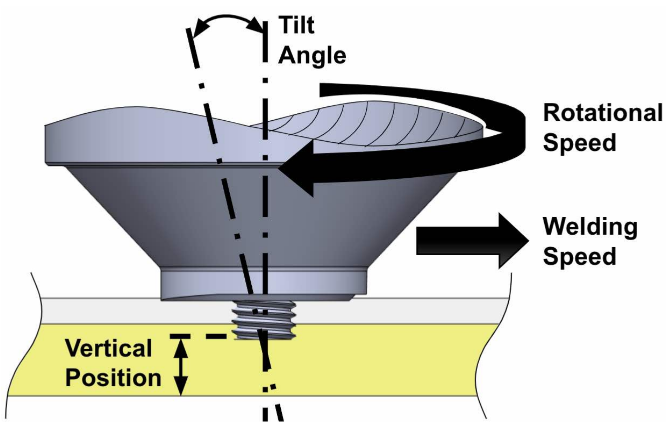

Figure 2.2: Tool's relative position to the base materials, during the process [57].

Along with the process parameters, it is essential to specify the type of control of the process - position or force. When position control is chosen, the vertical position established at the beginning of the process is to be kept, by the tool, throughout the welding process. It is the machine's job to adapt the vertical force exerted in order to keep the defined height. When the control parameter is force, it must be defined how much force the tool must bear, and, the said amount, must be kept throughout the process. Oscillations to the tool's vertical position, during the welding process, may be necessary to keep the force steady.

Joint morphology

Figure 2.3 illustrates the different zones found when a cut is made through the cross section of an FSW joint. Typically, these zones can be distinguished by the differences in microstructure and mechanical properties.

- **Base material (BM)**: Zone with no alteration in morphology, microstructure, or mechanical properties due to minimal heat input to the materials.
- **Heat affected zone (HAZ)**: Zone with no plastic deformation. Changes found in microstructure and mechanical properties are caused by an increment in heat input.
- **Thermo-mechanically affected zone (TMAZ)**: Zone with plastic deformation which, in combination with heat transfer, is sufficient to alter the material's properties. The plastic flow of the material can be identified due to grain reorientation and elongation. For aluminum alloys, this is a characteristic zone where recrystallization does not occur.
- **Stir zone (SZ)**:Zone with intense plastic deformation. The high heat input, in this zone, promotes recrystallization, resulting in a fine and equiaxial microstructure. The tool's design and movement can generate characteristic ring-shaped structures around the pin.

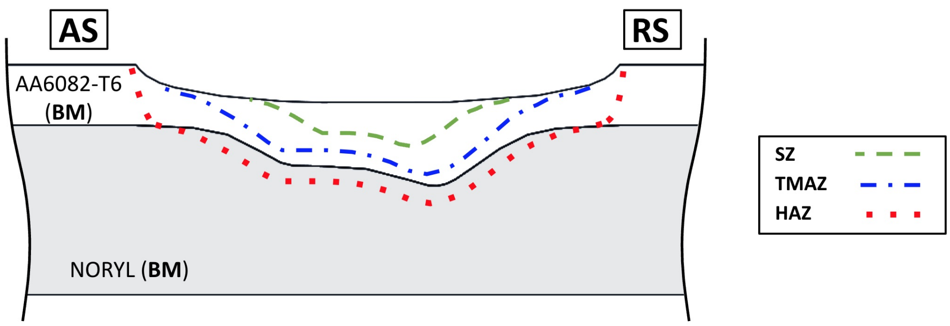

Figure 2.3: Schematic of a cross section of an overlap dissimilar FSW joint, delimitation of the different zones.

Given the coexistence of both rotation and translation movements, two sides can be identified:

- **Advancing Side (AS):** side where both welding and the tangential component of the rotational speed of the tool have the same direction.
- **Retreating Side (RS):** side where the welding and the tangential component of the rotational speed of the tool have opposite directions.

As can be observed from Figure 2.3, the cross section of a typical FSW weld is not symmetrical. During the process, the softened material is deformed by the movement of the tool, facilitated by the shoulder and pin. Due to the material's malleability, it tends to accumulate on the retreating side (RS) as a result of the opposing translation and rotational motion of the tool.

Tool

The tools used for FSW processes consist of a non-consumable rotating shoulder and pin configuration. As seen in Figure 2.4, the shoulder component, has a larger diameter and, generally, a concave and threaded surface, whilst the pin, when present, protrudes from the shoulder surface, with a smaller diameter. During the process, the shoulder has two functions: generate and maintain the heat that results from friction between the tool and the base material and, contain the flow of plastically deformed material, preventing it from flowing out of the joining region. The pin's main role is to mix the material in the weld zone which has been softened by the heat generated through the rotational and translation movement of the tool. Together, these components enable the formation of a weld between the base materials [41, 58, 59].

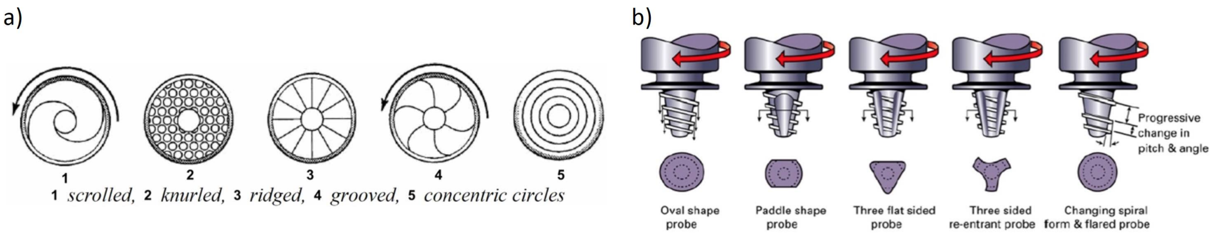

Figure 2.4: a) Shoulder surface eg. [60], b) Pin geometry eg. [58].

When designing a shoulder both the external diameter of the base and the geometry of the contact surface must be defined. The surface can either be flat, concave, or convex, with a variety of features such as rides, grooves, or concentric circles, as seen in Figure 2.4 a). As for the pin, also known as the probe, two dimensions must be defined, being the length of the pin and the diameter along the length. As for its features, the bottom of the pin can be flat or rounded, the body can be cylindrical, conical, or various other geometries and finally, the surface can be smooth or threaded in different ways [60]. Some pin examples are presented in Figure 2.4 b).

The design of the FSW tool plays a crucial role in the quality of the welds produced. The material's flow is directly influenced by the tool's parameters, including shoulder and pin diameter, pin shape, and tilt angle. Consequently, these factors have an impact on the resulting microstructure of the material [11, 59].

2.2 Friction Stir Welding of Aluminum and Polymer joints: a review

In spite of the relatively sparse research conducted in this domain, recently more authors have effectively employed FSW as the joining technology to combine aluminum alloys with thermoplastic materials. In an effort to combine the existent knowledge into specific categories namely, hardness, temperature, tensile strength, failure mechanism, and joint morphology, the following section was developed. Table 2.1 condenses the primary characteristics of the research under analysis.

Table 2.1: Primary parameters of the research under analysis.

Reference	Materials	Configuration	ω [rpm]	v [mm/min]	α [°]	Joint Eff. [%]
[1]	AA6061 PMMA	Butt joint	500, 771, 1000	31.5, 40, 50	2	$\sim$ 16%
[2]	AA6061 PC	Butt joint	500, 771, 1000, 1400	40, 63, 80	0	$\sim$ 34%
[3]	AA6111 PPS	Overlap joint	1200	10, 15, 20, 25	0	ND
[4]	AA6061 GFR nylon	Overlap joint	700, 900	15, 25	0	$\sim$ 9%
[5]	AA5058 PC	Overlap joint	960, 1200, 1600, 1940	45, 90	2	$\sim$ 69%
[6]	AA5058 PMMA	Overlap joint	600	25	0, 1, 2	$\sim$ 60%
[7]	AA5052 PP-C30S	Overlap joint	800, 900, 1000 1100, 1200	70	3	$\sim$ 20%
[8]	AA6061 PEEK	Overlap joint	900	30, 50, 70, 90	2	$\sim$ 20%
[9]	AA5059 HDPE	Butt joint	400 to 2000	30 to 200	0	$\sim$ 20%

2.2.1 Hardness

In an attempt to study the local properties of dissimilar FSW joints, indentation hardness measurement can prove to be a valuable asset. For a broader analysis of the cross section, this evaluation can be made across the different zones described in Subsection 2.1.4.

Dalwadi *et al.* [1] performed hardness testing on both materials, AA 6061 and PMMA, joined in a butt configuration. It was concluded that the aluminum's hardness reduced slightly with the reduction of rotational speed, due to the decrease in plastic deformation. Similarly, although this time in an overlap configuration, Huang *et al.* [8] determined that the hardness at the AA6061 T6 anchor had the same evolution in regards to the welding speed. This anchor is a hook-like aluminum structure that can sometimes appear in FSW joints. In regards to the relationship between rotational speed and hardness, Shahmiri *et al.* [7] recognized to have found different results. In this study, an overlap joint of an AA5052 aluminum alloy and polypropylene sheets was developed and studied. They found that increasing the rotational speed of the tool resulted in a decrease in the metal hardness in both SZ and HAZ. The justification was the increase in heat input which translated into more grain growth of the SZ and higher recovery rates of the HAZ. Derazkola *et al.* [5] found a correlation that could link the previous ones. An increase in AA5058's hardness was found to be caused by an increase in rotation speed and/or a decrease in welding speed which translates into an increase in heat input.

Patel *et al.* [2], who joined AA6061 and PC in a butt configuration, and Dalwadi *et al.* [1] found, for both metal and polymer, a decrease in hardness with an increase in distance to the center weld line. Still in regards to the aluminum, Khodabakhshi *et al.* [9] and Shahmiri *et al.* [7] detected a significant reduction in hardness in the HAZ and the TMAZ, depicted in Figure 2.5.

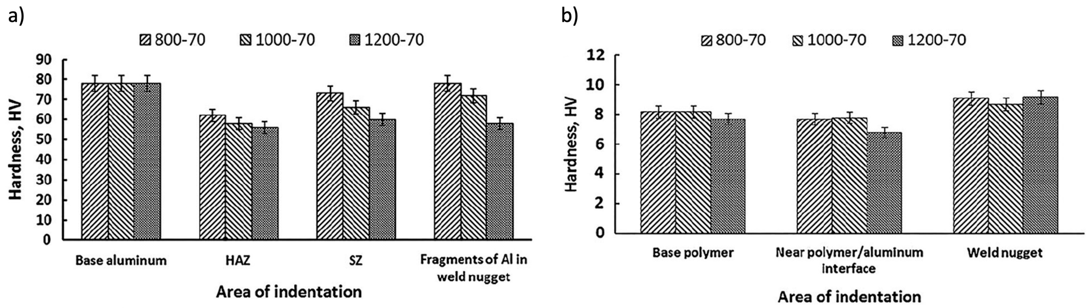

Figure 2.5: Local hardness a) AA5052, b) PP-C30S [7].

At higher deformation rates, the grain became noticeably finer, and higher hardness values were obtained. This conclusion is shared between Dalwadi, Derazkola, and Shahmiri [1, 5, 7].

Derazkola *et al.* [5] studied PC's hardness variations across a straight line in the HAZ from the AS to the RS, in the center of the weld. For the approach used, and since particles of both materials were present in the SZ, an accurate measurement couldn't be made. PC's hardness was smaller for a lower welding speed and it decreased with increasing rotation speed. Most likely, the reason for this was the reduction of molecular weight caused by the frictional heat. Patel *et al.* [2] and Shahmiri *et al.* [7] found similar results. A reduction in hardness, detected in the weld area, was caused by the frictional heat and tool stirring, which plasticized the material and caused thermal degradation. The fluctuation in its value was found to be caused by aluminum inclusions. Contrarily, Dalwadi *et al.* [1] saw that the hardness near the weld was higher than towards the parent material and that the uneven variation of PMMA's hardness could be justified by mechanical interlocking of AA6061 chips in the material and thermal degradation caused by frictional heat. Likewise, Huang, Shahmiri, and Khodabakhshi [7–9] observed that, on average, the polymer's SZ hardness was higher than the BM and detected aluminum fragments in the polymer at the SZ.

2.2.2 Processing Temperature

FSW processes rely heavily on heat generation and distribution. Not only is heat produced through friction between the tool and base material, but also through the plastic deformation which ultimately enables the joint's formation. Although sometimes forgotten, understanding the temperature field and its variations can give further insight into the process and its parameters.

Yan *et al.* [4] studied the variation of temperature in relation to the AS and RS, the rotation and welding speeds, and the plunge depth. Figure 2.6 a) depicts a small but present variation of the weld temperature with the weld side, being higher on the AS than on the RS. This is caused by a larger degree of plastic deformation produced by the higher linear velocity. Since the AA6061 sheet was placed on the AS, it promoted better heat dissipation, making this difference relatively small. During this study, different combinations of rotation speed, welding speed, and plunge depth were made and their temperatures were recorded in Figure 2.6 b). For a lower rotation and welding speed, the maximum temperature reached the melting temperature of the polymer. An increase in the welding speed caused a decrease in the unit frictional heat input which reduced the peak temperature. As expected, when the rotation speed was increased, and by means of an increase in friction, the temperature rose significantly. The same result was achieved when the plunge depth was higher, increasing the shoulder pressure.

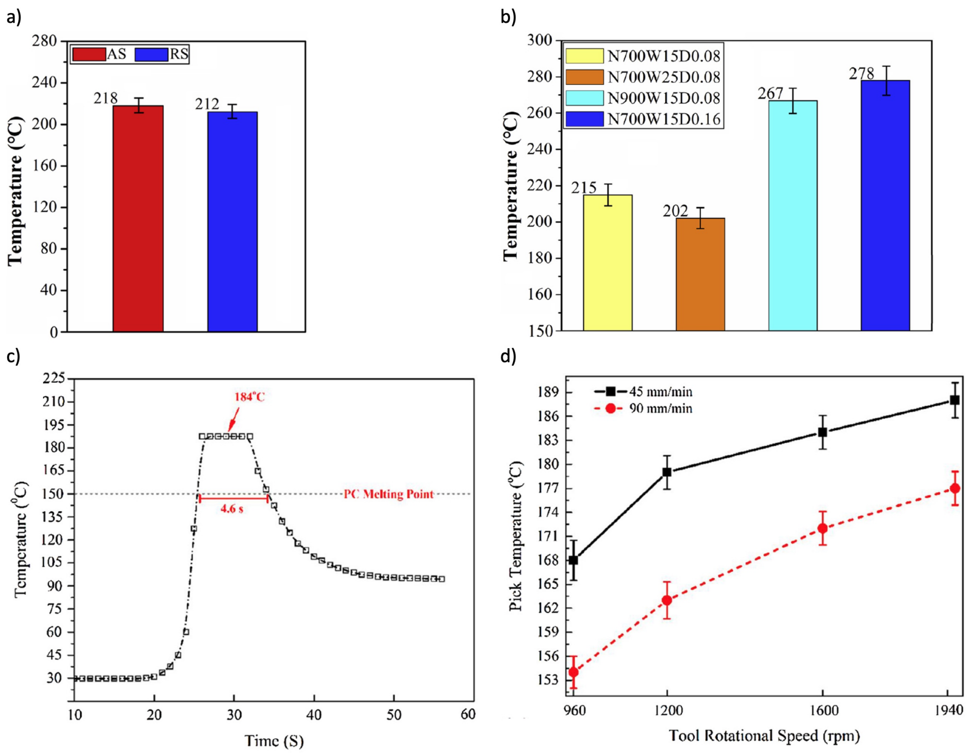

Figure 2.6: Processing temperature a) AS vs RS [4], b) for various welding and rotational speeds and plunge depths [4], c) during the FSW procedure [5], d) at different welding and rotational speeds [5].

Contrarily to Yan *et al.* [4], Derazkola *et al.* [5] created an overlap joint by placing the polycarbonate sheet on top of the AA5058. As it can be seen in Figure 2.6 c), the temperature's behavior started by rising abruptly until peak temperature was reached. This temperature stayed unchanged for a short period of time before cooling began. The location of the PC sheet on top of the aluminum and the low thermal properties of the polymer caused the temperature at the weld line, to remain high, even after the tool had passed. Figure 2.6 d) shows that regardless of the rotation or welding speeds chosen, the peak temperature always exceeded the PC's melting temperature of 147ºC.

2.2.3 Tensile strength/joint efficiency

To critically analyze and compare the tensile strength results from joints composed of different material combinations it is imperative to find a comparable unit. In this case, the term used is the joint's efficiency which can be described as the ratio between the joint's tensile strength and base polymer's ultimate tensile strength.

Throughout different studies, different parameters were found to have a beneficial impact on the tensile strength. Ratanathavorn *et al.* [3] found that strength increased at higher welding speeds since the pore-filled regions around the chips were smaller. This might be justified by a temperature decrease with a welding speed increase, causing a decrease in the flow of molten PPS. They also concluded that the main factor in improving tensile strength was the mechanical interlocking of the SZ.

Dalwadi *et al.* [1] observed that the tensile strength was higher for the intermediate welding speed, under study, results shown in Figure 2.7. This meant that it was identified as an initial increase of tensile strength, with a later decrease. For 1000rpm, an increase was observed until the welding speed of 40 mm/min, achieving a maximum joint efficiency of 15.7% and, after that, a significant decrease. However, for a lower rotation speed, a gradual increase in tensile strength was observed with the increase in welding speed. Huang *et al.* [8] observed a similar trend of initial increase with gradual decrease with welding speed, having achieved a maximum joint efficiency of 20.6% at a welding speed of 50 mm/min.

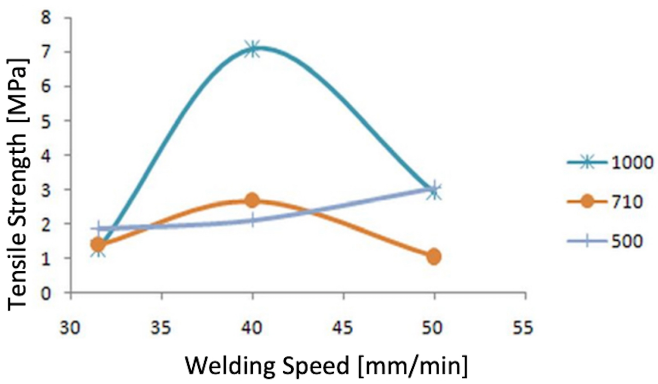

Figure 2.7: Tensile strength variation with rotational speed and welding speed [1].

Regarding the variation with rotation speed, Dalwadi *et al.* [1] observed that the tensile strength tended to increase with higher rotation speed, shown in Figure 2.7, which they attributed to an increase in frictional heating and mechanical stirring. Maximum tensile strength was obtained at 1000 rpm and 40 mm/min. Although the sample is relatively small, it can be deduced that rotation speed and advancing velocity had a significant impact on tensile strength, with the first being more prominent. This may be justified by the existence of sufficient mechanical interlocking and a balance in heat generation. Lower tensile strength appeared to be caused by an inferior heat concentration at the weld, causing poor mechanical interlocking. Derazkola *et al.* [5] achieved similar results, with the tensile strength increasing with the tool rotation speed until it reached 1600rpm and then reduced. For both welding speeds, 45 and 90 mm/min, this behavior was observed, although a higher tensile strength was recorded for a lower speed. The maximum joint efficiency achieved was 69.4%, at 1600 rpm and 45 mm/min.

Patel *et al.* [2] analysed this topic from a different perspective. Instead of looking at rotation speed and welding speed independently, this study focused on the velocity ratio [rev/mm]. They claim the ratio between the rotational and welding speed illustrates the heat generated at the tool interface, more specifically, either a very low or very high ratio decrease significantly the joint strength, as low as 5 MPa. A low-velocity ratio translates to insufficient heat generation and a poor stirring of the material, whereas a high ratio results in a large heat concentration that can cause melting and exit of the material from the weld zone. An optimal range between 10 and 20 rev/mm was concluded to attain the higher tensile strength, achieving results as high as 33.9% in terms of joint efficiency for 500 rpm, 40 mm/min, and 12.5 rev/mm.

Derazkola *et al.* [5] studied the bending strength and found that it increased with tool rotation speed until it reached 1600 rpm and then drastically reduced. For both welding speeds, 45 and 90 mm/min, this behavior was observed, although a higher bending strength was recorded for a lower speed. The maximum relative tensile strength achieved was 68.2% of PC's, at 1600 rpm and 45 mm/min. In a different study [6], depicted in Figure 2.8, Derazkola studied the impact that the tool tilt angle and plunge

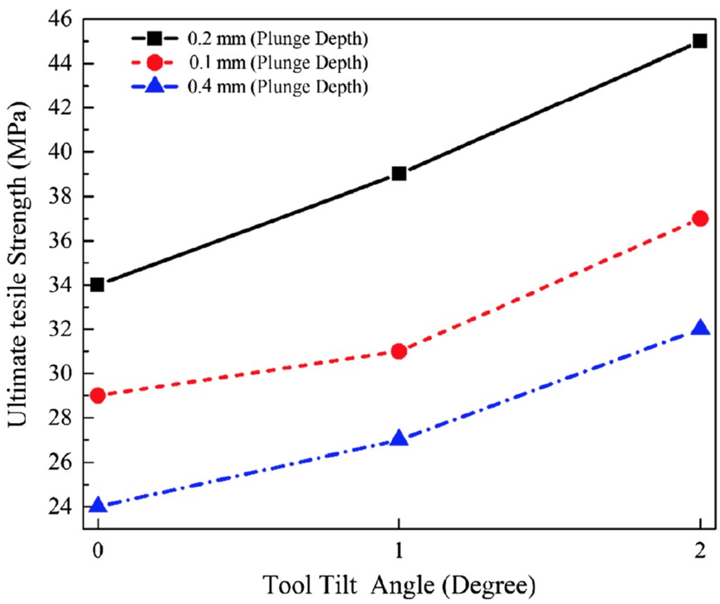

Figure 2.8: Effect of tool tilt and plunge depth in the ultimate tensile strength [6].

depth had on the tensile strength. Overall, it was found that the increase of both parameters, separately, led to an increase of the ultimate tensile stress although, in regards to the plunge depth, the increase was only registered until 0.2 mm, afterward, and until 0.4 mm, a decrease was observed. A maximum value for the joint's efficiency of 58.4% was attained at 2º tilt angle and 0.2 mm plunge depth. As a posterior conclusion, too high of a plunge depth generated too much heat which ended up causing defects and inappropriate micro and macro interlocking. Shahmiri *et al.* [7] study found supporting evidence for the impact of the plunge depth on tensile strength. In this case, it was observed that a shorter pin would lead to improperly joined materials which couldn't remain intact under hand force.

Shahmiri and Huang [7, 8] noted contradictory conclusions regarding the effect of heat input. In the first, [7], increasing the heat input resulted in a decrease in the joint's shear strength mainly caused by a thickening of the interaction layer and the gap between both materials. For the joint performed at 800 rpm and 700 mm/min, the joint with the lowest heat input, a maximum joint efficiency of 18.9% was recorded. As for the second, [8], a reduction of the aluminum anchor was observed with the decrease of heat input and was found to impair the amount of load the joint was able to bear.

2.2.4 Failure Mechanism

Examining the failure mechanism after tensile tests, both type and location can give an insight into the quality of the joint produced. Generally, failure will begin and propagate through the weakest parts of the joint, and a fracture predominantly outside the joint area and mostly on the polymer base material can indicate a well-welded joint.

Through testing, Ratanathavorn *et al.* [3] observed the first crack appearing between the SZ and the aluminum. The propagation of the crack, upward in the aluminum sheet, caused a reduction in load. This caused a rotation in the stir zone which, in itself, caused a secondary crack to form between the stir zone and the thermoplastic, resulting in a second load drop. The final fracture occurred when the first fracture fully separated the AA6111 and PPS sheets. The cross section's image can be seen in Figure 2.9 a).

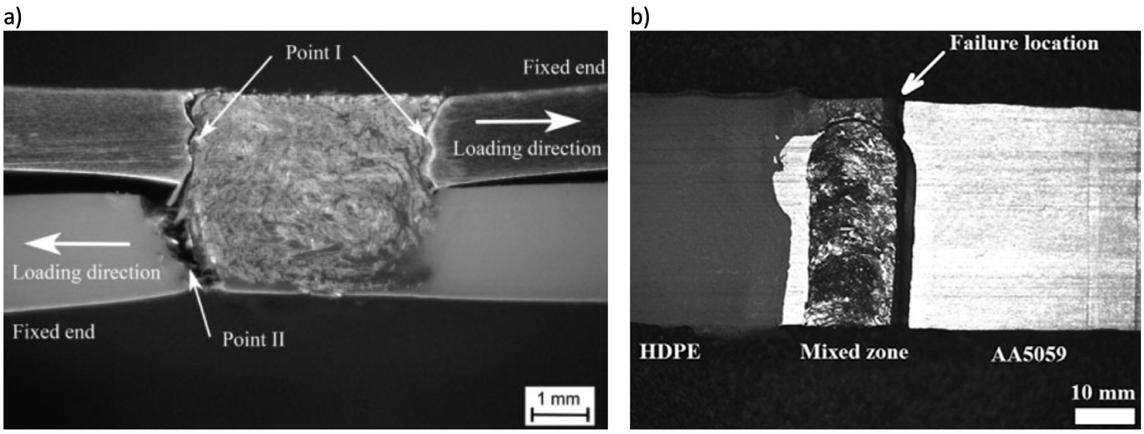

Figure 2.9: a) Cross section of a fractured specimen [3], b) Surface image of the fracture location [9].

Conversely to other authors, Derazkola *et al.* [5] did tensile as well as bending tests. Bending behavior showed that the fracture, on all specimens, was located in the SZ. Through SEM imaging, a smooth fracture path could be seen, in the upper area, followed by a disordered crack propagation which grew until the final fracture. Shrinkage bubbles changed the crack growth mode. In addition, aluminum particles played no effective role in the crack growth rate, during the bending test. Tensile behaviour showed that a crack first appeared between the interface of SZ and AA5058's TMAZ and the final fracture occurred when the central crack fully separated the AA5058 and PC sheets, indicating the location of the weakest part of the joint. SEM imaging, from the fracture surface of the PC sheet, showed fine particles of AA5058 alloy stacked on a polymer surface, which separated from the aluminum's TMAZ, during testing. Khodabakhshi *et al.* [9] found similar results to Derazkola, failure happening at the interface of the SZ and HAZ on the aluminum side, but this time in a butt joint configuration, depicted in Figure 2.9 b).

In a different study [6], Derazkola found that the location of failure varied with the process parameters. At higher heat inputs, caused by increasing tilt angle and plunge depth, tensile-shear fracture was found to be the fracture mode. Failure began at the lower part of the RS between the SZ and the metal hook and propagated until it was separated from the polymer. An increment of the plunge depth up to 0.4mm was studied. With this increase, detachment of the polymer at the interface of the TMAZ controlled the fracture behaviour. Increasing both the plunge depth and/or the tilt angle was found to affect the fracture location, pushing it toward the polymer BM. They determined that the best processing parameters, which achieved the best mechanical interlocks, were a tilt angle of 2º and a plunge depth of 0.2 mm.

Shahmiri *et al.* [7], shown in Figure 2.10, detected that failure always occurred at the polymer/aluminum interface, between the polymer and the weld nugget. Similarly, Huang *et al.* [8] found fractures to appear in the interface of the materials at the AS, caused by gaps that emerge in this location. After the initial crack, it rapidly propagated due to an increase in tensile force, breaking the adhesive-bonded area. Analogous to [6], failure took place when the aluminum anchor separated from the SZ.

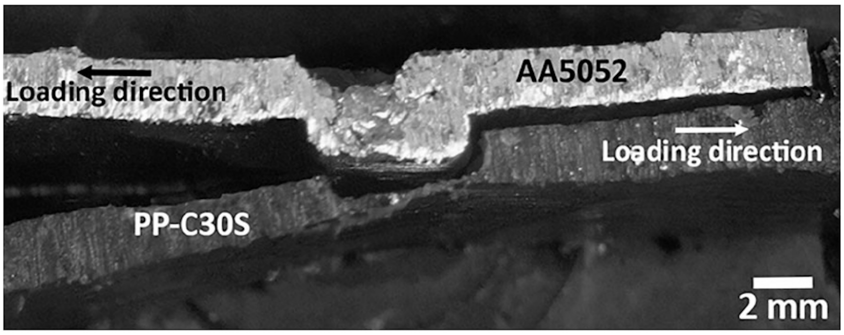

Figure 2.10: Fracture path in cross section view [7].

Changes in the speed parameters also impacted the fracture behaviour. Yan *et al.* [4] observed pure shear fracture, at a lower rotation speed and higher welding speed. Through SEM magnification, surface peeling was detected, depicting a weaker bond. When the welding speed decreased, a shear fracture came along with partial filler pulling out. This time, the SEM micrograph suggested an effective bonding. At higher rotation speeds and plunger depths, failure occurred with tearing of the middle layer and surface peeling, as well as degradation of the polymer matrix. Smooth cavity walls suggest that the joint fractured along the porous solidification. When welding speed increased, the maximum fracture load decreased, significantly. The main culprits of the reduction in joint performance were incomplete bonding between the filler and the GFR nylon sheet and the gap defect along the lap interface.

2.2.5 Joint Morphology

The morphology of an FSW joint can be divided into two categories, the surface appearance and the cross section. The surface appearance encapsulates all that can be seen with no further processing of the produced joint, this could be, a general appearance, a mixture of materials that extends to the surface of the joint, and the presence or absence of defects such as flash, tunneling or an exit hole. Such defects are explained in further detail in the next Subsection 2.2.6. The cross section morphology, which can only be analysed after cutting the joint, reveals what happened inside the joint, if the base materials retained continuity or if they mixed together, different regions (SZ, TMAZ, HAZ, nugget), the presence of defects like pores, hook structures or voids, and even what happens at the interface of the materials. The surface appearance is mostly analysed by its macrostructure, while the cross section could be evaluated by its macro, micro, or even nanostructure. Studying the joint's morphology can first and foremost give an immediate insight into how successful the joint could be, and when in conjunction with other data, it can show hidden patterns which help in the characterization of the joints.

Dalwadi *et al.* [1] joined AA6061 with PMMA in a butt joint configuration. Through microstructure analysis it is visible that there are aluminum fragments mixed with PMMA. The size of the aluminum fragments is the smallest for the highest strength performing joint, which had the larger rotational speed and an intermediate welding speed. Larger aluminum chips, seen in Figure 2.11 a), make for poor mechanical interlocking which caused a decrease in the tensile strength. No information was provided that allowed for a characterization of the surface quality of the weld.

Patel *et al.* [2] produced butt joints between AA6061 and PC. Figure 2.11 c) shows the overall appearance of the joint. The top surface was rough and irregular, with mixed material extrusion at the center of the weld line. The bottom surface was deteriorated with no resemblance to the original flat surface of the base material sheets. The cross section analysis shows a mixture of aluminum fragments in the resolidified polymer matrix. A similar relation as Dalwadi [1] was found, where finer aluminum chip size resulted in higher tensile strength of the joint. Furthermore, specimens recording a lower velocity ratio (relation between the rotation and welding velocities) had a lack of heat input and deficient mechanical deformation, which resulted in poor joint formation.

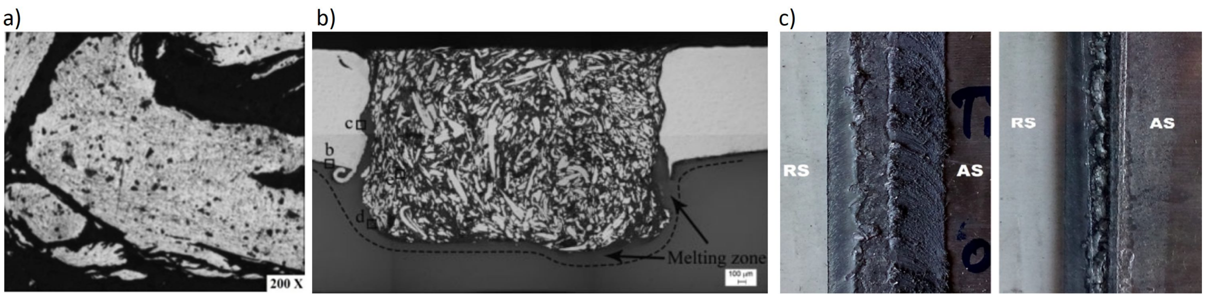

Figure 2.11: a) Aluminum fragment [1], b) Cross section view [3], c) Top and bottom surface of the joint [2].

Ratanathavorn *et al.* [3] joined AA6111 and PPS in an overlap configuration. Observing the surface of the joint, a channel of resolidified polymer mixed with aluminum chips exists where the tool penetrates the material. Other than this, the quality of the weld line is fairly good, with no flash present. The underneath surface of the joint, on the polymer sheet, presented discoloration of the polymeric material. Even though Ratanathavorn produced overlap joints, the morphology of the cross section, seen in Figure 2.11 b), was similar to the previous authors, with aluminum chips dispersed in a polymer matrix and no clear continuation of the base materials. In line with Patel [2], Ratanathavorn found that the size of the metallic chips was prominently related to the welding speed, with a higher speed generating larger fragments. Considering that the average temperature during FSW of dissimilar materials is closer to the melting temperature of the polymer rather than the aluminum, the AA6111 chips were formed by a cutting action of the pin threads, during translation. In the interface zone, between the stir zone and the PPS, some porosity can be observed.

Yan *et al.* [4] also performed studies on AA6061, joining it in an overlap configuration to GFR nylon. At lower welding speeds, softened GFR nylon was surrounded by unsoftened material leading to little to no material extrusion. On the other hand, when said velocity increased an increase in material accumulation was observed along the edge of the lapped region. A "squeezing out" action was promoted on the melted polymer, underneath the aluminum sheet, caused by the shoulder pressure. A similar, but more severe, phenomenon was observed with an increase in the plunge depth. Analysing the cross section microstructure, no mixing of aluminum and polymer was detected, as well as no aluminum fragments detached from the base material into the polymer. A fairly smooth interface was observed, with small irregularities that produce micro locks that aid in bonding both materials. As depicted in Figure 2.12, further away from the weld line, a microscopic gap can be seen at the interface. Increasing the welding speed resulted in incomplete bonding due to a reduction in heat input. An increase in rotation speed can result in material degradation due to an increase in frictional heat. This phenomenon is more apparent near the weld line center and gradually reduces as the distance increases, given the decrease in heat input. Overall, more heat input created a tighter bond thanks to a decrease in GFR nylon's viscosity.

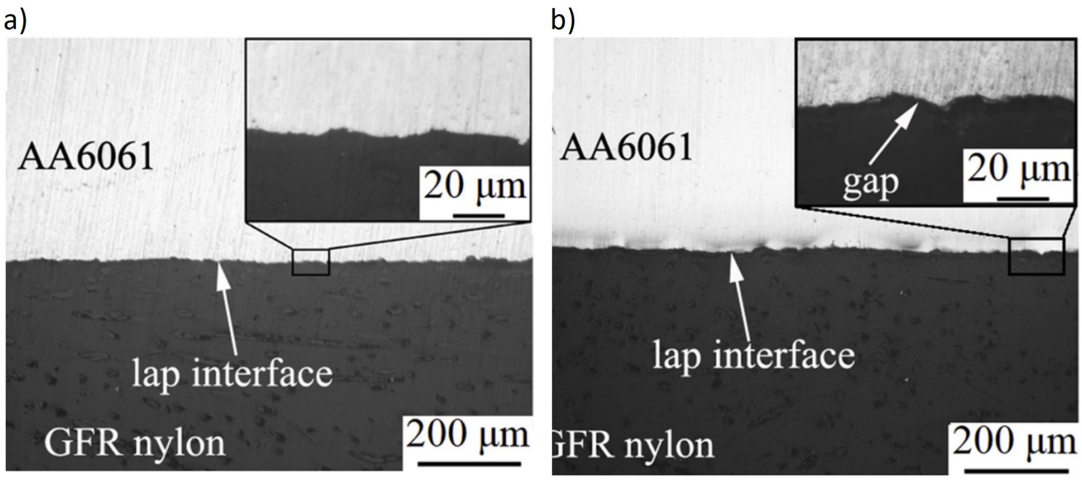

Figure 2.12: Microstructure of the interface a) closer to the weld line b) further away from the weld line, [4].

Derazkola *et al.* [5] joined AA5058 with polycarbonate in an overlap configuration. Differently from other studies, the joint produced had the polymer sheet on top of the aluminum and the tool made contact directly with the PC material. This geometric decision resulted in a poor surface appearance as the polymer got discolored by the frictional heat and the mixture of metal fragments. A decrease in joint area was found when the rotation speed was decreased whilst the welding speed was increased. This observation is similar to Patel's and Yan's [2, 4], where this specific variation in parameters leads to a lack of heat input and ultimately results in a diminished bonded area. As seen in Figure 2.13 b), when analysing the cross section morphology, it was found that the HAZ was larger in the AS when compared to the RS, and it increased with heat input. A TMAZ was also observed in the aluminum. Given the joint's geometry, during processing, the metal flowed upwards into the polymer creating a U-shape macro lock and other small indentations which increased the contact area and aided in the bonding of both materials, depicted in Figure 2.13 a). Similarly to the previous studies, aluminum particles were found embedded in the polymer. The amount of particles increased with higher rotational speed and lower welding speed, connecting this observation with an increase in heat input.

In a second study, Derazkola *et al.* [6] joined AA5058 with PMMA in an overlap configuration, and like the last, the PMMA sheet was positioned on top of the aluminum and in direct contact with the tool. As shown in Figure 2.13 c), the general surface quality of the weld denoted a rough and discolored weld line with material accumulation on the AS and a slightly smoother surface on the RS. Whilst studying the influence of the main processing parameters they found that, for the tilt angle, a value closer to 2° bettered the intermixing of the base materials. In regards to the plunge depth, an intermediate size of 0.2 mm was found to optimize the relation between what they considered to be a proper mixing of the base materials, whilst reducing the appearance of a tunnel-like defect. This study found identical observations as the previous one [4] in terms of cross section. A larger HAZ and TMAZ in the AS increased with heat input. A larger amount of aluminum fragments in the polymer matrix. And a U-shape aluminum formation which increased the contact area. Finally, an EDS chemical analysis was performed. At the interface of the materials, along with carbon, aluminum, and magnesium, they were reported to detect significant amounts of oxygen. This indicates the presence of an alumina oxide layer which aids in a secondary chemical bonding between materials.

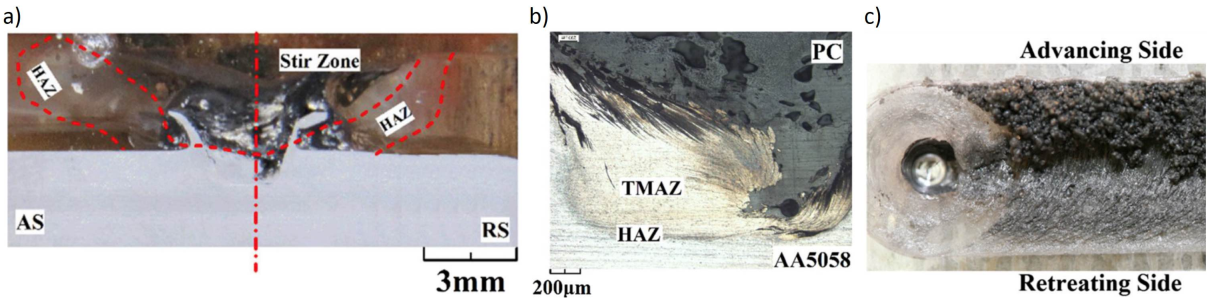

Figure 2.13: a) Cross section view with U-shape macro lock [5], b) Cross section morphology [5], c) Surface view of the weld line [6].

Shahmiri *et al.* [7] created a joint between AA5052 and polypropylene with an overlap of 25 mm. Like most studies, the overlap was done with the aluminum sheet on top and in contact with the tool. The overall appearance of the joint is depicted in Figure 2.14 a) and b), with a rough surface caused by the permeation of polymer through the aluminum sheet and an irregular bottom surface where the aluminum protrudes through the polymer sheet. A cross section observation found that the nugget size and the number of aluminum fragments were larger with a lower rotational speed, at constant welding speed. Microstructure studies were performed on the joint with the least rotational speed. In the aluminum three distinct regions were found, the HAZ, TMAZ, and SZ. In the HAZ the grain structure still resembles the cold-rolled grains of the base material. In the transition region, TMAZ, deformation of the grains is visible with elongation towards the rotation direction. Lastly, in the SZ and due to higher temperatures, there was a transformation from elongated to equated grains. Similarly to Derazkola [6], an EDS analysis was performed on the interaction layer found at the interface of the materials. This layer was mostly composed of carbon, aluminum, and oxygen atoms. Unlike the previous study, they found that this layer hindered the bonding between materials due to gaps found between the polymer and the interaction layer, and this layer and the aluminum, as depicted in Figure 2.14.

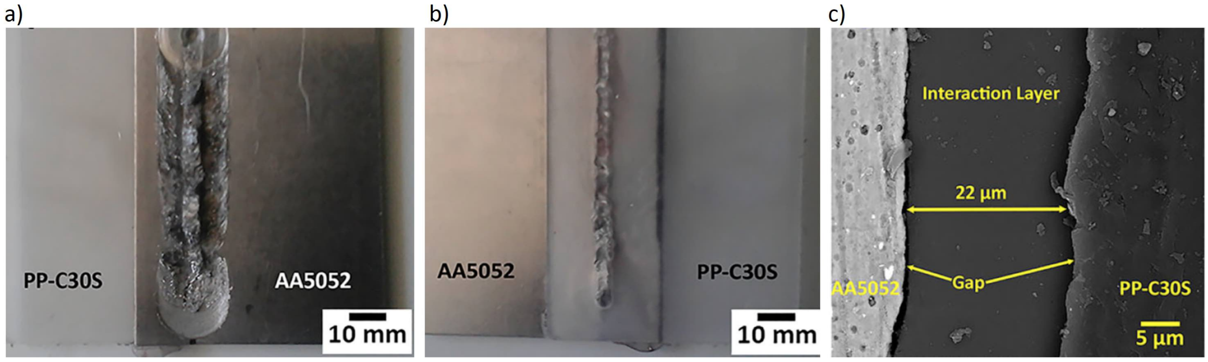

Figure 2.14: Weld line view from a) the top b) the bottom c) interaction layer at the interface of both materials [7].

Huang *et al.* [8] produced overlap joints with AA6061-T6 on top of PEEK. The global appearance of the joint reports an overflow of polymer through the aluminum at the weld line which was more prominent when the welding speed was lower, due to an increase of heat input. At the cross section, it can be seen an aluminum anchor formation which penetrates the polymer. The size of this structure is larger at the AS due to higher peak temperatures, and its overall size tends to increase with the decrease of welding speed as the heat input increases, as seen in Figure 2.15 a) and b). In the same line of thought as Derazkola's first study [5], this formation is considered beneficial to mechanical interlocking as it increases the contact area between materials. At the SZ a mixture of aluminum chips and resolidified polymer can be found.

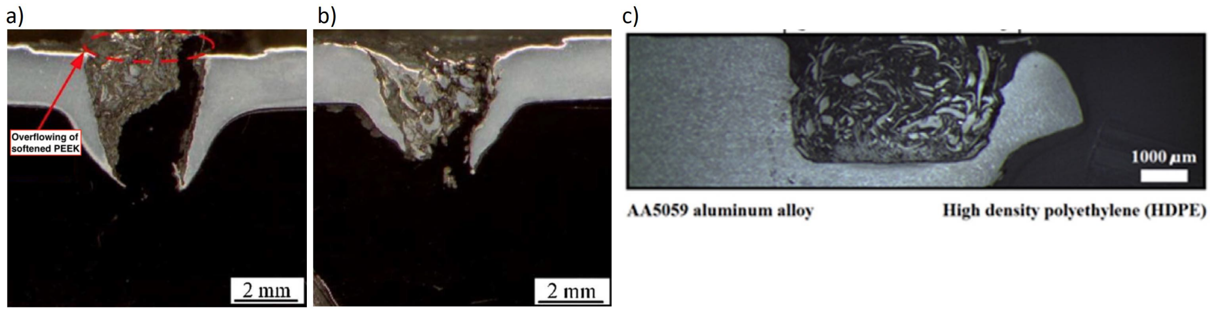

Figure 2.15: Aluminum anchor for a) 30mm/min b) 70mm/min, [8] c) Cross section view, [9].

Khodabakhshi *et al.* [9] joined AA5059 and high-density polyphenylene in a butt joint configuration. Differently from previous butt joints, the pin was shifted so that its position was mostly on top of the aluminum. The general surface appearance is represented by a rough weld line where there is a mixing of polymer and aluminum, as well as flash defects. The cross section, seen in Figure 2.15 c), shows that, a SZ formed by aluminum fragments dispersed on the resolidified polymer matrix. Larger aluminum fragments can be observed on the RS due to lower temperatures, in comparison to the AS. Different from previous studies, and due to the shifted position of the tool onto the aluminum, there is continuity of the aluminum sheet even though mixing of both materials is detected. Although EDS analysis was performed, no evidence of significant amounts of oxygen was found to support previous studies' conclusions about molecular bonding through an oxide interaction layer.

2.2.6 Joint Defects

FSW is known for producing high-quality joints, especially when the process is optimized. However, and as with any other process, it is not always possible to mitigate the factors associated with the appearance of defects, and, as so, it is important to highlight some of the main defects that are characteristic of this type of welding process.

Flash defect, shown in Figure 2.16 a), is described as an accumulation of softened on the outside edges of the weld line, in both the AS and/or RS. Common causes can be increased plunge depth and/or high heat input. High heat input is associated with a larger degree of material softening and plastic deformation which when extruded from the weld line results in flash. In the same manner, larger plunge depths create more force on the surface material aiding in material overflowing from its original location [61, 62].

When the FSW tool has a protruding pin, a **keyhole or exit-hole defect** appears where the tool last made contact with the material surface, as can be seen in Figure 2.16 a). This defect worsens with increasing pin length and can lead to a weaker joint due to the concentration of stress in that location [62].

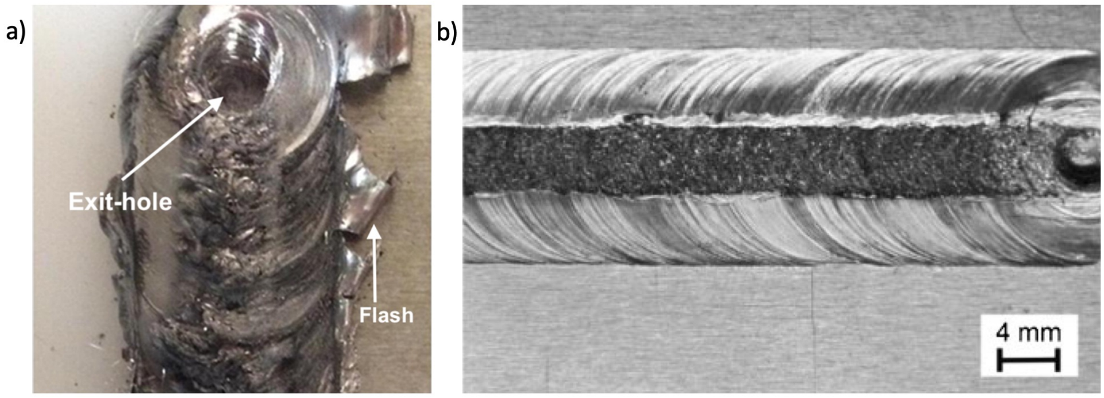

Figure 2.16: a) Flash and exit-hole defect [9], b) Surface defects [3].

Other **surface defects** can be found to disrupt the surface of the joint. These can be in the form of surface grooves caused by the passing of the shoulder giving the weld line a rough texture prone to stress concentration. In dissimilar joints, when the process settings are not adequate, an overflow of softened polymer, both through the center of the weld line as well as the interface of the materials, can occur, leading to a significant weakening of the joint. When looking at metal-polymer joints, polymer overflow through the weld line is associated with the discontinuity of the metallic sheet, seriously compromising the joint's mechanical properties [61, 62]. Both, shoulder grooves and polymer overflowing from the center of the weld line are depicted in Figure 2.16 b).

The most common ones are **voids**, which are typically found at the periphery of the HAZ [63]. In polymer joints, voids tend to appear in the RS given that the temperature in the AS, in comparison to the RS, tends to be higher due to a larger degree of plastic deformation. Polymers' low thermal conductivity copulated with insufficient heat in the RS, results in improper stirring in the SZ allowing voids to occur [61]. Typical appearance represented in Figure 2.17 a).

Pores can have various origins, amongst them, air entrapment, release of structural water, thermal degradation, or variations in thermal expansion of the materials. Their presence reduces the load-bearing area consequently decreasing the tensile strength of the joint [61]. Pores originating from air entrapment can be seen in Figure 2.17 b).

Tunnel defect, shown in Figure 2.17 c), is a cavity inside the weld line along its direction. Due to the insufficient material flow, caused by by low frictional heat, and lack of mixing, this defect usually appears in the AS. Proper plunge depth and speed parameters can minimize the appearance of this defect. Extreme cases of tunneling present a lack of filling in the surface which can also develop due to an extreme overflow of material through the interface or due to a lack of material flow or improper backing support.

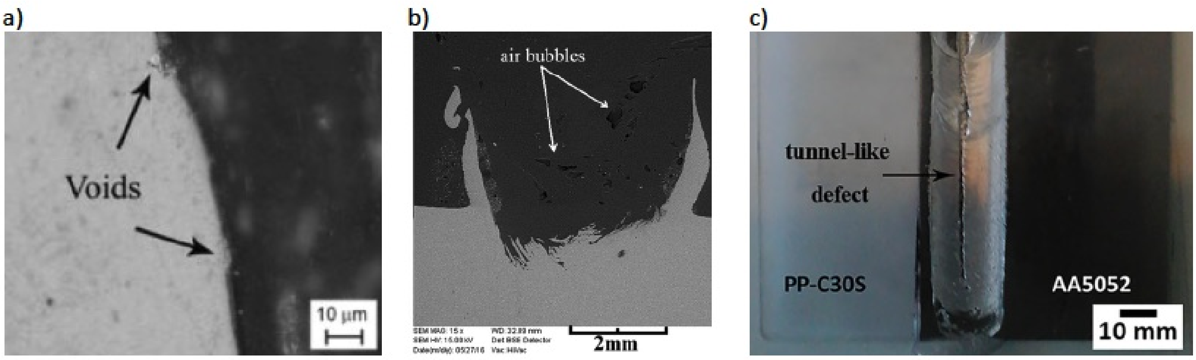

Figure 2.17: a) Voids [3], b) Pores [6], c) Tunnel defect [7].

Lack of penetration is a defect that can be directly correlated with shorter pin length and/or smaller plunge depth. When processing materials with low thermal conductivity, such as polymers, this can be exacerbated due to difficulty in softening the material that does not come in contact with the tool. Improper stirring results in a lack of root penetration which affects the load-bearing area, reducing it, and consequently, reducing tensile strength [61].

A common defect observed in joints with an overlap configuration is the formation of **hook-shaped**

structures. Hooking, depicted in Figure 2.17 b), can be caused by improper tool design and choice of parameters as well as the penetration force of the tool on the bottom sheet resulting in bending of the interface. Mitigating these defects involves optimizing welding parameters [64, 65].

2.3 Design of Experiments

Design of Experiments (DoE) is an important tool to systematically create and plan an approach, that when utilized in conjunction with statistical tools, provides an understanding of the correlations between different input parameters and output properties. It is widely used when developing and optimizing processes in scientific or industrial settings and, more recently, in optimizing welding and joining processes [66]. Generically, it requires the planning and execution of a series of experiments, according to a chosen model, to later analyze a series of results combinations, depending on the variables identified. A simple visual representation of this process is shown in Figure 2.18.

Various methods can be used to perform a DoE, each with its advantages and limitations. The Taguchi method is one of the most popular methods in optimizing processes by considering only orthogonal experimental combinations, which makes it effective by reducing the number of experiments needed [67]. However, this same strength is also a weakness of this method as orthogonal arrays permit mostly main effect analysis, making this method less effective when trying to identify more complex interactions, in comparison to other methods. One of which is the Full Factorial Design method (FFD). FFD method systematically analyzes the effects of multiple factors and their interactions on response variables, allowing for an analysis of the possible combinations of factor levels within the region under investigation [68]. However, it achieves this accurate and reliable analysis by combining factors and their levels, which by default increases the number of experiments exponentially. For larger studies, this can be a serious impediment. Another method, and the one chosen for this study, is the Central Composite Design (CCD). This method explained in further detail in the next Subsection, requires fewer experiments than the FFD, for the same amount of parameters, and is also able to model the curvature of the response surface, which becomes useful for optimization processes. In comparison, the Taguchi method was primarily designed to evaluate linear interaction, whilst the FFD can only provide such information for level 3 and above, which becomes too resource-intensive.

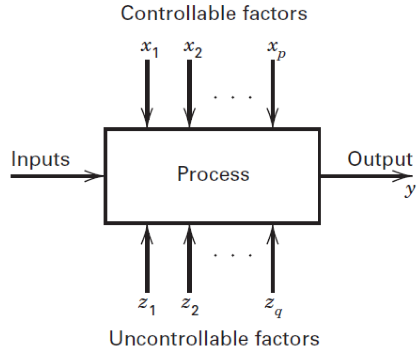

Figure 2.18: Generic representation of a DoE process, adapted from [68].

2.3.1 Central Composite Design

CCD was introduced in 1951 by Box and Wilson in the Journal of the Royal Statistical Society [69] and is a type of response surface design (RSD). RSDs are considered to be advanced DOE techniques [70]. Its second-order nature allows us to both assess linear and quadratic effects on the response variable. To achieve this, CCD comprises fractional portions, center, and axial points [66, 71], which can be interpreted, graphically, in Figure 2.19:

- Factorial Points: combination of factors at their low and high value, to generate the linear correlations between factors and responses. Usually two-level full (2^k) with code factors' levels -1 and +1.
- Center Points: assessment at the center value of all factors to determine the presence of curvature of the response surface. A n_c number of receptions can be performed at this center point. The coded levels are determined by:

$$\text{coded level} = \frac{\text{real value} - \text{mean value}}{\text{half of factors' range}} \tag{2.1}$$

- Axial Points: also known as star points, study extreme factor values that fall outside the high and low values stipulated for the experiment, allowing to assess the response surface curvature beyond the center points. An axial arrangement of 2k points where only one factor has a code value, α, different from the mid-level (0)

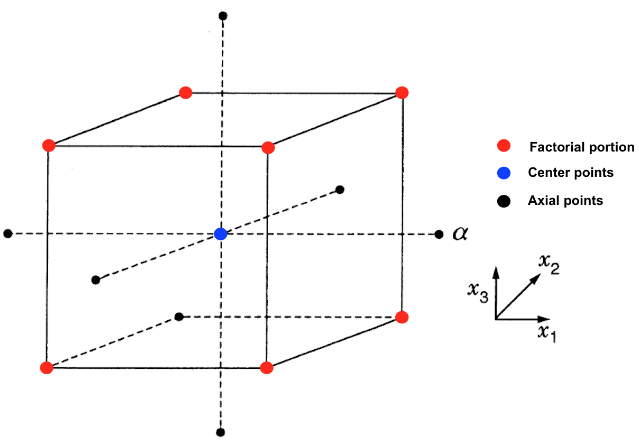

Figure 2.19: Central Composite Design for $k = 3$ and $\alpha = \sqrt[4]{2^k}$.

The α and n_c values must be defined to fit the specific experiment. The α value can vary from 1 to $\sqrt{k}$. In order to achieve rotatability, ensuring that the design points are equidistant to the center point, α must be equal to $\sqrt[4]{2^k}$, 2^k being the number of factorial points [71]. The number of design points for a CCD can be determined as follows:

$$N = 2^k + 2k + n_c \tag{2.2}$$

CCD is a valuable tool when designing experiments, as it allows for an efficient understanding of multiple factors' effects whilst minimizing the data necessary to do so. After analysing the results using CCD it is possible to organize the data in response surface plots and the respective contours. A generic representation of said plots can be viewed in Figure 2.20.

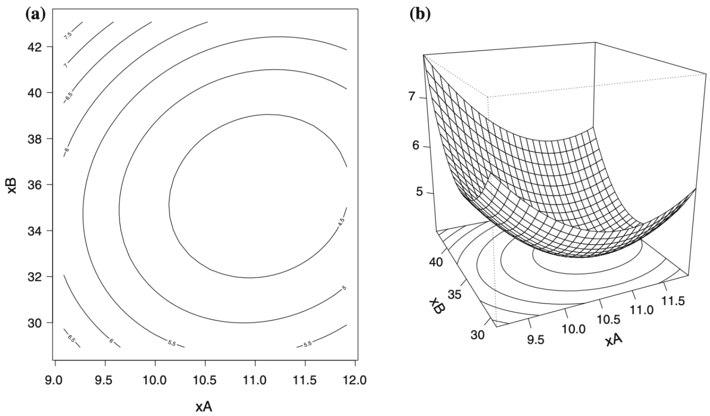

Figure 2.20: Possible response surface contour plot (a) and respective response surface plot (b) of a second-order model, adapted from [72].

Chapter 3

Experimental Development and Methodology

In this chapter, there will be a presentation and description of the base materials, equipment, procedures, and methodologies used to produce and study the dissimilar FSW joints.

3.1 Material Characterization

For the FSW joints performed, the base materials used were: an aluminum–magnesium–silicon alloy, AA6082-T6 with 2 mm thickness, and an engineering-grade polymer, reinforced with 20% of short glass fibers, composed by a blend of polyphenylene ether (PPE) and high impact polystyrene (HIPS), NORYL^{TM} GFN2 with 5 mm thickness.

3.1.1 AA6082-T6

As stated above, the metallic base material for the dissimilar joints produced was the Aluminum Alloy 6082-T6 in 2 mm sheets. Presented are the thermo-mechanical properties, in Table 3.1, and the chemical composition, in Table 3.2.

Table 3.1: Thermo-mechanical properties of AA6082-T6 [73, 74].

ρ $[\mathrm{g/cm^3}]$	E $[\mathrm{GPa}]$	UTS $[\mathrm{MPa}]$	Yield Tensile Strength $[\mathrm{MPa}]$	ε_{break} $[\%]$	HV	K $[\mathrm{W/(m.K)}]$	T_{melt} $[^\circ\mathrm{C}]$
2.70	70	290	250	10	118	170	580-650

AA6082 belongs to the series 6XXX of aluminum alloys, characterized by having magnesium and silicon as the main alloying constituents. These are medium-strength aluminum alloys and when compared to other series, such as 2XXX or 7XXX, have higher weldability, formability, and resistance to corrosion and lower cost [75]. Because of its chemical composition series 6XXX can undergo heat treatments to be strengthened. In particular, the T6 condition in AA6082-T6 is obtained through solution heating to 530-550 ºC followed by artificial aging at a temperature of approximately 170-200 ºC [76]. Because of all these characteristics, AA6082-T6 is a good match to be processed through FSW and raises interest in both the aerospace and automotive industries.

Table 3.2: Chemical composition of AA6082-T6 [74, 77].

Al [%]	Cr [%]	Cu [%]	Fe [%]	Mg [%]	Mn [%]	Si [%]	Ti [%]	Zn [%]	Others [%]
$95.2-98.3$	≤ 0.25	≤ 0.10	≤ 0.50	$0.60-1.20$	$0.40-1.0$	$0.70-1.30$	≤ 0.10	≤ 0.20	≤ 0.15

3.1.2 NORYL™ GFN2

As stated above, the polymeric base material for the dissimilar joints produced was NORYL™ GFN2. NORYL™ is the name of a group of material blends of PPE (polyphenylene ether) and HIPS/PS (polystyrene). Shown to combine characteristics as good chemical (acids, bases, cleaning agents) and heat resistance, low water absorption rates, high strength, good electrical performance, and fire retardant. Combining all these benefits with a good dimensional stability and ability to be processed, makes it suitable for a plethora of applications, including Friction Stir Welding [78, 79].

The specific material used in this study was NORYL™ GFN2 (SABIC Innovative Plastics, Saudi Arabia), supplied by PHT (Plastiques Hautes Technologies, France) is an amorphous blend of thermoplastics with a random distribution of short glass fibers (20 wt.%) and its thermo-mechanical properties can be seen in Table 3.3. For FSW application, the thermoplastic characteristic of the material is essential and the glass-fiber reinforcement allows for better performance of the final joint [78, 79].

Throughout this document, NORYL™ GFN2 will be referred to as NORYL™ or polymer, interchangeably.

Table 3.3: Thermo-mechanical properties of NORYL™ GFN2 [73, 78, 79].

$\boldsymbol{\rho}$ $[\mathrm{g/cm^3}]$	$\boldsymbol{E}$ $[\mathrm{GPa}]$	Tensile Stress at break $[\mathrm{MPa}]$	$\boldsymbol{HV}$ $[\mathrm{H358/30}]$	$\boldsymbol{K}$ $[\mathrm{W/(m.K)}]$	$\boldsymbol{T_{soft}}$ $(\ RateA/50)\ [°\mathrm{C}]$	$\boldsymbol{T_{melt}}$ $[°\mathrm{C}]$
1.25	6	80	100	0.26	145	280-300

3.2 Joint Geometry

For this study, the base materials sheets were placed in an overlap configuration with 40 mm. The aluminum sheets were cut into 300x125x2 mm plates, in the direction of the grain, and the polymer into 300x125x5 mm plates. As shown in Figure 3.1, in this overlap configuration, the AA6082-T6 plate was placed on top of the NORYL™. Following the work previously done [80], where initial feasibility tests were done to understand the best placement for the materials, in regards to the movement of the tool, the aluminum sheet is located on the RS, and the NORYL^{TM} sheet on the AS.

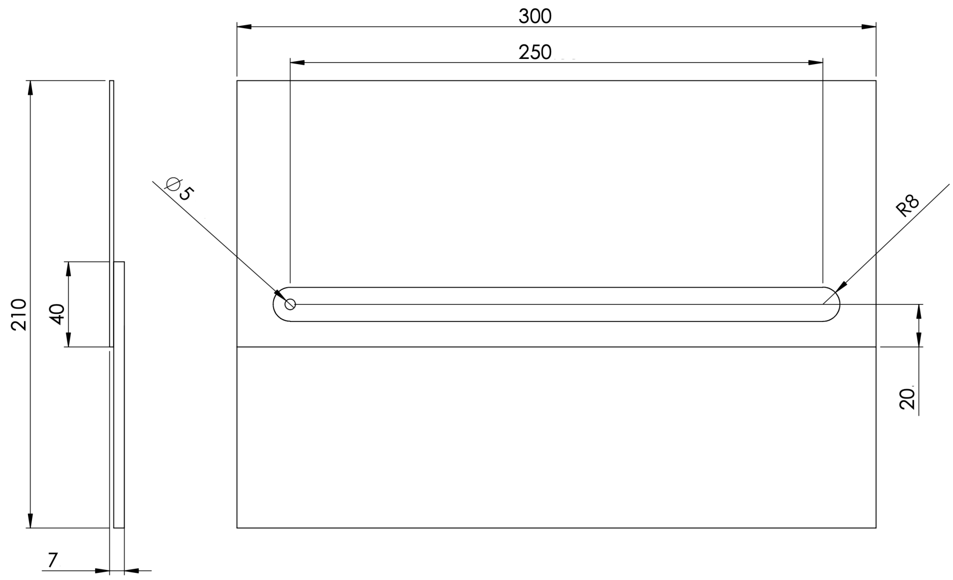

Figure 3.1: Joint configuration with 40mm overlap length (dimensions in [mm]).

3.3 FSW Equipment

To perform the FSW joints, the machine used was a custom FSW machine from UMAI, Unidade de Monitorização Avançada e Integridade Estrutural, at the Institute of Science and Innovation in Mechanical and Industrial Engineering (INEGI).

3.3.1 FSW Machine

The machine, depicted in figure 3.2, can be segmented into two main moving groups, the support table and the body of the machine. The support table has a single degree of freedom (X-axis), and the body has two degrees of freedom (Y and Z-axis). Furthermore, the body can also be adjusted to have a specific degree of inclination in regard to the support table.

All parameters, except the tilt angle which is manually defined, are defined and controlled through the software interface which complements the machine. Further explanations are present in Subsection 3.4.4.

The machine is completed with refrigeration, lubrication, and hydraulic units. This last unit controls the hydraulic cylinder which is responsible for locking the fitting attachment in place. This machine offers the capability to be controlled either in position or force modes.

Finally, the software registers all the data acquired by the machine sensors throughout the FSW process.

Figure 3.2: FSW machine axis.

3.3.2 FSW Tool

As this work is a continuation of previous studies [80, 81], the tool's geometry, presented in Figure 3.3, was kept the same. In order to make it compatible with the machine described in Subsection 3.3.1, a new tool was designed and fabricated.

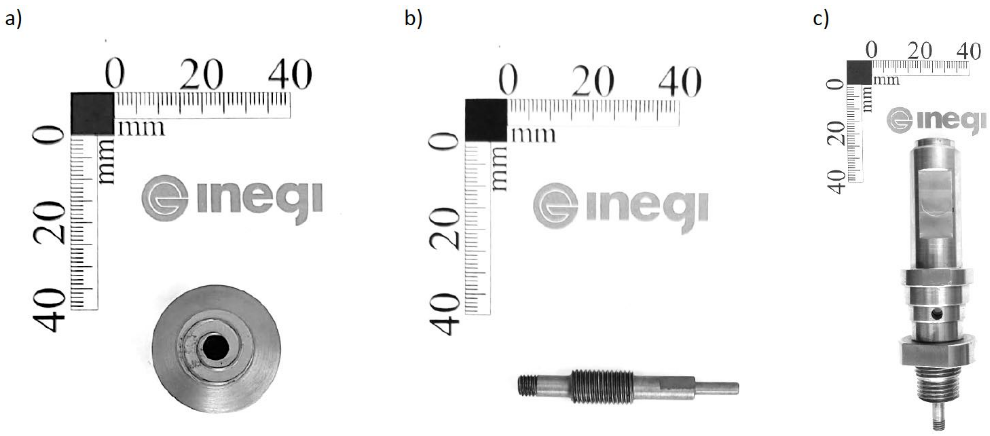

Figure 3.3: FSW Modular Tool a) Shoulder b) Pin c) Body.

The design of the tool followed a modular philosophy, being composed of three components: a threaded cylindrical shoulder with 16mm of diameter, a threaded pin with 5mm of diameter, and the body of the tool, which attaches the previous two parts. Both shoulder and pin were fabricated of AISI H13 tool steel and the body of DIN Ck45 steel. Since the length of the pin is not an object of study, it was kept at a 2 mm length, from the surface of the shoulder. This length was chosen based on the optimal results from previous studies [10, 80, 81].

3.4 FSW Experimental Procedure

3.4.1 Materials' Preparation

To prepare the base material plates, marks were drawn to determine the location of the centerline of the weld and a distance of 15 mm to each side, as depicted in Figure 3.4. These markings aided in the positioning of the clamping system and thermocouples, as well as with the positioning of the tool. Next, a small indentation was made at the thermocouples' location, explained in Subsection 3.4.3. The last step was to degrease the surfaces of the materials with ethanol.

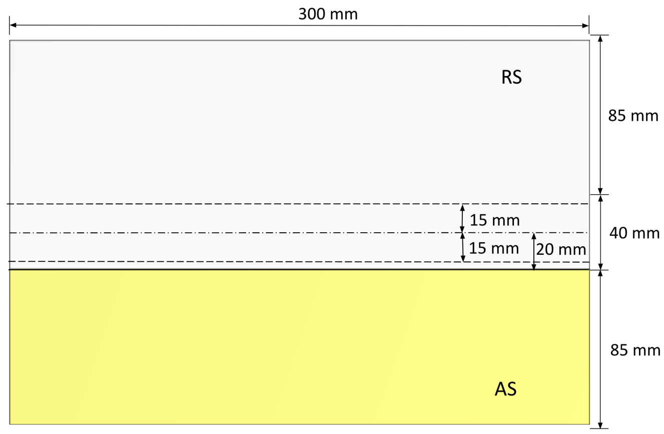

Figure 3.4: Clamping system guideline marks diagram.

3.4.2 Clamping Setup

The main goals of the clamping system are to immobilize the sheets under processing and to mitigate the generation of residual stresses by reducing distortion of the materials. Both vertical and horizontal restrictions must be applied to this end. To increase the quality of the welds produced it is crucial to have an appropriate clamping system otherwise, the plates will tend to rotate with the tool's movement or separate from each other, vertically, compromising the final joint.

As seen in Figure 3.5 b), the setup used throughout this work comprises a backing plate, two clamping bars, and six clamping points. The function of the support plate is to protect the machine's table, support the materials under processing, and aid in the clamping. Four of the six clamping points are screwed to the backing plate and are located at the edges of the two clamping bars. Each clamping point is composed of a height wedge, a fixation block, and a bolt and ring. The final two clamping points are placed in the center of the clamping bars. Given the size of the backing plate, these points must be screwed to the machine's table itself. In order to prevent further distortion, these points were fastened using a dynamometer wrench, using 5 N as the benchmark for all the clampings. The clamping system was already available and not specifically made for this study. Adjusting tabs were used to level the sheets and make them parallel with both the clamping bars and the backing plate. Lastly, to prevent horizontal movements of the materials, the clamping system of the support plate was adjusted to have a tight fit around the dimensions of the plates, immobilizing them in both X and Y directions.

3.4.3 Thermal acquisition system

In Subsection 2.2.2, the importance of studying the temperature field and its variation was explained. Following that, an assessment of the thermal behaviour was performed for all the joints produced to find if and how the thermal variation affects the FSW procedure, and the quality of its produced joints.

As seen in Figure 3.5 a), seven K-type thermocouples were used at a time. Six were placed on top of the aluminum sheet, three on each side of the weld, distanced from each other 75 mm, leaving the seventh outside the welding site to serve as the control for the ambient temperature.

Before every weld, a check of the thermocouples was made to ensure they were all working properly and were not damaged during the previous experiment. As described in the *Materials' Preparation*, Subsection 3.4.1, a small indentation was made on the aluminum to help anchor the thermocouples in their place. After clamping the materials, a provisional placement was set using paper tape, fixating the cables to the clamping bars. This made sure that the cables were not under tension when placing the thermocouples and prevented further errors. A small drop of thermal paste was used to promote a good connection between the thermocouple's wire and the metal sheet. Finally, a piece of electrical tape was put down to create a tight seal between the thermocouple, the aluminum sheet, and the thermal paste. The final placement can be seen in Figure 3.5 b).

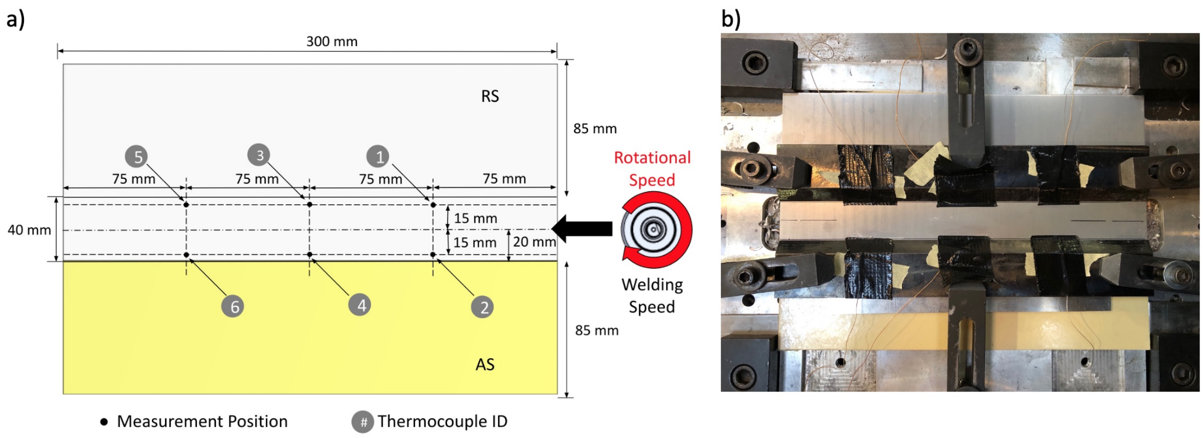

Figure 3.5: a) Thermocouples' position diagram, b) Thermocouples' placement during FSW.

To acquire the thermal data the thermocouples were connected to a NI cDAQ-9181 Ethernet chassis coupled with a C series module. To record the thermal measurements the *NI SignalExpress 2013* software was used. A data acquisition rate of 70 Hz was established to guarantee that enough data was recorded. Afterward, a .txt document was extracted in which the time, in seconds, and temperature for each thermocouple, in degrees Celsius, was recorded.

3.4.4 FSW Process

This specific FSW process was developed following the general procedure introduced in Subsection 2.1.4, as well as similar work done previously [10, 80, 81].

The process begins with the preparation of the materials, as described in Subsection 3.4.1, followed by the clamping setup, described in Subsection 3.4.2, with the joint configuration depicted in Figure 3.1 and lastly, the installation of the thermal acquisition system, described in Subsection 3.4.3.

Before the welding process itself begins, parameters must be defined. Figure 3.6 shows the menu in which the following parameters must be defined, "FSW MANUAL": material, spindle, trajectory and penetration, reference points, control, and registry. Whilst most parameters are defined beforehand, the reference points must be manually inserted before each run.

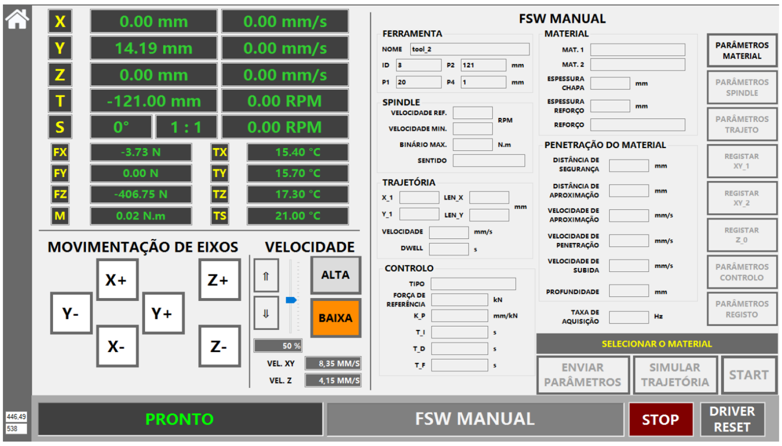

Figure 3.6: Variables' definition menu for manual FSW [82].

To define the beginning point, the marks described in subsection 3.4.1 were used to find the center of the weld leaving a distance between 15 and 25 mm to the end of the plate. At this point, the height, Z_0, was also defined with the help of a feeler gauge. Next, the endpoint was chosen. Even though the weld is a straight line between the beginning point and the end, for additional verification of the placement of the clamping system, the endpoint was defined the same way as the beginning one. Finally, the variables to be registered were chosen as well as the name of the file to be created, which complied with the following structure, *"DOE_BM_JointID#_ω_v_tilt"*

Prior to beginning the welding procedure, a mandatory trajectory simulation must be performed. During this simulation, the tool goes through the path of the weld without rotation and at a height of 5 mm above the Z_0. During the welding process, a constant watch must be kept on the scene to prevent accidents to both the materials and the machine itself.

Afterwards, the newly joined plates were left to cool down still clamped to the machine's table, as a measure to try to prevent additional deformation or distortion from happening.

3.4.5 Central Composite Design - Application

As introduced previously, in Section 2.3, an appropriate experiment design is a key factor when trying to optimize the study of parameter variations with overall joint quality. With such knowledge, this study was conducted with the intent of studying three input variables: i)rotational speed, ii) welding speed, and iii) tilt angle.

Following the central composite method (CCD), explained in Subsection 2.3.1, the knowledge from previous studies on the same matter [10, 73, 80, 81] and an array of studies introduced in Section 2.2, the matrix of parameters defined is presented in Table 3.4.

Table 3.4: Parameters defined through CCD for the DoE of FSW joints.

Joint ID	Parameters		
	ω[rpm]	$\mathrm{v[mm/min]}$	**Tilt** [$^\circ$]
J1	600	100	2
J2	1000	100	
J3	600	140	
J4	1000	140	
J5	600	100	3
J6	1000	100	
J7	600	140	
J8	1000	140	
J9	464	120	2.5
J10	1136	120	
J11	800	86	
J12	800	154	
J13	800	120	1.7
J14	800	120	3.3
J15	800	120	2.5

The factorial points' low and high values for the rotational speed, the welding speed, and the tilt angle are 600/1000 rpm, 100/140 mm/min, and 2/3 °, respectively. The axial points are extreme values that fall outside the factorial points and are determined by applying a α factor to the low and high values. Following what was explained in Subsection 2.3.1, in order to achieve the rotatability of the experiment the α must be equal to $\sqrt[4]{2^k}$, 2^k. In this experiment, the number of factors k is 3, making α equal to 1.682. By multiplying this factor by the factorial points' high and low values, the rotational speed, welding speed, and tilt angle are 446/1136 rpm, 86/154 mm/min, and 1.7/3.3 °, respectively. The center point is defined with 800 rpm of rotational speed, 120 mm/min of welding speed, and 2.5° of tilt angle. Previous studies [10, 73, 81] already ascertained the non linear condition of this experiment. Because of that, only one joint was produced with the center point parameters.

The last parameters to be defined are presented in Table 3.5, and they are the same for all fifteen joints.

Table 3.5: Constant parameters used for the DoE of FSW joints.

Constant Parameters	
FSW Process control	Position
Rotation direction	CW
Plunge Speed [mm/s]	0.1
Plunge depth [mm]	2.2
Dwell time [s]	15

Afterward, with the results from the CCD, a statistical study was done on all fifteen joints. An analysis of variance (ANOVA) was performed to evaluate the effect of the parameters under study in both the UTL and the processing temperature. Results and their discussion can be found in Section 4.6.

3.5 Post Processing

3.5.1 Specimen Preparation

In order to perform various tests, the fifteen friction stir welded joints had to be cut into appropriate-sized specimens. A technical drawing of the specimen cutting schematic, which can be seen in Figure 3.7 as well as in Appendix A, was created and sent to A. J. Maltez - Sociedade Metalúrgica, Lda, who performed the procedure.

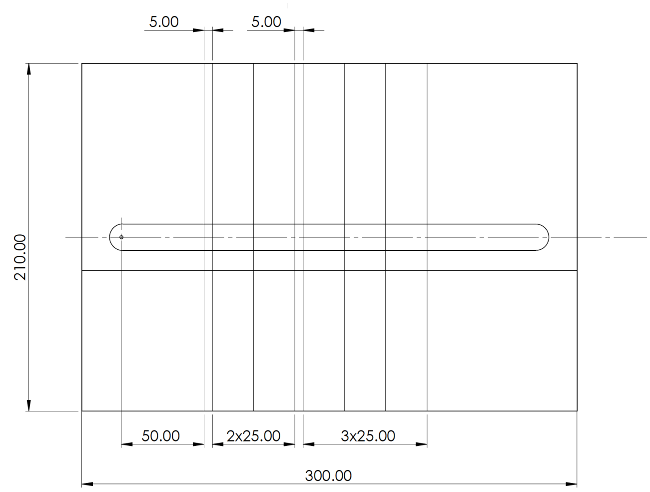

Figure 3.7: Specimen cutting schematic, all dimensions in [mm].

The plates were cut perpendicular to the weld line discarding the first 50 mm from the center of the exit weld point. One 5 mm specimen was cut followed by two 25 mm specimens, and after that another 5 mm specimen was followed by three 25 mm specimens. This alternation of specimen types was made to ensure both 5mm specimens, which will be used for microscopic analysis and hardness testing, come from distinct sections of the joint. The 25 mm specimens will be used for the quasi-static tensile testing. Each specimen was labeled, from left to right, from 1 to 7. Specimens 1 and 3 had a width of 5 mm and specimens 2, 3, 5, 6, and 7 of 25 mm.

3.5.2 Quasi-Static Tensile Testing

Preparation

For this study, all of the 25mm specimens cut from the joined plates, described in Subsection 3.5.1, were prepared. For the grip of the specimens to be done correctly, two 5.5mm holes had to be drilled in both the materials centered widthwise and distanced 85 mm from the center of the weld line, as shown in Figure 3.8. This preparation was done using the vertical milling machine available at IST's Laboratório de Técnicas Oficinais.

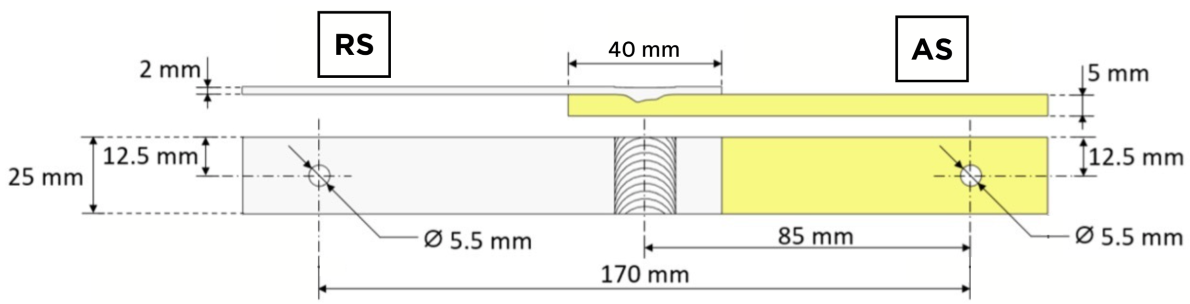

Figure 3.8: Drilling schematic [81].

Testing

Quasi-static uniaxial tensile tests were performed to determine the tensile mechanical properties, for all the friction stir welded joints. From these tests, it was determined the ultimate tensile load (UTL) and later calculated the ultimate tensile stress (UTS) and consequent joint efficiency (Eff %).

From each welded joint, all five of the 25 mm specimens, described in subsection 3.5.1, were tested.

Testing was performed at the Mechanical and Materials Testing Laboratory at IST on an INSTRON® 5566 testing machine, shown in Figure 3.9, available at IST's Mechanical and Materials Testing Laboratory. This model has a maximum load cell capacity of 10 kN. Keeping in mind the overlap geometry of the joints shims were used to align the specimens with the vertical axis of the machine. Shims of polymer were gripped with the aluminum section of the specimen, and vice versa, to make up for the difference in thickness, in order to mitigate the effects of the secondary bending moment. All tests were executed at the constant displacement rate of 5mm/min, at room temperature.

Results of the quasi-static tensile tests and their discussion can be found in Section 4.3.

Figure 3.9: INSTRON® 5566 testing machine and specimen grip detail.

3.5.3 Microscopic Analysis

Preparation

From all the friction stir welded joints, three were chosen to undergo microscopic analysis. As described in Subsection 3.5.1, 5mm specimens were cut from all joints, although only three were studied. In order to perform the desired microscopic analysis the 3 samples had to be correctly prepared. From the 210 mm long specimens, a smaller specimen was cut in order to fit inside the 25 mm mold, without compromising the cross section to be studied. The specimens were placed inside the molds which were then filled with approximately 40 ml of epoxy resin mixed with 4.8 ml of hardener to later be left to harden for 12 hours. After hardening, the samples were polished with sandpaper grades ranging from 240 to 2400 grit, for 2 to 3 minutes each. The polishing process was monitored with an optical microscope. Following the first polish, a cloth disc with polishing gel was used, as well as a silica disk, to attain the desired finish sample. As a last step, the specimens were placed in an ultra-sonic bath to remove silica residues. In order to see the aluminum grain boundaries, the samples were contrasted with Keller's reagent which is composed of distilled water, nitric acid (HNO3), hydrochloric acid (HCl), and hydrofluoric acid (HF). This preparation was performed at IST's Material Characterization Laboratory.

Testing

To analyse the microstructure, a combination of scanning electron microscopy (SEM) and energy-dispersive spectroscopy (EDS) was performed, on the three specimens prepared, using the Thermo Scientific Phenom Prox G6 at IST's Electronic Microscopic Laboratory. SEM was performed at a magnification of 500x and 1500x to analyse the morphology of the interface between the materials, on at least six regions per specimen. EDS, on the other hand, used to the chemical elements in a particular area, was performed between four and eight times per specimen, when deemed necessary.

Furthermore, macroscopic analysis of the cross section of the tensile test specimens was done, after these were tractioned. This was done using the Digital OPTIKA Microscope at IST's Mechanical and

Materials Testing Laboratory. After the images were attained, the SolidWorks software was used to measure and analyse the dimensions and geometry of the joints.

Findings from the microscopic analysis and their discussion can be found in Section 4.4.

3.5.4 Hardness Test

Preparation

Similarly to the preparation made in Subsubsection 3.5.3, for the microstructure analysis, 3 samples were also studied. In total, three samples were prepared using the same molds, resin, and polishing regiment. No Keller reagent was used in this case. This preparation was also performed at IST's Material Characterization Laboratory.

Testing

To perform the hardness tests the Shimadzu HMV-2 machine, available at IST's Mechanical and Materials Testing Laboratory, was used. To conduct this hardness test an indentation was made, on the specimens, with a load of HV 0.2 (0.2 kgf) or HV 1 (1 kgf), depending if the testing sight was on the polymer or the aluminum, respectively. The indentations were made along three defined trajectories, for a period of 15 seconds each.

Results of the hardness Vickers tests and their discussion can be found in Section 4.5.

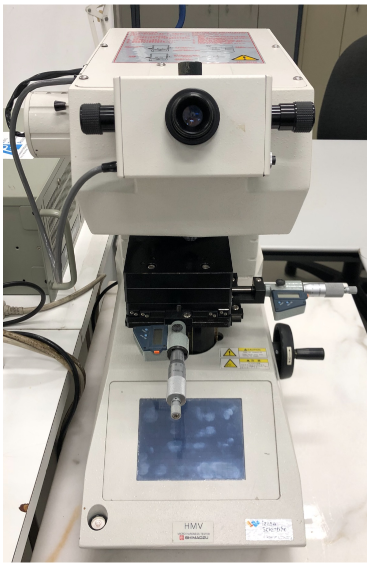

Figure 3.10: Shimadzu HMV-2 machine.

Chapter 4

Experimental Results

This chapter presents the experimental results obtained and the consequent analysis and discussion. It is divided into six sections, an evaluation of the produced joints, the processing temperature finding, the quasi-static tensile tests' results, followed by the microstructure analysis of the joints' interface, the results from the hardness tests, a statistical analysis of the temperature and quasi-static tensile results and finally, the presentation and analysis of the resulting optimization joints.

4.1 Produced Joints

In this section, a general evaluation of the joints' surface produced will be made. A more detailed analysis of the morphology of the joints will be carried out in Section 4.4 where a thorough analysis of the cross section's macro and microstructures will be evaluated. Firstly, a comprehensive comparison between the different joints' surface morphology will be made in an attempt to find relations between the overall quality of the joints.

When beginning this kind of analysis it is imperative to establish a benchmark of what is expected to be the outcome, based on the available literature and previous studies. Based on the literature review presented in Section 2.2, it would be anticipated that the surface quality would be relatively rough, exhibiting a mixture of resolidified polymer and aluminum fragments on the weld line, as well as a degradation of the underlying joint surface. Although this is true for many studies [1–3, 5–9], it does not mean that it is the only outcome available. This current thesis derives from previous studies [10, 73, 80, 81] where, for many combinations of parameters, an unmixed weld line was achieved, and joints with fairly good surface quality were produced.

Following the methodology presented in Section 3.4 and the parameters defined in Table 3.4, fifteen friction stir welded joints were produced. Figure 4.1 shows all fifteen weld lines, just after the FSW process.

The first evaluation of the joints was performed as they were removed from the clamping setup. As expected from the range of parameters chosen, and from a visual standpoint, all joints had solid connections. No misalignment of the material sheets was detected and no significant gaps along the seam parallel to the joint.

Figure 4.1: Weld line of the FSW joints, a) J1, b) J2, c) J3, d) J4, e) J5, f) J6, g) J7, h) J8, i) J9, j) J10, k) J11, l) J12, m) J13, n) J14, o) J15.

As introduced earlier in Subsection 2.1.4, the polymeric material goes through a softening process due to the heat generated by the tool, during the FSW process. As it softens, it becomes more and more malleable, allowing it to join with the aluminum. However, if this softening is excessive or if the vertical force, present during the passing of the tool, is excessive, there will be an extrusion of the material, from the weld line to the sides of the weld. Overall this was avoided for the joints under study. The most significant example of this happened for J13, where a significant amount of NORYL^{TM} overflowed through the overlapping interface of the materials, as seen in Figure 4.2 a) and b). For the remaining joints, this event was minimal and, when present, was contained to the interface of the materials parallel to the weld line, primarily closer to the beginning of the weld. J4, showcased in Figure 4.2 c) and d), had no polymeric extrusion whatsoever. This phenomenon, although small, is adverse to the joint's performance as it removes material from its original location and reduces its thickness in comparison to the nominal value.

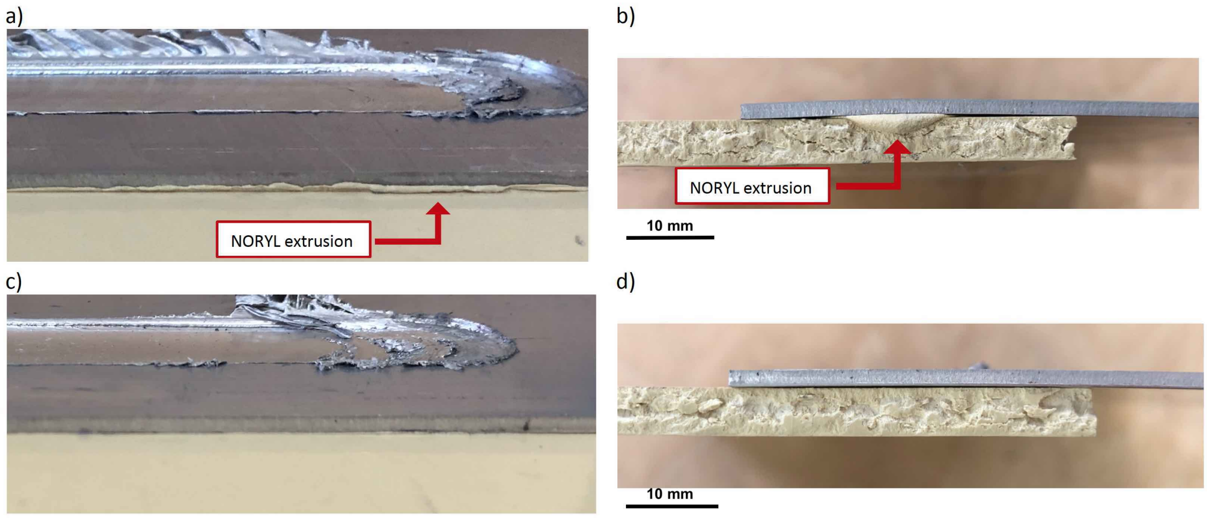

Figure 4.2: NORYL^{TM} overflow, a) J13 side, b) J13 top, c) J4 side, d) J4 top.

A common defect that affected two-thirds of the joints was the disruption of the surface of the weld at the initial point. As portrayed in Figure 4.3, this happened in various degrees, from no irregularities to extrusion of NORYL^{TM} through the aluminum material. Of the fifteen joints, J10 which had the most rotational speed at 1136 rpm had the worst defect, J5/J7/J9/J12/J15 with rotational speeds ranging from 464 to 800 rpm had no defects, and the remaining joints had some degree of it. For this phenomenon to occur, there must be some disturbance of the aluminum for it to "separate" from itself. The main culprit for this is the the dwell time that, when combined with higher rotational speed, delivers too much heat to a single location exacerbating the softening of the materials and promoting their disruption. When sufficient, this phenomenon allows for the polymeric material, which in this case is located 2 mm below the joint's surface (the thickness of the aluminum sheet), to escape the joint and resolidify outside the weld. If there was a concrete application for this process, where no post-processing was intended to be done, the dwell time should be studied to optimize its potential. This occurrence does not appear to have a direct impact on the joints' performance, since no specimens were retrieved from this section.

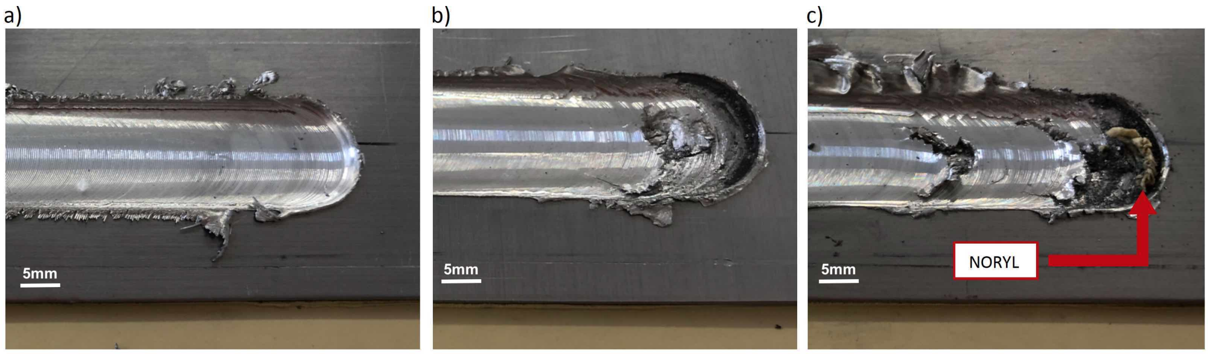

Figure 4.3: Initial defect for joints with varying rotational speeds a) J9 (464 rpm), b) J14 (800 rpm), c) J10 (1136 rpm).

Overall, the surface quality of the weld line was very good for all the joints. When undisturbed, the surface of the weld line is fairly smooth as it is only comprised of processed aluminum material. And that was the case for all the joints produced. Despite this, the surface can never be as smooth as the base material unless some kind of post-processing polishing procedure is performed. The texture of the weld line is characterized by a semicircular pattern produced by the translation of the tool which travels with rotational speed. This texture becomes finer as the rotational speed increases. For a rotation of 1000 rpm, there were no significant differences among the joints. On the other hand, for a rotation of 600 rpm, the texture improved at a lower welding speed of 100 mm/min, as was the case of J1, when compared to J3 which had a welding speed of 140mm/min. This was expected, as a lower welding speed allows for more rotations of the tool, at any given spot, allowing time to smooth some of the irregularities. Lastly, for both low and high welding speeds, there was an improvement of the texture for joints with higher rotational velocities, as was the case for J2 and J4 when compared to J1 and J3, respectively. All of these comparisons were done with the naked eye, and as such very good joints like J4, J8, and J10 look fairly similar. Despite that, J10 appears to have the best surface quality at a rotational speed of 1136 rpm. A varying range of the quality of the weld line can be seen in Figure 4.4.

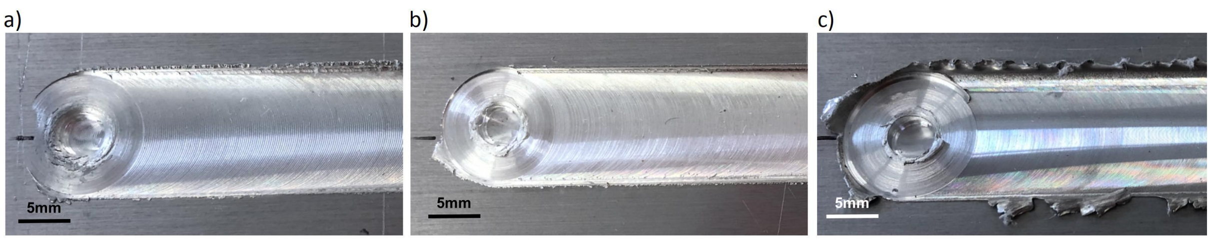

Figure 4.4: Surface quality of the weld line, ranging from coarser to smoother a) J3, b) J4, c) J10.

As explained in Subsection 2.2.6, the key-hole or exit defect is a common appearance in friction stir welded joints with a protruding pin in the tool geometry. For all the joints, the pin was kept at a 2mm length from the shoulder base, making this defect similar from J1 to J15. To mitigate this defect, without changing the geometry of the tool, there would have to be a secondary process to eliminate it. In this study, and considering that no specimens were made from either end of the weld line, this was not a necessary step.

The Subsection referenced above also introduced the flash defect. This defect is known to be more prevalent in joints with an increased plunge depth and/or high heat input. In terms of flash, two joints stand out, J10 and J13. J10 produced a significant amount of flash but only in the first section of the weld. Referencing back to its processing parameters, 1136 rpm, 120 mm/min, and 2.5 $^\circ$, the explanation seems fairly straightforward. With this being the joint with the highest rotational speed, and remembering that the dwell time was the same for every other joint, measured at 15 s, the amount of heat generated in the first location was large enough to excessively plasticize the aluminum and promote its escape from the weld line. As the tool began its welding movement, the heat input dissipated enough so that the flash defect was mitigated for the rest of the length of the weld. In the case of joint J13, the parameters were 800 rpm, 120 mm/min, and 1.7° . Here, with the lowest tilt angle, the surface of the shoulder in constant contact with the material is greater, increasing the friction and consequently the heat input. Moreover, this lower angle promoted a dragging action which moved the aluminum along the weld line and into its sides. Because of this, the flash was not contained to a certain section, like in J10, but it prolonged itself throughout the weld line. For the other joints, minimal to no flash was registered, with the most common event being the appearance of fine metal shavings as the tools grazed the surface of the aluminum, and that were never connected to the weld line.

Crossing the information presented previously, the joint with the overall best quality is J8, combining no NORYL^{TM} or aluminum flash with a good surface finish. J13 comes last in the overall evaluation, due to the amount of polymeric and metallic flash and the presence of an initial defect.

After processing the joints and cutting the specimens, the cross section of the weld becomes visible. Some of those specimens were processed even further and were embedded in resin, as explained in Subsections 3.5.3 and 3.5.4. Figure 4.5 a) shows cross section the J4 specimen for the hardness tests and Figure 4.5 b) for the microscopic analysis.

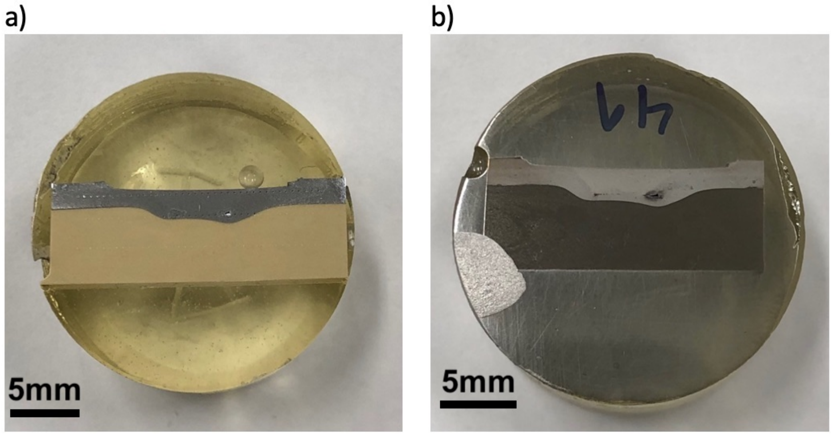

Figure 4.5: Cross section of J4 specimens a) hardness testing, b) microstructure analysis.

Previous studies on this subject [73, 81] found three main configurations for the joint's cross section. As depicted in Figure 4.6, type I is characterized by a single concavity at the interface in contrast to type II which has a double concavity at the interface, and finally, type III, which does not present aluminum continuity and in its place has a mixture of aluminum fragments and resolidified polymeric material.

The studies reviewed in Section 2.2 presented mainly type III [2, 3, 5–9]. Although common, this is not the best type of cross section as it does not retain the properties of either material due to the lack of continuity. Furthermore, even though the contact area between the materials is increased due to the fragmentation of the aluminum, this does not promote an improvement in the bonded area as it increases the likelihood of the appearance of pores and voids in the matrix.

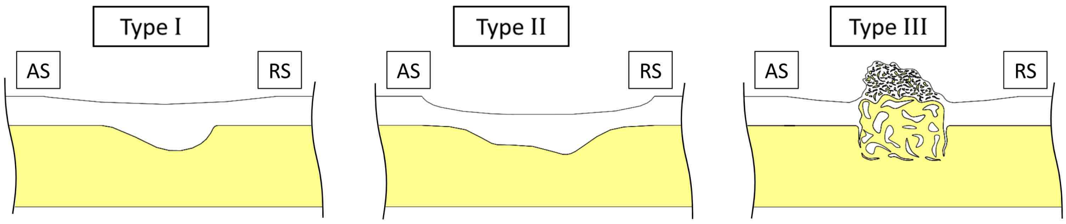

Figure 4.6: Cross section morphology types, adapted from [81].

Figure 4.7 shows the cross section of joints J1 through J15. All fifteen joints have a type II morphology with two concavities at the interface of the materials. The presence of this double concavity improved the mechanical interlocking by increasing the bonded area without breaking the continuity of the materials, allowing for an improved bonding of the joint.

The concavity of the RS tends to be more prominent on the RS in comparison to the AS. This is caused by the increased plastic deformation flow that exists in the AS paired with the tendency for lower temperatures to develop in the RS. The plasticized material flows from the AS and tends to pool in the RS. All joint concavities were measured in relation to the distance to the base of the NORYL^{TM} sheet. In all but three, the RS concavity ended closer to the base of the NORYL^{TM} sheet meaning that it was the larger concavity. J6 presented two cavities of the same size, whilst J5 and J8 had larger concavities on the AS than the RS. These last two joints had a lower-than-average mechanical performance, as will be presented in Section 4.3. All three joints were on the lower average of temperatures recorded, as will be presented in Section 4.2. There could be a relation between mechanical performance and the morphology of the cross section, for that to be understood, further studies should be done to verify said relation.

In regards to defects in the cross section, a small but present closed tunnel was formed in all fifteen joints, mostly located in the RS. This can be better seen in Figure 4.5 a). This volumetric defect is fairly common in joints of this type. There is a noticeable reduction in the size of the tunnel defect in this study when compared with previous ones, with the same set of materials [80, 81].

Figure 4.7: Cross section measurements of one specimen from joints a) J1, b) J2, c) J3, d) J4, e) J5, f) J6, g) J7, h) J8, i) J9, j) J10, k) J11, l) J12, m) J13, n) J14, o) J15.

4.2 Processing Temperature

In Subsection 2.2.2 was introduced that one of the most determining factors, when trying to achieve a robust metal-polymer composite joint, is the processing temperature during the FSW process. FSW processes rely heavily on heat generation and distribution which comes from i) the friction that exists between the tool and the base materials and ii) the plastic deformation which ultimately enables the joint's formation [73, 83, 84].

As explained in Subsection 3.4.3, the three pairs of thermocouples were placed on the surface of the aluminum sheet, recording its temperature during the procedure. At first glance, this could seem like a rough approximation, given that the location of interest during the joining process resides in the materials' interface. However, according to previous studies [81], where the same set of materials were joined, producing a similar geometry joint with parameters that fall inside the scope of the current study, it was found that the reduction of the temperature from the surface of the aluminum to the interface of the materials was less than 0.2 °C. In summary, this happens because of the difference between the thermal conductivity of the base materials. AA6082-T6 has a thermal conductivity of 170 $\mathrm{W/(m.K)}$ whilst NORYL$^{\mathrm{TM}}$ only has 0.26 $\mathrm{W/(m.K)}$, values presented in Section 3.1. This property means that even though in the previous work [81], the temperature of the aluminum reaches peak temperatures between 199 °C and 310 °C, the temperature recorded on NORYL$^{\mathrm{TM}}$'s bottom surface only got to 24 °C to 39 °C and the calculated temperature of the interface surface was approximately the same as the aluminum's. Using this information, the temperature recordings from the surface of the aluminum sheet were considered to be a valid estimate of the temperature in the interface.

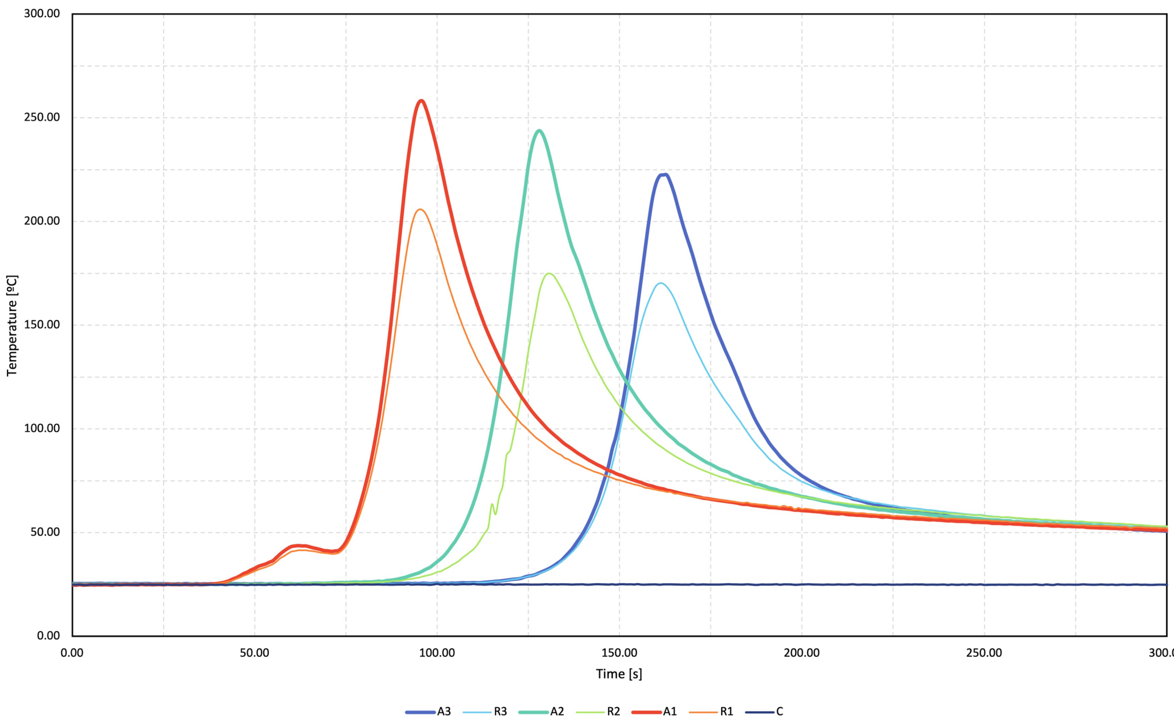

Figure 4.8: Temperature distribution measured by the thermocouples during FSW process of joint 3.

Figure 4.8 depicts the temperature distribution registered by the thermocouples during the FSW process of joint J3. In it are represented the temperatures captured by the three AS thermocouples (A#) as well as the three RS thermocouples (R#) and also the control thermocouple (C) which measured the ambient temperature. The temperature distributions for the remainder of the joints can be seen in Appendix B. During the production of joints 1 to 15 the ambient temperature was lowest in the morning, at 23.7 °C, and highest in the afternoon, at 24.9 °C. However, as it will become evident in Section 4.7, the ambient temperature will prove to have a greater impact on the FSW process than initially considered.

As a result of the temperatures registered throughout the totality of the FSW process, Figure 4.9 portrays the peak temperature achieved by the thermocouples and the correspondent melting a softening temperature of NORYL^{TM}. More particularly, Figure 4.9 c) is a direct result of the temperatures displayed in Figure 4.8 about joint J3. Both graphics are a good representation of a possible temperature distribution during the FSW process for the range of parameters under study.

Table 4.1 presents all the AS and RS peak temperatures graphically displayed in Figure 4.9, whereas Table 4.2 presents the peak temperature averages for the advancing and retreating side.

Table 4.1: Peak temperature registered by each thermocouple for joints J1 to J15 [°C].

	A1	**A2**	**A3**	**R1**	**R2**	**R3**
J1	234.03	245.63	251.19	242.15	249.46	229.04
J2	245.36	270.14	246.18	260.29	219.50	230.69
J3	258.12	243.91	222.52	205.81	174.90	170.35
J4	243.77	265.19	245.61	213.24	280.06	247.72
J5	196.00	196.15	218.70	139.90	105.12	189.11
J6	245.24	219.54	221.15	137.23	194.49	186.54
J7	212.75	200.90	167.49	208.48	225.60	238.14
J8	220.69	254.39	248.25	171.12	194.72	194.54
J9	242.18	218.15	227.44	178.02	205.89	225.07
J10	306.07	244.17	280.87	184.26	229.63	216.74
J11	227.46	241.11	239.25	213.63	27.98	176.92
J12	246.19	266.69	251.59	219.60	173.10	240.64
J13	223.91	283.24	267.68	246.79	211.37	211.92
J14	232.99	266.69	246.15	229.76	228.21	180.88
J15	244.28	191.84	249.42	216.48	202.76	227.93

Comparing the average temperatures for each side, the common denominator is that, on average, the AS temperature is higher than the RS. This observation is in line with Yan *et al.* [4], reviewed in Subsection 2.2.2, as well as other studies analysing temperature measurements for FSW [73, 85], and can be justified by an increased plastic material flow on the AS, when comparing it to the RS, due to the higher velocity gradient present on this side. An outlier to this observation is J7 which has a higher RS temperature. No cause was found to justify this, other than the possibility of user error when placing the thermocouples, as this was the last joint to be produced. As it will become apparent further on, J7 will be the second to worst performing joint in the mechanical tests, and this could be a reason, although no concrete evidence was found.

Correia *et al.* [73] proposed a hypothesis where the minimum temperature, which enables the proper formation of a metal-polymer composite joint, was the polymer's softening temperature whist temperatures significantly above its melting temperature could prove to be a deterrent to a properly bonded joint due to polymeric overflow. Knowing beforehand that all fifteen joints were successfully jointed, and observing Figure 4.9, these results are in line with this hypothesis. Generally, the peak temperatures reside inside the boundaries of NORYL^{TM}'s melting and softening temperatures. The only joints which registered temperatures below the lower boundary were J5 and J6. Considering that they are average-performing joints, refer to Section 4.3, the most likely cause for this is the fact that they were the first joints produced, and this increased the probability that the thermocouples were not properly placed. J10 was the only joint that surpassed the melting temperature of the polymer and, as was presented in Section 4.1, at the beginning of the joint, an excessive amount of flash was present. The excess heating caused the aluminum to escape its original position and solidify outside of the weld line.

All temperature results, both in its recordings and its analysis, came in line with what was expected, prior to their recording. As will be shown in the next section, this corroborates the proper bonding of the joints produced.

Table 4.2: Average AS and RS peak temperature, for joints J1 to J15 [°C].

	AS$_{avg}$	**St. Dev.**	**RS$_{avg}$**	**St.Dev.**
J1	243.6	7.2	240.2	8.5
J2	253.9	11.5	236.8	17.2
J3	241.5	14.6	183.7	15.8
J4	251.5	9.7	247.0	27.3
J5	203.6	10.7	144.7	34.5
J6	228.6	11.8	172.8	25.3
J7	193.7	19.2	224.1	12.2
J8	241.1	14.7	186.8	11.1
J9	229.3	9.9	203.0	19.3
J10	277.0	25.4	210.2	19.1
J11	235.9	6.0	195.9	15.0
J12	254.8	8.7	211.1	28.2
J13	258.3	25.1	223.4	16.6
J14	248.6	13.9	212.9	22.7
J15	228.5	26.0	215.7	10.3

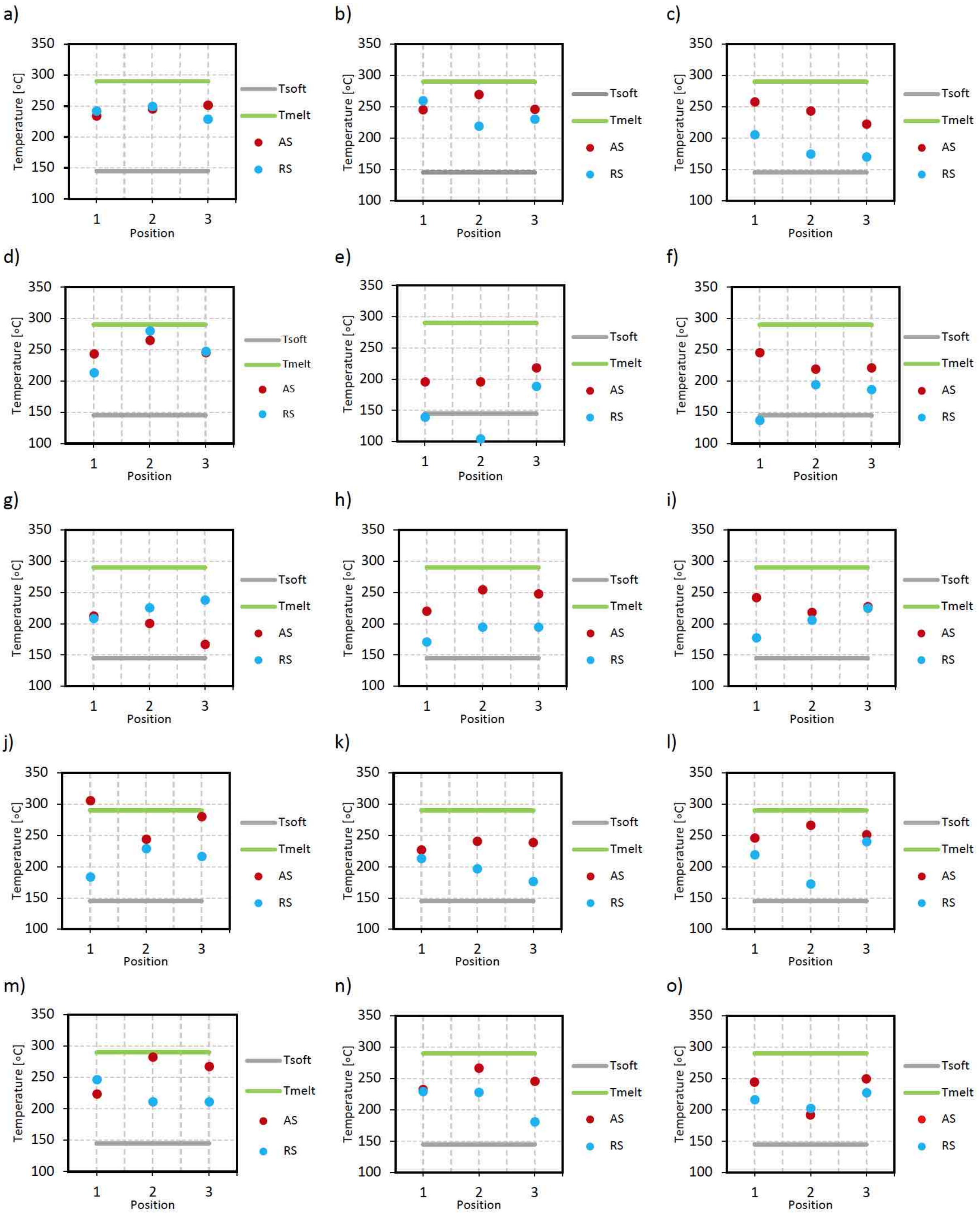

Figure 4.9: Peak temperature registered in positions 1, 2, and 3 for both AS and RS, in reference to NORYL^{TM}'s softening and melting temperatures. Results from joints a) J1, b) J2, c) J3, d) J4, e) J5, f) J6, g) J7, h) J8, i) J9, j) J10, k) J11, l) J12, m) J13, n) J14, o) J15.

4.3 Quasi-Static Tensile Tests

In this section, the results from the quasi-static tensile tests will be presented and analysed. The tests were performed in accordance with the methodology explained in Subsection 3.5.2. These results will provide insight into the global mechanical performance of the FSW metal-polymer composite joints with the end goal of displaying the relations between the parameters under study and the mechanical resistance of the joints.

Although all five specimens, from each joint, were tested, the highest and lowest results were discarded in an attempt to have a more accurate convergence of results. The Force/Displacement results can be seen in Table 4.3 and in Figure 4.10.

Table 4.3: Quasi-static tensile test results.

	UTL1 [N]	**UTL2 [N]**	**UTL3 [N]**	**Avg. UTL [N]**	**St.Dev. [N]**
J1	1990.60	2442.30	2451.60	2294.83	215.16
J2	1681.49	1691.08	1722.02	1698.20	17.29
J3	1986.98	2037.33	2481.97	2168.76	222.42
J4	3043.52	3380.77	3818.21	3414.17	317.15
J5	1716.01	1793.14	1859.59	1789.58	58.67
J6	2006.21	2363.16	2601.58	2323.65	244.66
J7	1648.86	1715.82	1759.57	1708.08	45.53
J8	1785.23	1873.17	1877.06	1845.15	42.40
J9	2365.94	2367.30	2496.68	2409.97	61.31
J10	2569.55	2776.55	2855.99	2734.03	120.74
J11	2778.09	2812.07	3176.91	2922.36	180.53
J12	2110.92	2538.51	2620.12	2423.19	223.30
J13	2654.64	2755.68	2816.74	2742.35	66.84
J14	2189.22	2241.77	2261.12	2230.70	30.38
J15	2205.62	2222.47	2621.93	2350.00	192.40

Looking at the Force/Displacement results it is obvious that J4 performed well above the rest of the joints, surpassing the 3000 N mark and reaching an average UTL of 3414.17 $\pm$ 317.15 N. Nonetheless, this was also the joint with the highest standard variation, at 317.15 N. Following J4 were J11 at 2922.36 $\pm$ 180.53 N and J13 at 2742.35 $\pm$ 66.84 N. On the other end of the spectrum was J2, bearing the least amount of load until failure, at 1698.20 N and presenting the lowest standard variation, at 17.29 N. Following J2 were J7 at 1708.08 $\pm$ 45.53 N and J5 at 1789.58 $\pm$ 58.67 N. Considering all fifteen joints, the average UTL experienced was 2337.00 N.

Regarding the displacement values of Figure 4.10, some remarks should be taken into account. Firstly, the displacement values were measured by the tensile test machine and not an extensometer, as such, these measurements are an approximation of the real value tampered by the machine's own displacement. Secondly, not all specimens incurred in an instantaneous and total fracture like all the specimens of J4 or some of the specimens of J1, J6, etc., most of the specimens had an initial fracture, that did not completely sever the NORYL^{TM} plate before the total fracture occurred. This can be seen in the "steps" the Force/Displacement curve has, before the final fracture at the peak of the curve.

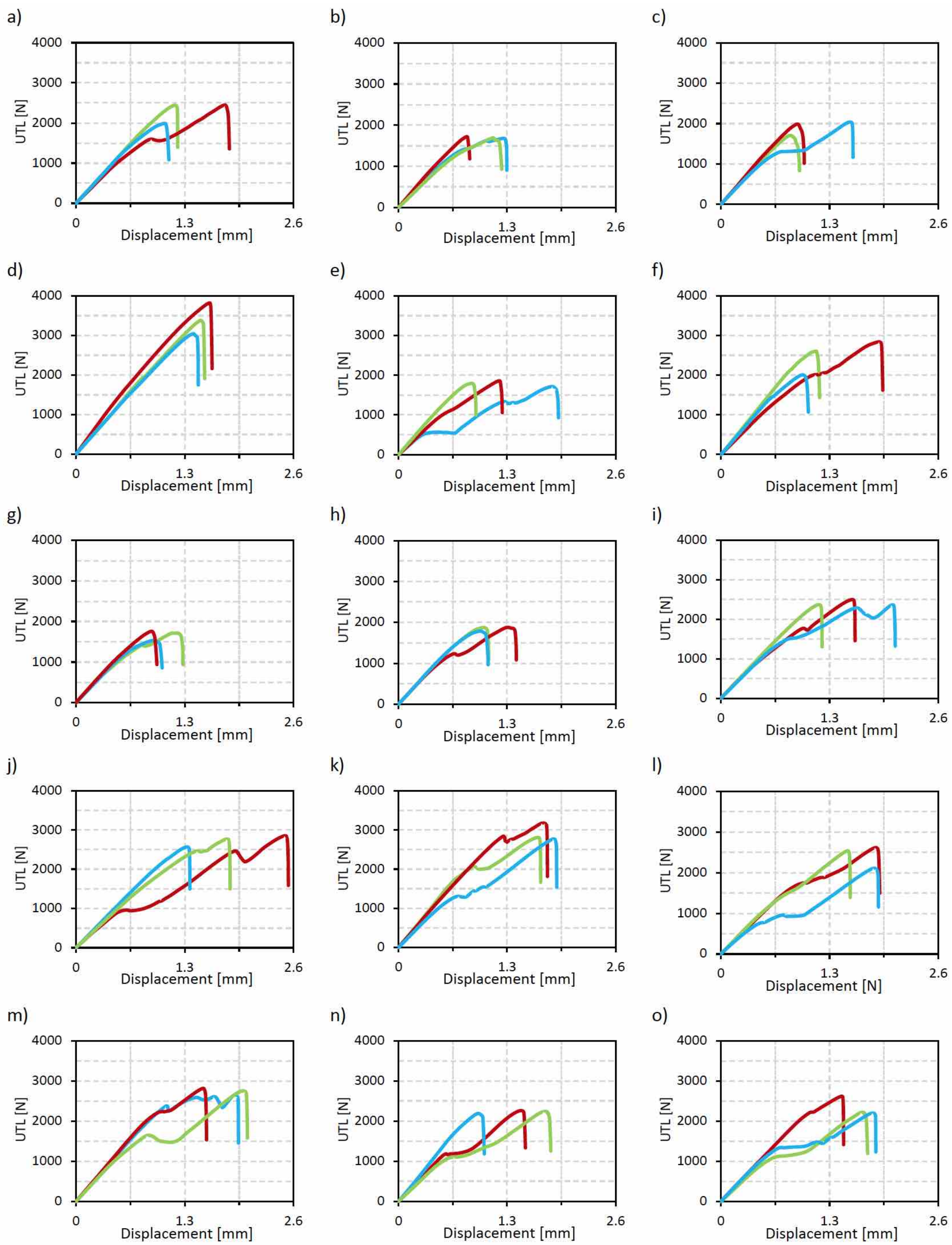

Figure 4.10: Force/Displacement results from joints a) J1, b) J2, c) J3, d) J4, e) J5, f) J6, g) J7, h) J8, i) J9, j) J10, k) J11, l) J12, m) J13, n) J14, o) J15.

Lastly, in every joint, there is an effective joint area and an apparent joint area. The first is the area in which mechanical bonding did happen and, as such is a smaller but stronger joint section. The latter is a section that appears to be thoroughly bonded but where there is only adhesion between the materials. Because of this, it represents a larger but less bonded joint section. Because of this, the ”steps”, referred to above, can be a representation of the detachment of the area which is solely joined through adhesive forces and, after them, the curve represents the failure of the mechanically interlocked area.

Li *et al.* [86] created overlapped FSW joints between 7075 aluminum alloy and short glass fiber-reinforced poly-ether-ether-ketone (SGF/PEEK) and found 2 main failure mechanisms, i) tensile fracture starting at the lap interface and growing to the joint's surfaces, due to the mixture of polymer and metal in the SZ, and ii) shear fracture due to the large residual stress at the interface of the materials. Correia *et al.* [73] encountered three different failure mechanisms: Mode A, where the fracture occurred in the polymer (tensile fracture), Mode B, where failure came in the form of peeling at the interface (shear fracture) and Mode C, characterized by a combination of both modes A and B. A diagram of these failure mechanisms is presented in Figure 4.11. In that same study, Correia *et al.* concluded that the joints with the highest tensile strength failed in accordance with Mode A. Looking at Figure 4.12, where all fractured specimens' cross sections are presented, it is obvious that all 75 specimens from J1 to J15 fractured in accordance to Mode A.

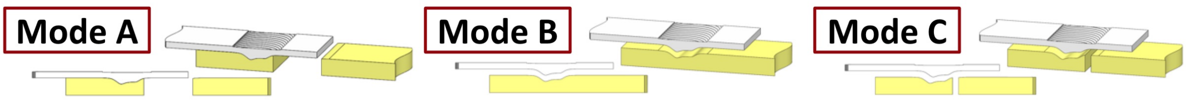

Figure 4.11: Schematic of the possible failure mechanisms, adapted from [73, 81].

Figure 4.12 also portrays an important finding regarding the aluminum. All specimens show a gap between the polymer, which is still attached to the joint, and the aluminum. This gap is a result of the plastic deformation present in the aluminum, bending it slightly next to the weld line.

To accurately compare these results with previous studies, there must be a common denominator. In this case, that is the joint's efficiency. The joint's efficiency is the ratio between the ultimate tensile strength of the joint (UTS) divided by the ultimate tensile strength of the weakest base material, as seen in Equation 4.1. In this study, the weakest base material is NORYL^{TM}, with a UTS of 80 MPa.

$$Efficiency(\%) = \frac{UTS_{joint}}{UTS_{WBM}} * 100 \tag{4.1}$$

Figure 4.12: Cross section of specimens 2, 3, 5, 6, and 7 from joints a) J1, b) J2, c) J3, d) J4, e) J5, f) J6, g) J7, h) J8, i) J9, j) J10, k) J11, l) J12, m) J13, n) J14, o) J15.

To understand the overall nature of the failure of the stress at the joint, there must first be a careful observation of the geometry of the specimens. Figure 4.13 shows a schematic of the cross section of the tensile test specimens. The first observation regards the varying materials' thickness at the joint section. Depending on the exact location for the crack to initiate, the actual fracture area varies from the nominal thickness of the base material. Second, given the overlapping nature of the joints, the stress field developed is quite complex, even though the specimens were loaded in a single direction. As schematized in Figure 4.13, the misalignment between the two materials' neutral lines induces a secondary bending moment. This representation was adapted from the Neutral Lines Model described by Schijve *et al.* [87], Ekh *et al.* [88], and Skorupa *et al.* [89]. The presence of a secondary bending moment causes forces to manifest in various directions. To estimate the stress level, two methods were found in the literature.

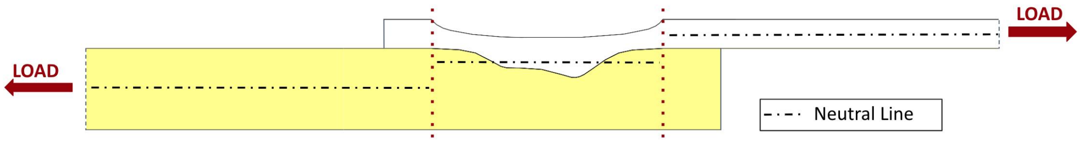

Figure 4.13: Schematic of the neutral lines across the cross section of the joint under tensile load.

Method 1 - Remote Stress

According to Infante *et al.* [47], one way to calculate the stress at the joint is by calculating the stress at the remote area, the remote stress. In this case, as depicted in Figure 4.14, the remote area is the area of a section of the weakest material, distant from the fracture section, through which the force is transmitted. The local area varies between joints. This simplification removes that variable and allows the stress to be calculated. The remote stress is equal to the ultimate tensile load (UTL) divided by the area of the remote section of the weakest base material, in this case, NORYL^{TM}, as Equation 4.2 demonstrates. This method was used in previous studies on this matter [10, 80, 81].

$$\sigma_{Remote} = \frac{UTL}{A_{Remote_{WBM}}} \tag{4.2}$$

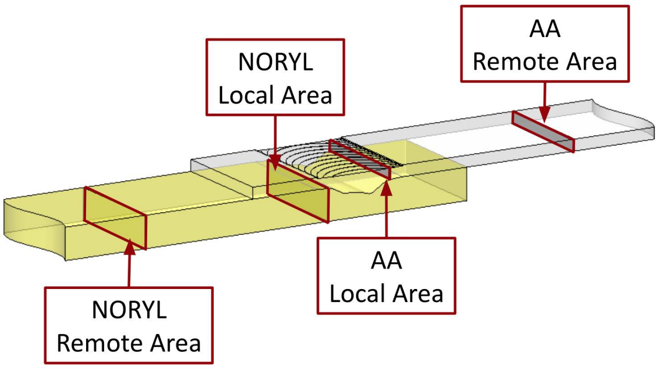

Figure 4.14: Schematic of the local and remote areas of both materials.

Using Equation 4.2 and the average UTL results measured during the tensile testing, the average remote stress was calculated, for each joint, and the results are presented in Table 4.4. Furthermore, using Equation 4.1 the joint efficiency, according to Method 1 was calculated.

The efficiency of the joints, J1 to J15, display an improvement from the results attained by Francisco [80], the previous study under similar processing parameters. The low efficiencies portrayed by the joints, under method 1, are representative of the strength of the joints, but they are tainted by the degree of simplifications used by the method. To understand the influence of these simplifications, method 2 was studied and implemented.

Table 4.4: Average joint strength, calculated through the Remote Stress method.

	Avg. UTL [N]	σ_{Remote} [MPa]	Efficiency [%]
J1	2294.83	18.36	22.95
J2	1698.20	13.59	16.99
J3	2168.76	17.35	21.69
J4	3414.17	27.31	34.14
J5	1789.58	14.32	17.90
J6	2323.65	18.59	23.24
J7	1708.08	13.66	17.08
J8	1845.15	14.76	18.45
J9	2409.97	19.28	24.10
J10	2734.03	21.87	27.34
J11	2922.36	23.38	29.23
J12	2423.19	19.39	24.24
J13	2742.35	21.94	27.43
J14	2230.70	17.85	22.31
J15	2350.00	18.80	23.50

Method 2 - Tensile Stress + Secondary Bending Moment's Induced Stress

Correia *et al.* [73] proposed a less simplified and, as such, more accurate way of calculating the stress. Considering failure mechanism mode A, introduced above, the crack, which initiates between the joint area and the NORYL^{TM} plate, due to its low stiffness, serves as an elastic pivot point. Due to the overlapping nature of the joint and the dissimilar thickness of the base materials, the misalignment of the neutral lines, which can be seen in Figure 4.13, induces a secondary bending moment. Both the overlapping nature of the joint and the thickness dissimilarity can be denominated as geometric eccentricities, and promote a secondary bending moment when an element is under tension [87, 88]. This moment is often overlooked in the literature regarding overlapping FSW joints, but as it will be apparent, its impact can not be negligible due to its significance.

As such, this method indicates that both the stress generated by the axial load and the stress induced by the secondary bending moment must be taken into account when calculating the ultimate tensile strength of the joints. Equation 4.3 shows that through this method, the local stress is equal to the tensile stress (or remote stress, in the previous method) plus the stress induced by the secondary bending moment, which is equal to the secondary bending moment multiplied by the distance, or half the thickness of the NORYL^{TM} plate, and divided by the moment of inertia of the NORYL^{TM} plate.

$$\sigma_{Local} \approx \sigma_T + \sigma_{SBM} = \frac{UTL}{A_{Remote_{WBM}}} + \frac{M_{SB} \cdot y}{I_{zz}} \tag{4.3}$$

The secondary bending moment was not measured but rather gathered through a simple finite elements model (FEM), developed using the commercial finite elements software Abaqus®. The development of this model does not fall under the scope of this thesis, and as such, it will only be introduced through a user's point of view. The 1D model was constructed using standard planar beam elements (B21), with 3.5 mm, to perform a non-linear elasto-plastic analysis.

Looking at Figure 4.15 a), it is visible that the schematic for the geometry of the joint used only has 2 segments. Contrary to the initial neutral line diagram, presented in Figure 4.13, which had three segments, for this simplification only two segments were considered. To do so, the overlap of the aluminum and NORYL^{TM} neutral lines served as the representation of the joint section. This region was not considered to be a segment itself because the scope of this analysis does not entail the study of the geometric and inertial properties of this region, which are unknown.

The top beam, Figure 4.15 b), which represents the aluminum plate, is clamped on its outer edge, whereas the bottom beam, which represents the NORYL^{TM} plate, is bounded by a guided clamp, allowing the load to be exercised in its direction. Finally, the jointed area was simplified through a linear overlap of the beams with a 12 mm length. This was measured to be the average linear distance between where the joint begins and ends, but in reality, this distance is larger, as the joint has a nonlinear geometry, portrayed through the cross section in Figure 4.7.

a)

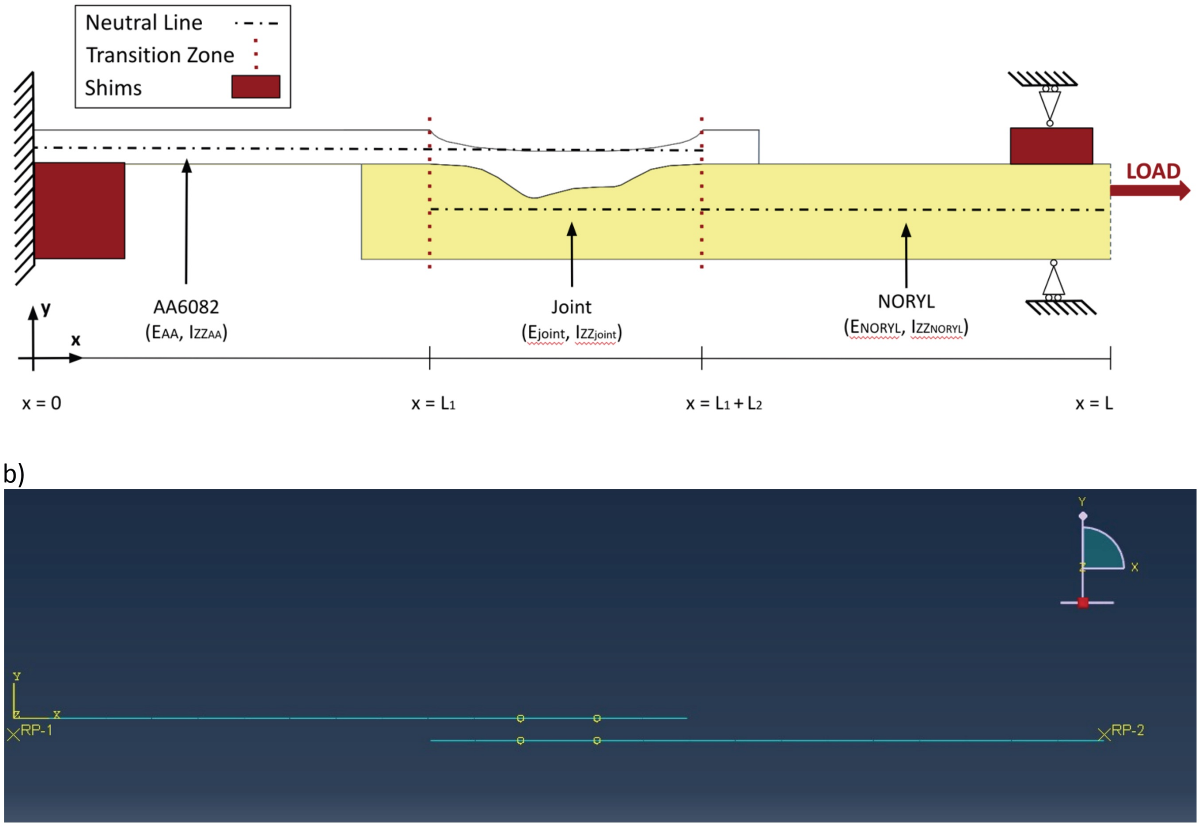

Figure 4.15: a) Schematic of the neutral lines, with the associated boundary conditions, b) Abaqus® 1D simplification of the model.

As stated before, the beams were introduced to represent each material plate, and as such, they were defined through their properties. To add to the mechanical properties presented in Section 3.1, the elasto-plastic data was incorporated. The NORYL^{TM}'s data was found in the manufacturer's data sheet [90]. The aluminum's thermoviscoplastic properties were defined using the Johnson-Cook constitutive model [91], following the application done by Rodriguez-Millan *et al.* [92, 93], for AA6082-T6. This model considers a linear elastic behavior until the yield point, as presented in Equation 4.4. In this equation the first term represents the strain hardening due to plastic deformation, the second defines the strain rate sensitivity, and the third one accounts for the thermal softening of the material. Using the model's equation and applying it to the aluminum, Rodriguez-Millan *et al.* defined the material properties, which were used in the numerical model. Their values and meaning can be found in Table 4.5.

$$\sigma = (A + B \times \epsilon^n) \times \left[1 + C \times \ln \frac{\dot{\epsilon}}{\dot{\epsilon}_0}\right] \times \left[1 - \left(\frac{T - T_0}{T_m - T_0}\right)^m\right] \tag{4.4}$$

Table 4.5: Johnson-Cook parameters for AA6082-T6 [92, 93], used in the numerical model

Parameters		**AA6082-T6**
Reference Yield Stress	**A [MPa]**	201.55
Material Constant	**B [MPa]**	250.87
Material Constant	**n**	0.206
Strain Rate Sensitivity Parameter	**C**	0.00977
Reference Strain Rate	$\dot{\epsilon}_0$ **[s^{-1}]**	0.001
Reference Temperature	**T_0 [K]**	293
Melting Temperature	**T_m [K]**	855
Thermal Sensitivity Parameter	**m**	1.31

Figure 4.16 presents a diagram of the tensile and bending moment stress expected to develop, according to this method, as well as an approximate location of the nucleation of a crack at the interface of the materials. The failure Mode A, experienced by the specimens, as well as the location of nucleation and propagation of the crack, were reflected in the numerical model and its elements, leading to material failure.

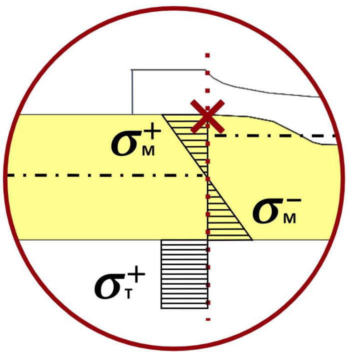

Figure 4.16: Diagram of the tensile stress (σ_T) and bending moment stress (σ_M) at the fracture location. Crack initially appeared at the X, adapted from [73].

Using the numerical model, the secondary bending moment for each of the fifteen joints was attained. An example of the full output for the numerical model can be seen in Figure 4.17, a plot of the development of the secondary bending moment along the length of the specimen. This graphic portrays the secondary bending moment for both beams, representative of the aluminum (blue) and the NORYL™ (red) plates, and their overlap at the joint region. The initial section of the NORYL™'s M_{SB} and the final section of the aluminum's M_{SB} plot lines are zero because they represent the free portion of overlapped material that is not connected. As expected, the M_{SB} is largest for the NORYL™ plate just next to the joint region, this is the location for the crack nucleation also seen in Figure 4.16. Contrarily to the NORYL™ the maximum M_{SB} in the aluminum's plot, just before the joint area, is not vertical to the M_{SB} at the beginning of the joint. This less abrupt reduction can be correlated with the presence of plastic strain in this section. As the aluminum starts to present plastic deformation, which was recorded above in Figure 4.12, only part of the M_{SB} is transmitted to the joint area. Graphically it translates as a non-vertical reduction of the aluminum's M_{SB}.

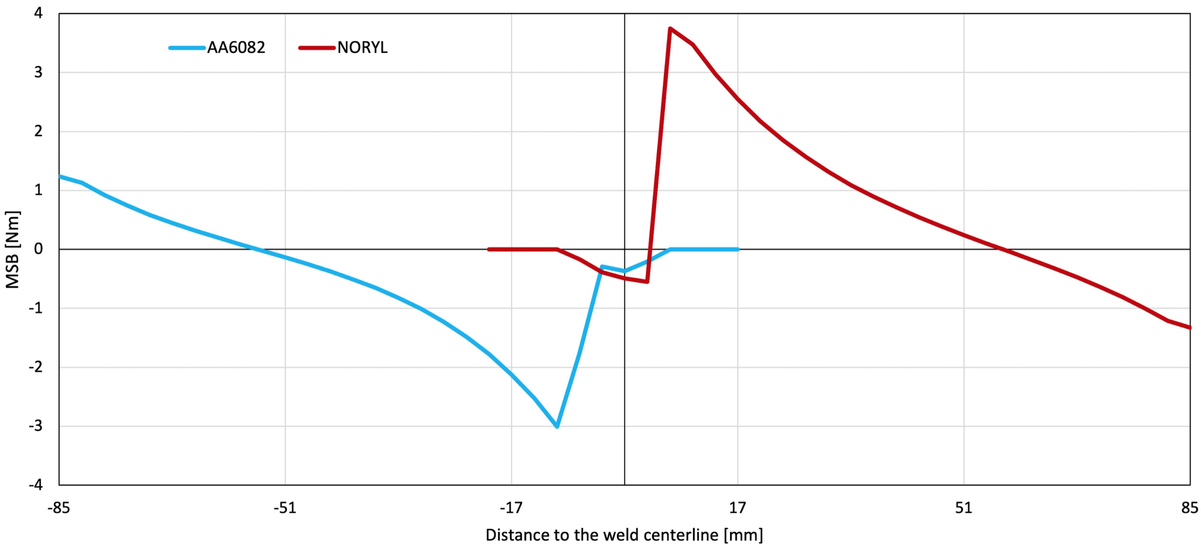

Figure 4.17: Development of the bending moment of J4 along its length, using the numerical model.

The bending factor can be defined as the ratio between the M_{SB} strength and the tensile strength, as displayed in Equation 4.5. Higher bending factors are associated with joints with lower UTL, due to the reduction in tensile strength, characteristic of a low-performance joint [87].

$$k_b = \frac{\sigma_{SBM}}{\sigma_T} \tag{4.5}$$

Table 4.6 gathers the results from the average UTL values previously introduced in Table 4.3, the secondary bending moment, as well as the results from Equations 4.3, 4.5, and 4.1 for the local stress according to Method 2, bending factor and joint efficiency, respectively.

Considering that the secondary bending moment derives from the applied load to the joint, its values are larger for joints with greater UTL (J4, J11, etc.) and smaller for lower-performing joints (J2, J7, etc.). The M_{SB} results range from 4.20 Nm to 2.47 Nm. Joints with higher M_{SB} will have larger secondary bending moment stresses and, because of that, higher overall local stresses. On average, the secondary bending moment stresses amount to 63% of the totality of the local stress.

Looking at the results, and comparing them to the results from Method 1, it's obvious that the highest-performing joints remain the same and the order, from best to worst-performing joint, is not impacted

Table 4.6: Average local strength, calculated through the Tensile Stress + Secondary Bending Moment's Induced Stress method.

	Avg. UTL [N]	M_{SB}[Nm]	σ_T [MPa]	σ_{SBM} [MPa]	σ_{Local} [MPa]	k_b	Eff. [%]
J1	2294.83	3.224	18.36	30.95	49.31	1.69	61.64
J2	1698.20	2.47	13.59	23.71	37.30	1.75	46.62
J3	2168.76	3.07	17.35	29.50	46.85	1.70	58.56
J4	3414.17	4.20	27.31	40.33	67.64	1.48	84.55
J5	1789.58	2.59	14.32	24.89	39.21	1.74	49.01
J6	2323.65	3.26	18.59	31.29	49.88	1.68	62.34
J7	1708.08	2.48	13.66	23.85	37.51	1.75	46.89
J8	1845.15	2.67	14.76	25.59	40.35	1.73	50.44
J9	2409.97	3.356	19.28	32.25	51.53	1.67	64.41
J10	2734.03	3.70	21.87	35.47	57.34	1.62	71.68
J11	2922.36	3.85	23.38	36.99	60.37	1.58	75.46
J12	2423.19	3.37	19.39	32.39	51.78	1.67	64.72
J13	2742.35	3.70	21.94	35.55	57.49	1.62	71.86
J14	2230.70	3.15	17.85	30.22	48.07	1.69	60.08
J15	2350.00	3.29	18.80	31.56	50.36	1.68	62.96

by including the stresses caused by the secondary bending moment. What does change using this method is the magnitude of the stresses developed during the tensile load, and this is easily spotted by comparing the joint efficiencies. For both methods, the joint efficiency is the ratio between the ultimate tensile strength of the joint (UTS) divided by the ultimate tensile strength of the weakest base material, as explained through Equation 4.1. Taking for example J4, through method 1 the efficiency of the joint was estimated to be 34.14%, and through method 2 was 84.55%. This realization can change the perspective an observer has on the performance of a joint. By the first method, one might think that the joint has much more to improve given the distance to 100%, or the strength of the weakest base material, giving the illusion of a poor-performing joint. But by the second method, the room for improvement is much smaller, which provides, in this case, a more realistic view of the joints produced.

Lastly, the bending factor results ranged from 1.48 to 1.75, with smaller bending factors being associated with larger UTL results due to the development of larger tensile stresses. Further studies should be conducted to attest to this observation and understand how and why this factor relates to and impacts the overall mechanical performance of the overlapping dissimilar joints.

4.4 Microstructure Analysis

In this section, the results from the microstructure analysis will be presented and discussed. The tests were performed following the methodology explained in Subsection 3.5.3 on three specimens with i) high joint efficiency (J4), ii) medium joint efficiency (J6), and iii) low joint efficiency (J7). Results will provide a more detailed insight into the microstructure of the FSW joints' cross section, to complement the previous analysis presented in Section 4.1. Furthermore, a chemical characterization of the materials interface will be presented.

Figure 4.18 shows the approximate location of the regions analysed for each joint. The samples from J4 and J6 were analysed in seven spots (A-G) whilst J7 had one additional test location (B1).

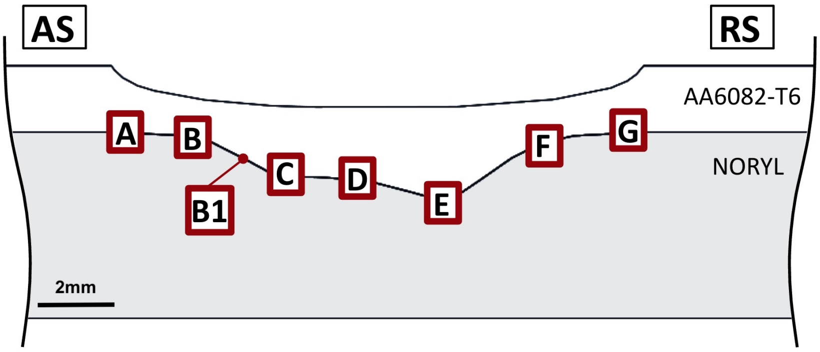

Figure 4.18: Schematic of the scanning electron microscopy test locations.

4.4.1 Scanning Electron Microscopy (SEM)

A detailed view of the samples' microstructure was attained using scanning electron microscopy, and the images from samples J4, J6, and J7 are portrayed in Figures 4.19 a), b), and c)respectively.

As previously observed in Section 4.1, all three cross-sections present a double concavity feature, at the interface. This geometrical characteristic improves the mechanical interlocking by increasing the bonded area without breaking the continuity of the materials, allowing for an improved bonding of the joint. Furthermore, the macro-image of all three specimens shows that they all exhibit a void defect outside the SZ. In reality, this defect is a small closed tunnel, as it is present along the length of the weld line, common in these joints [7, 94, 95]. As failure occurs outside of this area, nothing indicates that its presence is in any way correlated to a worsening of the mechanical performance of the joints.

The test locations A and G are approximately located at the end of the apparent joining area. This is the area that appears to be soundly connected when evaluated with the naked eye. A closer inspection of the microstructure shows that only J4 presents a tight connection at these locations, with no gaps between both base materials. Larger effective joining areas correlate to higher mechanical strength due to the increase in the loading bearing area. J4 is the joint with the highest mechanical strength, and from the three specimens under analysis, it is the one with the largest effective joining area. Following J4 is J6 with the intermediate mechanical performance. This joint's effective connection starts just after location B and ends just before location G. Finally, J7 comes last with the smallest joint area and the lowest mechanical strength of the three joints, only connected between B1 and between E and F. These gaps may stem from significant variations in the thermo-mechanical properties of the base materials, resulting in disparate heating and cooling rates and causing geometric mismatching at the interface, a phenomenon identified by Li *et al.* [86].

Recalling Figure 4.7 d), f), and g) where it was shown the cross section of joints J4, J6, and J7 after failure, respectively. In these images it is notorious a variance in the location of the nucleation of the fracture, with J4's location being the furthest from the center of the weld line and J7's being the closest. Crossing this observation with the length of the effective joining area, a pattern appears. Larger joining

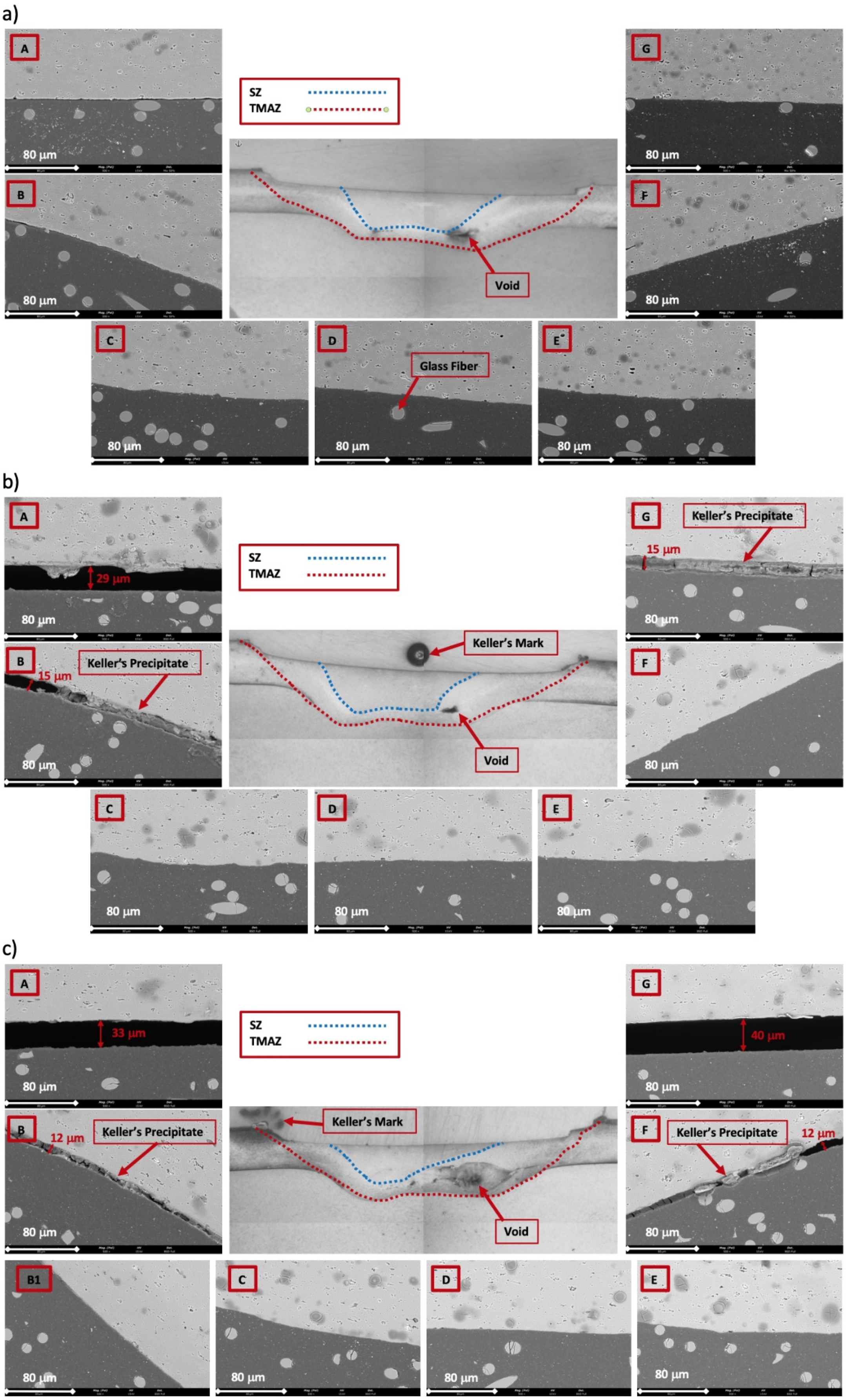

Figure 4.19: Cross section's macro and microstructures a) J4, b) J6, and c) J7.

areas promote an increase in the mechanical strength of the joint which could be connected with the increase in the distance of the failure sight from the center of the weld line.

Regarding the gaps between the aluminum and NORYL^{TM} materials, for J6, they were measured at 29 μm in location A and 15 μm in locations B and G, near the ends of the effective joining area. whereas J7 gaps measure 33 μm and 40 μm in locations A and G, respectively, and 12 μm in locations B and F. From Figures 4.19 b) and c) it is observable an accumulation of debris which was chemically analysed and concluded to be deposits of chlorine, fluorine, and sodium. Both chlorine and fluorine are in Keller's reagent composition and the sodium most likely came from non-distilled water used in the cleaning of the samples. Even though unwanted, the presence of these precipitate regions indicates the nearness to the beginning of the effective joining area, as the gaps became so small, that not even the ultrasonic cleaning couldn't clear them from the interface of the BM.

4.4.2 Energy Dispersive Spectroscopy (EDS)

Amongst the three specimens, thirty-eight EDS analysis were performed. The test locations are shown above in Figure 4.18. For almost every location, three spots were analysed, one on the aluminum, one at the interface, and the last in the NORYL^{TM} material. More complete EDS reports are available in Appendix C. The EDS analysis had two main objectives, i) chemically characterize the interface, and determine the presence of oxygen at the interface to validate the hypothesis presented by Derazkola *et al.* [6], and ii) identify the precipitate accumulated in some sections of the interface. Figure 4.20 shows the three spots tested in location D of the sample from joint J4 and the respective EDS elemental analysis spectrum.

Figure 4.20 a) and b), regards the analysis performed on the aluminum material. As expected, approximately 93.5% of its atomic concentration is aluminum, and the rest is oxygen and carbon. These last two atoms are most likely due to epoxy resin residue that was left on top or embedded in the sample, after polishing. Figure 4.20 c) and d), regards the analysis performed on the interface region of the joint. Here the atomic concentration is mostly comprised of carbon (71.2%), followed by aluminum (26.0%) and oxygen (2.1%). Depending on the exact spot tested, results may vary from having more carbon, as in this case, and more aluminum. Figure 4.20 e) and f), regards the analysis performed on the NORYL^{TM} material. As expected, approximately 87.7% of its atomic concentration is carbon, followed by oxygen at 10.1% and a small amount of silicon. All three atoms are present in the NORYL^{TM}'s composition, with silicon being one of the main constituents of fiberglass. Lastly, Figure 4.21 depicts the analysis performed on the precipitate deposit at the interface, in location G of the sample from joint J6. The atomic concentration indicates a large percentage of carbon (60.8%), followed by oxygen (13.0%), chlorine (10.8%), sodium (8.2%), and a small percentage of aluminum (3.9%). The presence of carbon, aluminum, and a small degree of oxygen, was expected given that this is at the interface, and comparing it to results from Figure 4.20 d). The presence of chlorine and sodium (and in other tests fluorine, reference to Annexes C) was unexpected but explicable due to the methodology followed. The reagent used to see the aluminum's grain was Keller's reagent, composed of HNO3, HCl, HF, and distilled water.

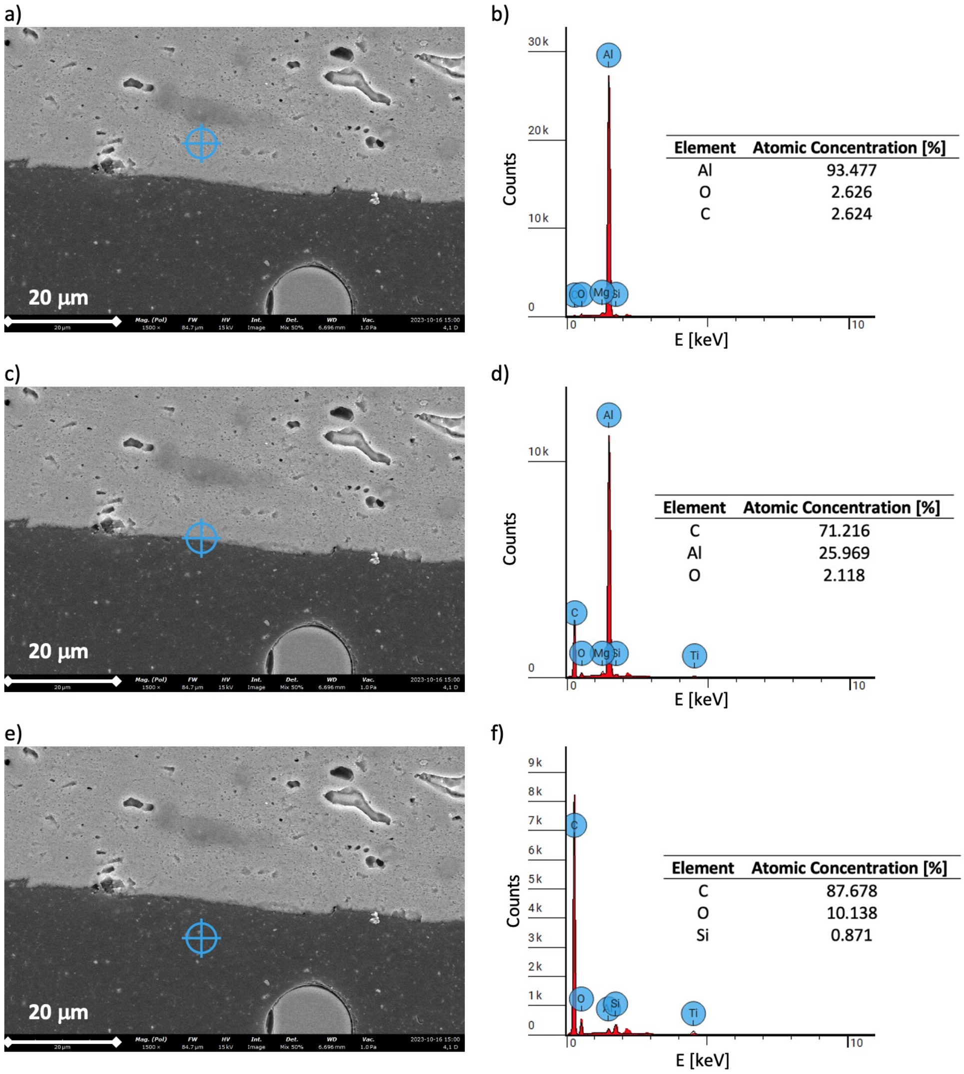

Figure 4.20: Energy dispersive spectroscopy of joint J4, in location D of Figure 4.18, a) aluminum's test spot, b) EDS spectrum of the aluminum, c) interface's test spot, d) EDS spectrum of the interface, a) NORYL^{TM}'s test spot, b) EDS spectrum of the NORYL^{TM}.

The debris found in some detached sections of the interface is Keller's precipitate (accounting for the chlorine and fluorine) mixed with undistilled water (accounting for the sodium), which settled in the small gaps and was not properly removed during the ultrasonic bath, at the end of the preparation of the samples. Although unwanted, it certainly did not impact the mechanical performance of the joints, as this was only done to these three samples, none of which were used in the mechanical tests. In future works, a more thorough cleaning of the samples should be done to mitigate this effect.

In reference to the hypothesis presented by Derazkola *et al.* [6], where oxygen was found in larger concentrations, allowing for the speculation that at the interface, molecules of aluminum oxide formed and aided in the bonding process, this was not what was observed here. The oxygen atomic concentration is lower at the interface than in the NORYL^{TM}, and approximately the same as the concentration in the aluminum. This indicates that the oxygen present at the interface is, most likely, either part of the NORYL^{TM} material or residue from the epoxy resin. If an oxide layer were to be formed at the interface, a larger concentration of oxygen was expected. It is expected that some degree of atomic interaction

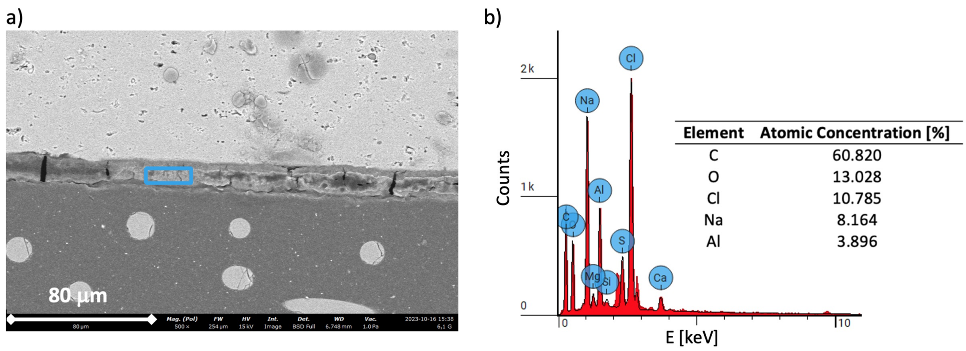

Figure 4.21: Energy dispersive spectroscopy of joint J6, in location G of Figure 4.18, a) Keller's precipitate test spot, b) EDS spectrum of the Keller's precipitate.

between the materials takes part in the bonding mechanism, either physical interactions or chemical bonding. From the analysis performed the oxide layer hypothesis was not proven, but it may still be true, and for that reason, a more detailed spectroscopy analysis focused on lightweight atoms. Other interactions, besides the aluminum oxide layer, could be studied, namely other ionic or covalent bonds, metallic or hydrogen bonds, amongst others [96, 97], to understand in more detail the nature of the bonding mechanisms.

4.5 Hardness Tests

Vickers hardness tests were performed on three specimens, the same as in Section 4.4, and the results are present in Figure 4.22 b), c) and d), respectively. The tests were carried out in a straight line, across the length of the specimen, in three different locations. The schematic of the test points can be seen in Figure 4.22 a). Path A passes solely through the aluminum layer and was measured at a distance of 1 to 1.5 mm from the top limit of the specimen. Path B passes both through the polymer and the aluminum materials and was measured at a distance of 2.7 to 2.8 mm from the top limit of the specimen. Finally, path C passes solely through the polymer layer and was measured at a distance of 2.75 mm from the bottom limit of the specimen. Measurements were made beginning 2 mm away from the left border of the specimen and 0.5 mm from each other. Unprocessed material, of both aluminum and NORYL™, was also tested to attain the nominal hardness values and serve as a baseline for this study.

At first glance, it is quite obvious that throughout the length of the specimen, the AA6082-T6 hardness is considerably smaller than the nominal value for the parent material, suggesting a variation in microstructure and grain size between the welded area and the unprocessed material, [74, 77]. Looking at path A, it is possible to make out a "W" shape, a feature found by several other authors [74, 77, 98]. This shape depicts a rapid hardness decrease when approaching the TMAZ followed by a slight increase when narrowing in on the SZ and finally, a small decrease when arriving at the nugget location. The minimum value was found in the transition between the TMAZ and the SZ with the nugget's hardness being slightly higher.

Recalling Section 4.2 Table 4.2, the average peak temperature in the proximal location of the thermocouples was above 200°C. According to Moreira *et al.* [77] the strengthening precipitate which attributed the T6 condition to the heat-treated aluminum, can only remain stable for temperatures lower than 200°C, meaning that the T6 condition is loss under this FSW processing representing a decrease in the joints' hardness. Given that the temperature at the nugget zone is likely to be higher than the recorded temperature, the slight hardness increase could be justified by a recrystallization of the finer grain [77].

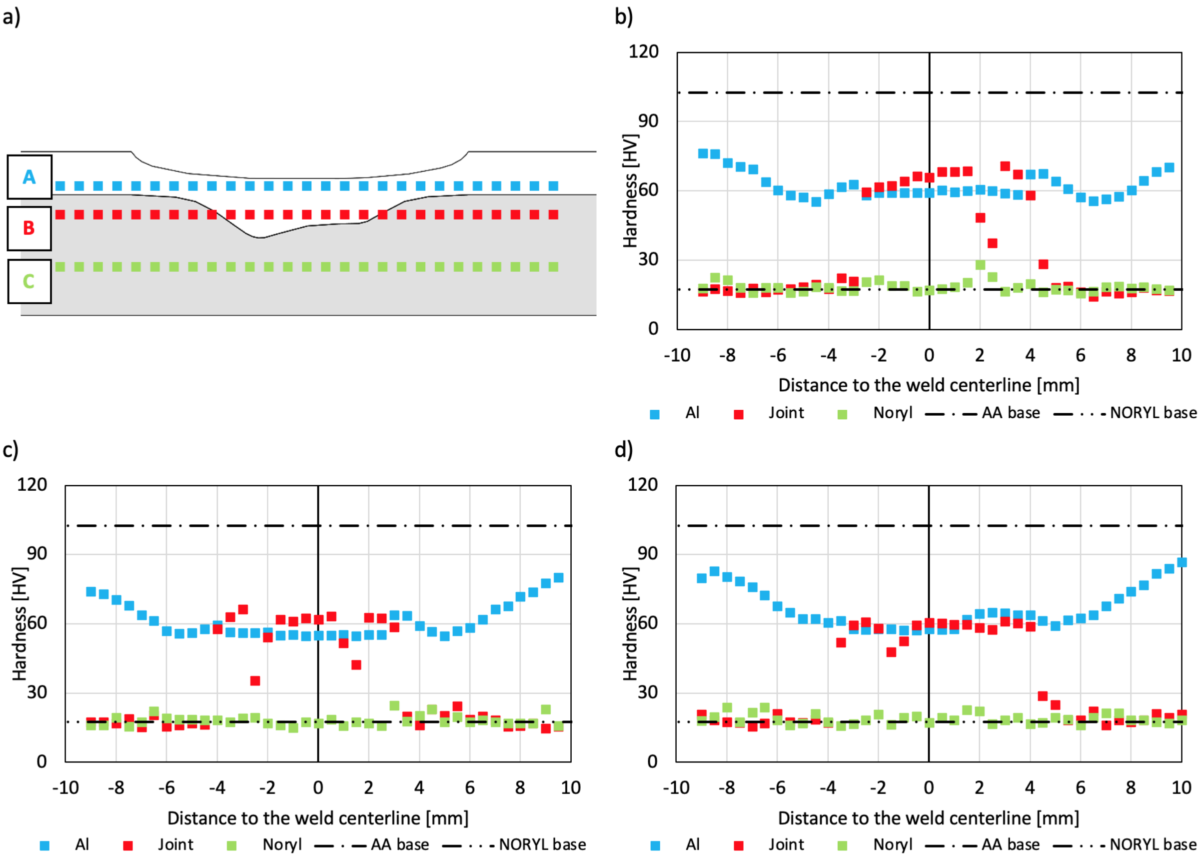

Figure 4.22: a)Schematic of the hardness test location, paths A (blue), B (red), and C(green), Hardness profiles for joints b) J4, c) J6, and d) J7.

The center measurements along path B were made in the aluminum section of the joint. Significant dips in the hardness profile were found coincident with the presence of void defects in the cross section, described in Subsection 2.2.6 and visible in Figure 4.5 a).

Analysing the hardness profiles of the polymer, in both paths C and B, it is noticeable that the values measured oscillate around the nominal value evaluated at 17.39 $\pm$ 0.2 HV. Average polymer hardness values for specimens 4, 6, and 7 were 18.42 $\pm$ 0.2 HV, 18.85 $\pm$ 0.2 HV and 18.85 $\pm$ 0.2 HV, respectively. A slight increase between the measured nominal harness value and the specimens' value is consistent with the location of the test. For the nominal value, the test was performed on the surface of the polymer, a location with fewer glass fibers, whilst the specimens were tested on the cross section of the material. In the specimens, oscillations in value are related to the increased presence or absence of short glass fibers, and increasing or decreasing hardness, respectively.

No relation could be made between the joint efficiency and the hardness profiles. Between the three joints, and along each path, differences were small and no pattern was found to sustain a possible conclusion on this matter. Also, unlike Costa *et al.* [98], no significant increase in hardness was found when increasing the welding speed, meaning that, for the small parameter interval studied, such a relation can't be attained.

However, this test could be of value if the objective was to define the various zones of the joint morphology found in the cross section, as described in Subsubsection 2.1.4. Analysing the variations of hardness along the aluminum allows for a characterization of the microstructure of the joint.

4.6 Statistical Analysis of the Effects of Processing Parameters

A statistical analysis was performed after all the results were attained and discussed. The main objective of this analysis was to understand the relationship between the processing parameters and the results gathered. To this end, both the temperature results, discussed in Section 4.2, and the mechanical strength results, presented in Section 4.3, were subjected to an ANOVA, using the Minitab Statistical Software. Particularly, when it comes to the mechanical strength results, the study was conducted to achieve the highest results possible, as in this case, high UTL results correlate to a higher quality of the joints produced.

The assessment of the terms' significance was done by evaluating the F-values and p-values, and terms with a p-value higher than the initial threshold of α = 0.1 were disregarded. This was done according to the Stepwise Backward Elimination method, an iterative process, where the least significant terms were removed, for each step, reaching a reduced model with only significant predictors [68, 99]. To assess the relevance of the model's individual terms, a 95% interval of confidence was selected, a value that provides a balance between being strict enough to reduce false positive results and not being overly strict which can lead to false negative results.

4.6.1 Processing Temperature Statistical Analysis

The processing temperature statistical analysis was performed using the average peak temperature recordings for each side. These results were presented earlier in Table 4.2. Tables 4.7 and 4.8 present the analysis of variance and the model summary for the average RS temperature and AS temperature, respectively. The ANOVA study for the processing temperatures had two main objectives to achieve, i) finding and understanding if a correlation between process parameters and thermal behaviour exists, and ii) discovering if there is an optimized temperature for the current study.

Although an ANOVA was conducted for both AS and RS, the analysis of the results will fall mostly on the AS. This decision takes into consideration that the temperatures recorded were an approximation of the real temperatures developed during the process, and its acquisition becomes extremely difficult given the geometry of the joint and the passing of the tool, during the process. Given the nature of the temperature generation, due to the friction between the tool and the BM and the plastic deformation of the materials during the process, the RS temperature is a by-product of the AS temperature, and not the other way around. As such, studying the AS average temperature will produce conclusions that are closer to the reality of the process.

Table 4.7: Average retreating side (RS) temperature analysis of variance — ANOVA

Source	DF	SS	MS	F-value	p-value	Contribution
v	1	130.9	130.9	0.30	0.597	1.3%
Tilt	1	3782.2	3782.7	8.56	0.014	36.8%
v·Tilt	1	1496.1	1496.1	3.38	0.093	14.6%
Error	11	4862.2	442.0			47.3%
Total	14	10271.3				
R^2 = 52.7%, adjusted R^2 = 39.8%						

The ANOVA results for the average RS temperature found the welding speed to be a non-significant term, as its p-value is above α=0.1. Within this interval, the independent variable tilt and the two-way interaction between the tilt angle and the welding speed are statistically significant. However, considering the confidence interval was 95%, the only significant term would be the tilt angle, amounting to a contribution of 36.8%. Once again, looking at the fitness of the model, the percentage of variation in the response that is explained by the model (R^2) was 52.7%, whilst the same concept adjusted for the number of predictors relative to the number of observations (adjusted R^2) was of 39.8%. Equation 4.6 subsequently offers the numerical expression connecting the average temperature on the RS and the processing parameters.

$$T_{RS} = 680 - 3.26 \cdot v - 197.4 \cdot Tilt + 1.368 \cdot v \cdot Tilt \tag{4.6}$$

Table 4.8: Average advancing side (AS) temperature analysis of variance — ANOVA

Source	DF	SS	MS	F-value	p-value	Contribution
ω	1	1491.0	1491.0	9.33	0.010	34.8%
Tilt	1	875.8	875.8	5.48	0.037	20.4%
Error	12	1917.7	159.8			44.6%
Total	14	4284.6				
R^2 = 55.2%, adjusted R^2 = 47.8%, predicted R^2 = 26.6%						

The ANOVA results for the average AS temperature found two significant independent variables, the rotational speed, and the tilt angle, with the rotational speed exhibiting the largest contribution (34.8%), followed by the tilt angle (20.4%). In terms of the fitness of the model, the percentage of variation in the response that is explained by the model (R^2) was only 55.2%, whilst the same concept adjusted for the number of predictors relative to the number of observations (adjusted R^2) was of 47.8%. The predicted value (predicted R^2) only amounted to 26.6%, which could indicate an over-fit model. This happens when terms that lack significance in the broader population are added, making the model overly customized to the sample data and skewing the predictions [100]. Subsequently, Equation 4.7 provides the numerical expression linking the average temperature on the AS and the processing parameters.

$$T_{AS} = 239.6 + 0.0522 \cdot \omega - 16.02 \cdot Tilt \tag{4.7}$$

Looking at Figure 4.23 a), where the main effects on the average temperature are displayed, it's noticeable how the rotational speed exhibits the largest contribution of the three parameters, with its increase resulting in higher AS temperatures. Contrarily, the tool tilt angle presents a negative relationship, meaning the smaller it is, the higher the temperature. All this is true within the scope of the

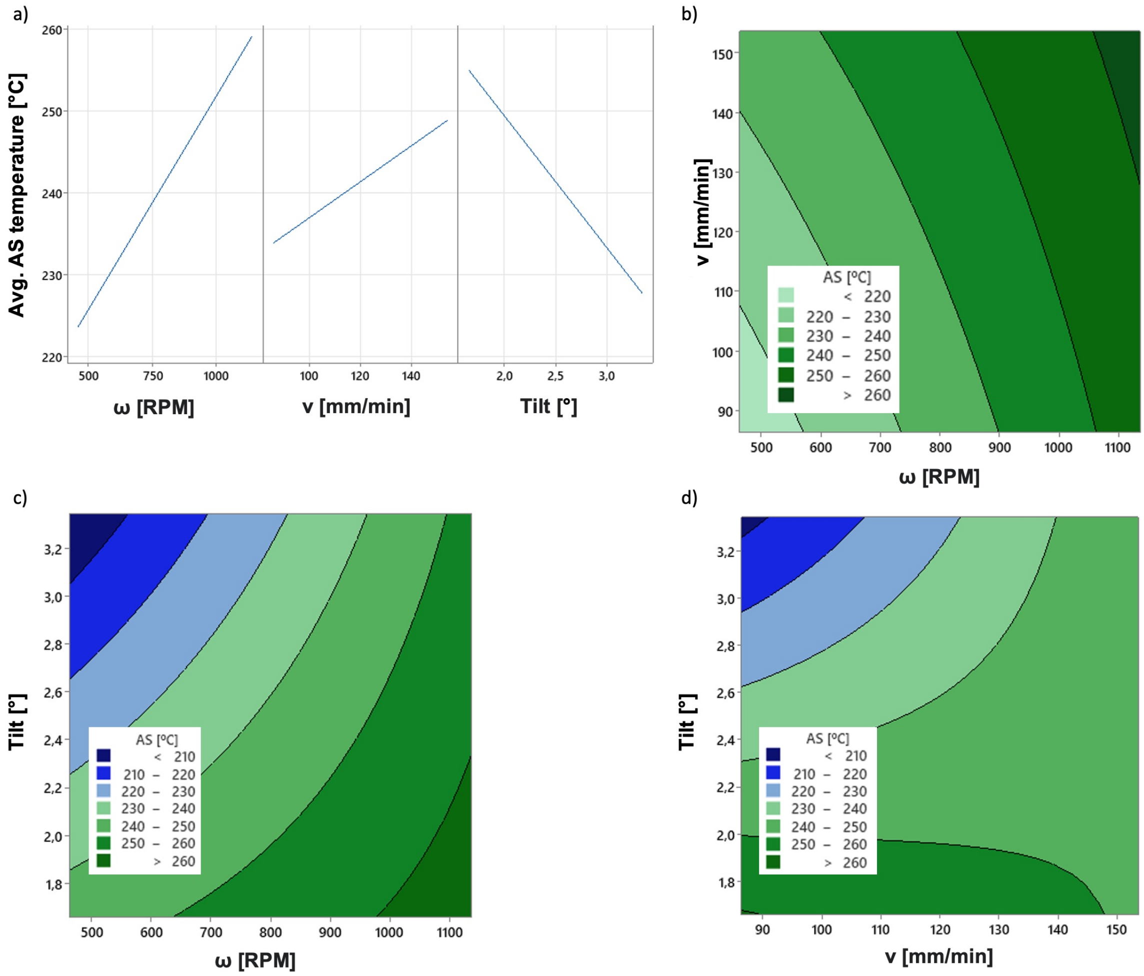

Figure 4.23: a) Main effects of the joining parameters on average AS temperature; Contour plots of average AS temperature as a function of interactions between b) rotational speed and welding speed, keeping a 2.5° tilt angle, c) tilt angle and rotational speed, keeping 120 mm/min of welding speed, and d) welding speed and tilt angle, keeping 800 rpm of rotational speed.

analysis. Regarding now the contour plots presented in Figure 4.23 b), c), and d) it is possible to see a saddle-like response surface contour as the welding speed increases in relation to the tilt angle. For higher welding speeds, the variance in said region is smaller which can be interpreted as a smaller variation in the output with the variation of the process parameters. Higher AS temperatures are present in this region, contrary to lower temperatures which can be seen in blue, on the graphics, in the corner of the plots where characterized by larger tilt angles. Overall, and as explained in previous sections, higher temperatures are usually indicative of better-performing joints, and these plots point to a combination of high welding and rotational speeds, and smaller tilt angles to achieve said results.

4.6.2 Quasi-Static Tensile Results Statistical Analysis

The quasi-static tensile results statistical analysis was performed using the same UTL results as the ones presented in Table 4.3. Table 4.9 presents the analysis of variance and the model summary for the quasi-static tensile test results. The ANOVA study for the UTL had two main objectives to achieve, i) finding and understanding the correlations between process parameters and mechanical strength, ii) discovering the optimized set of parameters that, mathematically, maximized the joint strength results.

Table 4.9: Quasi-static tensile test results variance analysis — ANOVA

Source	DF	SS	MS	F-value	p-value	Contribution
ω	1	726334	726334	5.42	0.025	7.1%
v	1	27165	27165	0.20	0.655	0.3%
Tilt	1	1629327	1629327	12.15	0.001	15.9%
ω·**v**	1	834313	834313	6.22	0,017	8.1%
v·Tilt	1	1809115	1809115	13.50	0.001	17.6%
Error	39	5228118	134054			51.0%
Total	44	10254372				
R^2 = 49.0%, adjusted R^2 = 42.5%, predicted R^2 = 29.0%						

The ANOVA results for the quasi-static tensile test results found the welding speed to be a non-significant term, with a p-value of 0.655. It also found two significant independent variables, the rotational speed, and the tilt angle, with the tilt angle exhibiting the largest contribution between the two (15.9%), as well as two two-way interaction terms, the first between the rotational and welding speeds and the second between the welding speed and the tilt angle, amounting for the largest contribution (17.6%). In terms of the fitness of the model, the percentage of variation in the response that is explained by the model (R^2) was only 49.0%, whilst the same concept adjusted for the number of predictors relative to the number of observations (adjusted R^2) was of 42.5%. The predicted value (predicted R^2) only amounted to 29.0%, which could indicate an over-fit model [100].

$$UTL = -1120 - 4.93 \cdot \omega + 32.6 \cdot v + 2896 \cdot Tilt + 0.0466 \cdot \omega \cdot v - 27.46 \cdot v \cdot Tilt \tag{4.8}$$

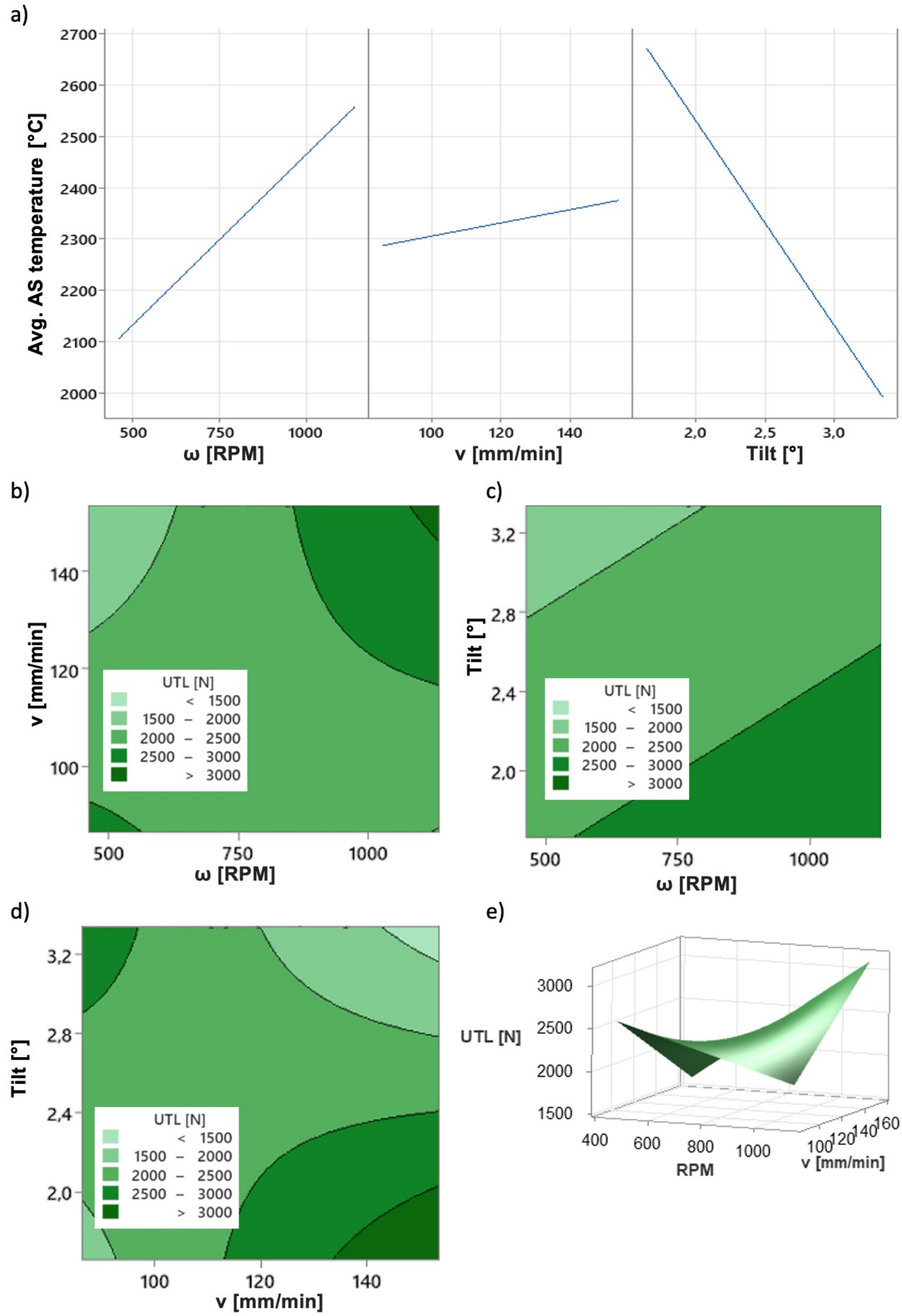

Figure 4.24: a) Main effects of the joining parameters on UTL; Contour plots of UTL as a function of interactions between b) rotational speed and welding speed, keeping a 2.5° tilt angle, c) rotational speed and tilt angle, keeping 120 mm/min of welding speed, d) welding speed and tilt angle, keeping 800 rpm of rotational speed; and e) Response surface of UTL vs welding speed vs rotational speed, keeping a 2.5° tilt angle.

Looking at Figure 4.24 a), where the main effects on the UTL are displayed, it is obvious how the tilt angle is the parameter with the largest contribution. In this relation, decreasing the tilt angle promotes an expected increase in the UTL of the joint, for the range of values understudy. On the other hand, increasing the rotational speed promotes an increase in the joint strength. Lastly, increasing the welding speed promotes a small increase in the UTL when compared to the other two parameters. Regarding the contour plots presented in Figure 4.24 b), c), and d) it is observable the narrowing of a saddle-like response surface contour as the welding speed increases in relation to the tilt angle. For lower welding speeds, the variance in said region is smaller which can be interpreted as a smaller variation in the output with the variation of the process parameters.Higher UTL values are graphically represented in a darker green color and are present in the corners of the domain, locations where smaller variations in the process parameters produce larger increases in the UTL output. Combining the information from the various plots, it appears that the optimum regions combine higher values of welding and rotational speed, with lower values of tilt angle. This comes in agreement with what was observed experimentally, with J4 being the highest-performing joint with parameters that corroborate this observation. Looking at Figure 4.24 e), the response surface portrays a saddle shape with a narrower curvature for higher UTL values. This may predict an increase in volatility of the output, the closer the parameters get to the optimum values. In other words, the closer the parameters are to their optimum value, the less stable the UTL output, which could result in a worse overall mechanical performance than the one expected and statistically predicted. To finalize this statistical analysis, the ANOVA for the UTL results generated an optimized response to maximize the strength of the joint, based on the three FSW parameters.

4.7 Optimization

The ANOVA for the UTL results generated an optimized response to maximize the strength of the joint. This solution has a rotational speed of 1136 rpm, a welding speed of 154 mm/min, and a tilt angle of 1.7° . From Equation 4.8, for this solution, the estimated mean response was 4238 N, whilst the 95% lower confidence interval and the 95% lower prediction interval were 3654 N and 3389 N, respectively.

Similarly to the fifteen previous joints, the optimized joints were produced following the methodology presented in Section 3.4. In total, six joints were produced in this second stage, three joints were produced using the optimized set of parameters (ω=1136rpm, v=154mm/min and tilt=1.7°) and three were produced with the parameters of J4, the best joint so far (ω=1000rpm, v=140mm/min and tilt=2°). Figure 4.25 shows the weld lines of the three joints with the optimized set of parameters (OPT1, OPT2, OPT3), as well as, the weld lines of the three repetitions of J4 (J4_1, J4_2, J4_3). From this point onward, as a group, the six joints will be denominated as ”optimization joints”, the three joints with the optimized set of parameters will be named ”optimal joints”, and the three joints with the parameters from J4 will be called ”repetition joints”.

The reasoning behind the decision to produce the repetition joints lies in the fact that the temperature, at the location of the FSW machine, couldn’t be controlled. The first fifteen joints were produced in July, where the ambient temperature average at 23.7° C in the mornings and 24.9° C during the afternoons. In contrast, the optimization joints were produced in late November, where temperatures were around

10° C in the mornings and only 18° C during the afternoons.

Figure 4.25: Weld line of the optimization FSW joints, a) OPT1, b) OPT2, c) OPT3, d) J4_1, e) J4_2, f) J4_3.

4.7.1 Surface quality - optimization joints

Following the same order as the analysis in Section 4.1, the first observation was done as soon as the plates were removed from the clamping system, confirming that the joints were successfully bonded through a tight connection between the base materials. Similarly to J4, shown in Figure 4.2 c) and d), no NORYL™ overflow was detected in either one of the six joints produced.

Looking at Figure 4.26, it can be seen, in greater detail, the disruption of the weld line in the initial position. J4 was one of the joints with an intermediate degree of this defect, and although present, there was only a small defect that compromised the aluminum material, with no polymer extrusion. On the contrary, all six optimization joints present a significant degree of this defect. The repetition joints (J4_1, J4_2, J4_3) have a more evident initial defect than the optimal joints, but even these, have a larger defect than the worst joint in the first production, J10. As concluded in Section 4.1, the combination of a larger than necessary dwell time with higher rotational speed promotes the emergence of this defect. But if these were the only intervening factors, the repetition joints would have a similar appearance to J4, and that is not the case. What can be deduced from this observation is that the ambient temperature, which was the only uncontrolled parameter that significantly diverged between both production times, must have an impact on the formation of this initial defect.

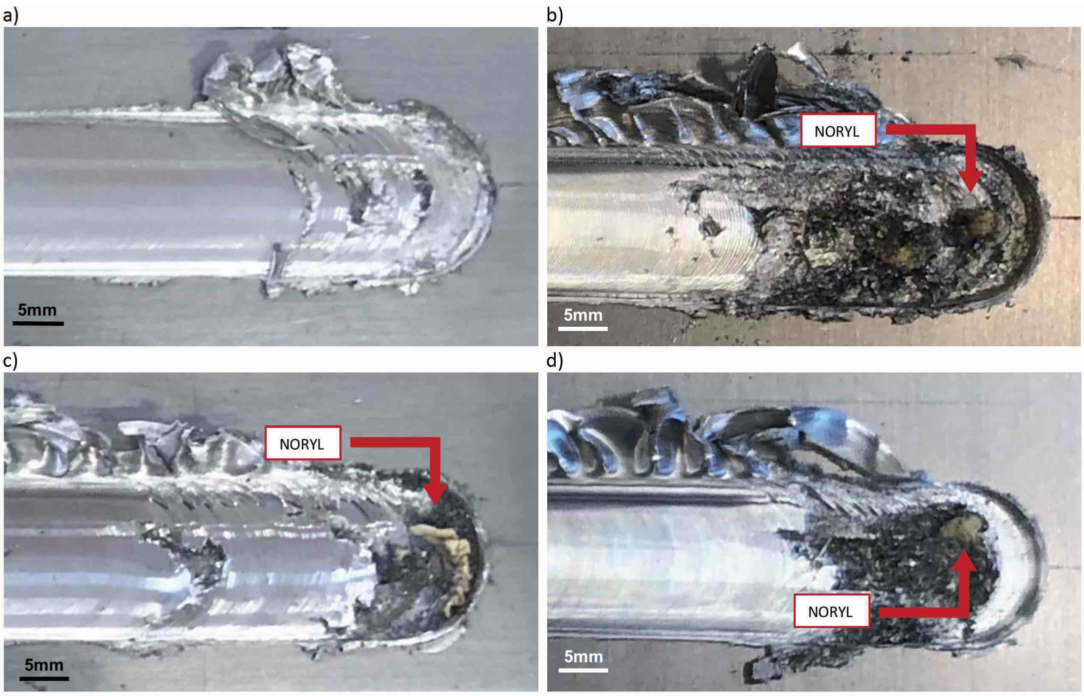

Figure 4.26: Initial defect for joints, a) J4, b) J4_3, c) J10, d) OPT1.

In comparison to the first fifteen joints, and as expected, the average smoothness of the weld line increased. As evidenced previously, increasing the rotational speed promotes an increase in the surface quality of the weld line. Overall, there is a slight difference between the repetition joints and the optimal ones, with the optimal joints (OPT1, OPT2, OPT3) having a smoother and shinier finish to their weld line. In regards to the exit hole defect, no significant differences are noted, as the pin length and the plunge depth were kept the same.

Lastly, the flash defect was the most prominent variation in the overall surface quality of the joints. Comparing the repetition joints in Figure 4.25 d), e) and f) with J4 in Figure 4.1 d), it is very apparent that the flash defect is much more pronounced in the repetition joints when it was mostly negligible in J4. A closer observation shows that J4_3 has significantly less flash than J4_1 or J4_2. This can be explained by the time of day during which the joints were produced. The first two repetition joints were produced in the morning whilst the third was produced in the afternoon. The difference in ambient temperature was so significant that the rapid cooling of the plasticized aluminum accumulated on the RS of the weld line. In an attempt to mitigate this effect, all optimal joints were produced during the afternoon, in the order that they are presented. OPT1 joint presents a similar amount of flash to J13, reference to Figure4.1m), whilst OPT2 and OPT3 present a similar flash defect to J10, Figure 4.1 j). This was in line with what was expected as the optimized parameters combine the rotational speed of J10 with the tilt angle of J13, both important factors for this case.

Overall, the surface quality of this second production instance decreased compared to the first instance, particularly in the repetition joints, indicating that the ambient condition significantly affects this matter.

4.7.2 Quasi-Static Tensile Results - optimization joints

The optimization joints were cut into 25mm specimens, similar to the other fifteen plates. Two specimens, from the center of each joint, were used for the quasi-static tensile shear testing. The Force/Displacement results, for all the twelve specimens tested, can be seen in Table 4.10 and in Figure 4.27.

Table 4.10: Quasi-static tensile tests results for the optimization joints [N].

	UTL1	UTL2	Avg. UTL	St.Dev.	Total Avg. UTL	Total St.Dev.
OPT1	2894.14	2933.15	2913.64	19.51		
OPT2	2507.48	2681.37	2594.42	86.95	2645.24	232.14
OPT3	2200.49	2654.79	2427.64	227.15		
J4_1	2936.76	2952.10	2944.43	7.67		
J4_2	2435.79	2571.63	2503.71	67.92	2789.49	207.90
J4_3	2845.17	2995.48	2920.32	75.15		

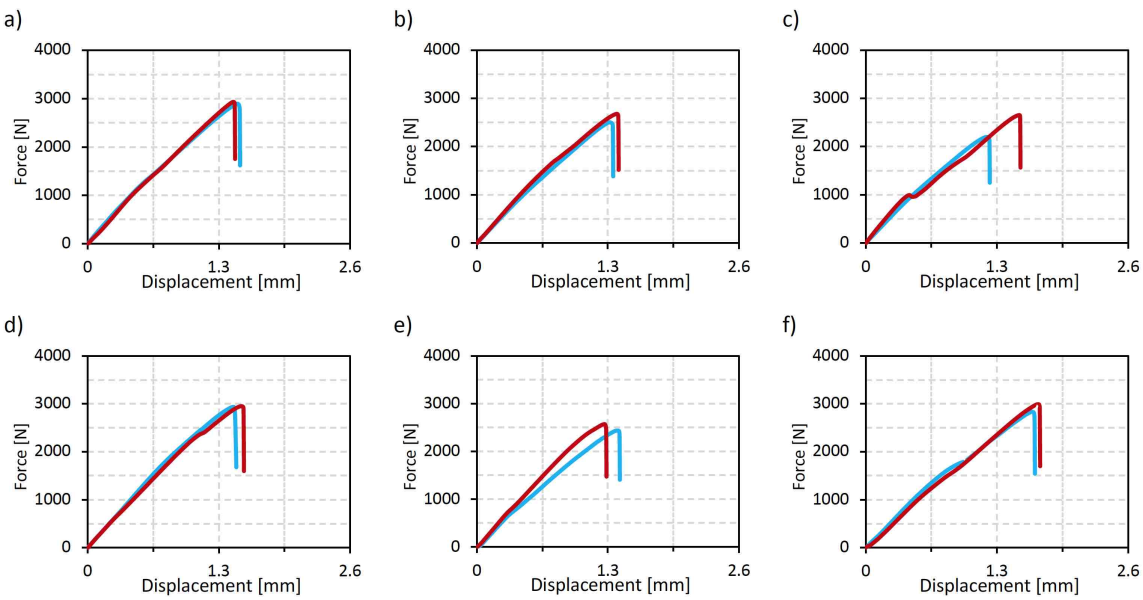

Figure 4.27: Force/Displacement results from the optimization FSW joints, a) OPT1, b) OPT2, c) OPT3, d) J4_1, e) J4_2, f) J4_3.

From the results of the repetition joints (J4_1, J4_2, J4_3), and comparing them to the results from J4, it is obvious that the mechanical performance worsened significantly. J4 reached an average UTL of 3414.17 $\pm$ 317.15 N, and all its specimens had a UTL higher than 3000 N. No specimen from any of the three repetition joints reached these results, only averaging a UTL result of 2789.49 ± 207.90 N. This represents an 18.3% reduction in average mechanical performance, for the same set of parameters. Given the significant reduction, the optimal joints' results will be analysed in comparison to these last results and not with the first, as these results were obtained from joints produced in more similar conditions.

Looking at the results, it is noticeable that the difference between two specimens of the same joint is minimal for all joints except OPT3, which is also the joint with the poorest mechanical performance. Considering all the optimal specimens, from the three joints, the average UTL experienced was 2645.24 ± 232.14 N. Even though these results were not superior to the repetition joints, they were very close, with only a 5.2% reduction. If the results from the joint OPT3 were to be disregarded, due to their discrepancy from the rest of the specimens, only a 1.27% reduction would be seen, making the difference between the optimal joints and the repetition joints negligible.

Regarding the displacement results, the observations and conclusions were the same as previous ones, presented in Section 4.3. Looking at Figure 4.28, and recalling the diagram from Figure 4.11, as before, all specimens fractured fractured in accordance with Mode A.

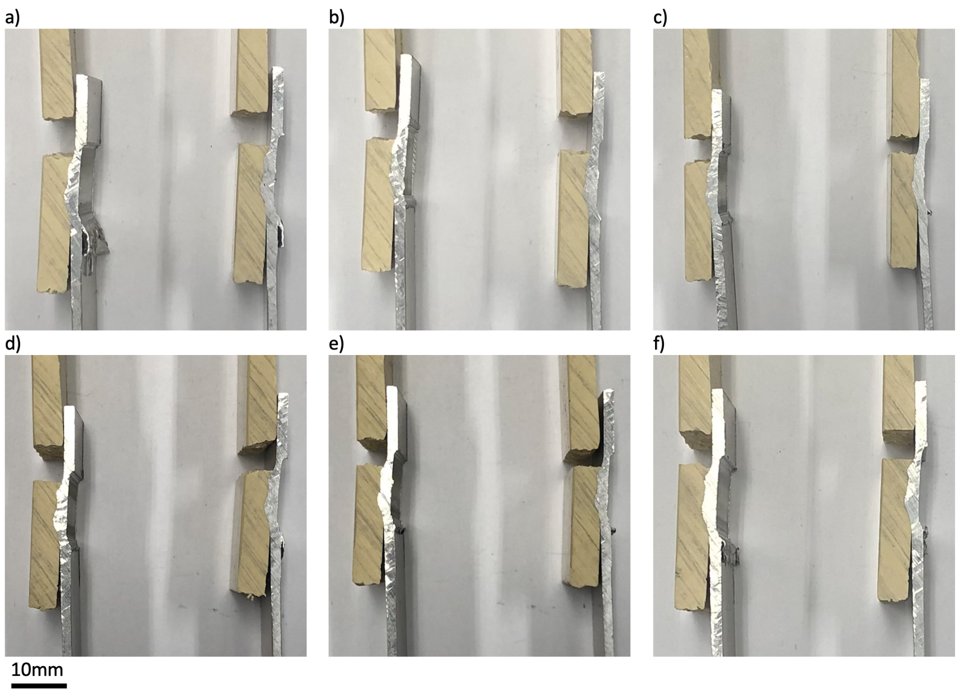

Figure 4.28: Cross section of the specimens from the optimization joints a) OPT1, b) OPT2, c) OPT3, d) J4_1, e) J4_2, f) J4_3.

Following Method 2 - Tensile Stress + Secondary Bending Moment's Induced Stress, introduced in Subsection 4.3, the local tensile strength was calculated, as well as the bending factor and the joint efficiency, and the results are displayed in Table 4.11.

From the numerical model introduced in Method 2, the secondary bending moment for the optimal joints was found to be 3.61 Nm, and for the repetition joints 3.74 Nm. As expected, since these joints had a shortcoming performance in comparison to J4, the overall local strength, and correspondent joint efficiency were also lower. However, even after being produced in worse conditions, due to the low ambient temperature, their results surpass the overall average joint performance among the fifteen joints. Comparing now the optimal joints with the repetition joints, a small reduction is observable when it comes to joint efficiency. This result was expected but the difference between them is marginal, with the efficiency dropping only 3.04%.

Table 4.11: Average local strength, calculated through the Tensile Stress + Secondary Bending Moment's Induced Stress, for the optimization joints.

	Avg. UTL [N]	M_{SB}**[Nm]**	σ_T **[MPa]**	σ_{SBM} **[MPa]**	σ_{Local} **[MPa]**	k_b	**Eff. [%]**
OPT1 **OPT2** **OPT3**	2645.24	3.61	21.16	34.67	55.83	1.64	69.78
J4_1 **J4_2** **J4_3**	2789.49	3.74	22.32	35.94	58.26	1.61	72.82

In summary, and as expected, the optimized joints did achieve, on average, a better mechanical result than the average of the fifteen original joints. However, the repetition joints were expected to perform as well as J4, and this was not the case. Not only were they worse than J4, but the optimal joints did not surpass them either. From these observations, some notes can be taken. First, more specimens could have been used to try and certain if indeed the optimal joints were worse than the repetition joints, or if by increasing the samples under study, their difference would be mitigated. Secondly, and recalling the response surface from Figure 4.24 e), the optimal joints were defined by parameters on the narrower point of the saddle-like surface, a region characterized by a high sensitivity. This means that even though they are statistically optimal, according to the model, a slight deviation from the model could generate a significant worsening of the output. Lastly, differences in the manufacturing of the joints, exacerbated by the different months of production, could have had a larger impact on the quality of the joints, than the one perceived. In the future, the outside conditions, namely the ambient temperature, should be monitored and if possible controlled, to try and mitigate their impact on the quality of the FSW joints.

Chapter 5

Conclusions

5.1 Achievements

This thesis utilized a Central Composite Design of Experiments to analyze the thermo-mechanical properties of the friction stir welded joints between AA6082-T6 and NORYL^{TM} GFN2, configured in an overlap arrangement. The conclusions were found as follows:

- The interval of parameters chosen was found to produce soundly bonded joints, reinforcing the viability of this process to produce dissimilar joints, between aluminum and NORYL^{TM}.
- All joints show a very good surface quality with negligible polymeric extrusion, contained disruption of the aluminum material to the initial weld spot, a good to excellent range of weld line smoothness, and minimal metallic flash defect. All the joints' cross sections are characterized by a double concavity shown to enhance the mechanical interlocking of the material without disrupting material continuity.
- Thermal history confirmed the tendency for higher temperatures on the advancing side, due to increased plastic material flow, and a tendency for the processing temperature to be between the softening and melting temperatures of the polymeric material, allowing for the proper development of bonding mechanisms without thermally compromising the material.
- Quasi-static tensile tests showed UTL results ranging from 1698.20 ± 17.29 N to 3414.17 ± 317.15 N. Using a FEM model, to replicate the test, provided the secondary bending moment generated which ranged from 2.47 Nm to 4.20 Nm. On average the stress caused by the M$_{S}B$ amounted to 63% of the total stress of the joint. Bending factor results ranged from 1.48 to 1.75, with smaller bending factors being associated with larger UTL results due to larger tensile stresses. Considering both tensile and secondary bending moment's induced stress, the joint efficiency ranged from 46.62% to 84.55%.
- Scanning electron microscopy showed a strong connection between larger effective joining areas and increased joint strength, as well as how micro-gaps in the interface are detrimental to the performance of the joints. Energy dispersive spectroscopy showed no evidence of the formation

of an aluminum oxide layer, in the interface.

- Hardness profiles were similar between the joints. The aluminum measurements formed the characteristic W-shaped profile, with a rapid decrease approaching the TMAZ followed by a slight increase in the SZ and a decrease in the nugget location. No significant variation was detected in the polymer's measurement, and no correlation was found between the harness profiles and the mechanical strength of the joint.
- Statistical analysis determined mathematical models to predict both the processing temperature and the mechanical strength (UTL), as a function of the processing parameters, rotational speed, welding speed, and tool tilt angle. In particular, the UTL model showed a high contribution of the tilt angle and the two-way interaction between the welding speed and the tilt angle. Due to the narrow saddle-like profile of the response surface reaching the optimal values, output volatility is expected when trying to obtain optimal values.
- To maximize the mechanical strength, the UTL model generated the optimal set of parameters: rotational speed of 1136 rpm, a welding speed of 154 mm/min, and a tilt angle of 1.7° . This solution did not reach the predicted outcome, with the average joint UTL only reaching 2645.24 $\pm$ 232.14 N. The joint strength was largely impacted by the uncontrolled variation of the ambient temperature. The temperature decreased between 15° C and 25° C, from the ambient temperature at the moment of initial production, which generated the UTL model.

5.2 Future Work

From the experimental work developed and the analysis performed some aspects were found to need improvement as well as further studies:

- Characterize the fatigue behaviour of the dissimilar joints, perform static and dynamic studies at different service temperatures, and study the mechanical behaviour of the joint at different deformation rates.
- Design different FSW tools and study their impact on the dissimilar metal-polymer joints, and produce dissimilar FSW joints with different material thicknesses to better understand the heat transfer between BMs.
- Measure and analyse the impact of the ambient conditions, namely the room temperature, on the surface quality and mechanical strength of the joints.
- Create a digital twin that can accurately replicate the production procedure to minimize the number of experimental procedures necessary.
- Develop a new clamping system, with a different geometry or material, which does not promote heat conductivity to the outside of the weld line.
- Study the impact of the dwell time on the quality of the joint, to minimize material waste and optimize the procedure in the initial phase.

References

[1] C. G. Dalwadi, A. R. Patel, J. M. Kapopara, D. J. Kotadiya, N. D. Patel, and H. G. Rana. Examination of mechanical properties for dissimilar friction stir welded joint of al alloy (aa-6061) to pmma (acrylic). volume 5, pages 4761–4765. Elsevier Ltd, 2018.

[2] A. R. Patel, D. J. Kotadiya, J. M. Kapopara, C. G. Dalwadi, N. P. Patel, and H. G. Rana. Investigation of mechanical properties for hybrid joint of aluminium to polymer using friction stir welding (fsw). volume 5, pages 4242–4249. Elsevier Ltd, 2018.

[3] W. Ratanathavorn and A. Melander. Dissimilar joining between aluminium alloy (aa 6111) and thermoplastics using friction stir welding. *Science and Technology of Welding and Joining*, 20: 222–228, 3 2015.

[4] Y. Yan, Y. Shen, H. Lei, J. Zhuang, and J. Li. Friction lap welding aa6061 alloy and gfr nylon: Influence of welding parameters and groove features on joint morphology and mechanical property. *Journal of Materials Processing Technology*, 278, 4 2020.

[5] H. A. Derazkola and M. Elyasi. The influence of process parameters in friction stir welding of al-mg alloy and polycarbonate. *Journal of Manufacturing Processes*, 35:88–98, 10 2018.

[6] H. A. Derazkola, R. K. Fard, and F. Khodabakhshi. Effects of processing parameters on the characteristics of dissimilar friction-stir-welded joints between aa5058 aluminum alloy and pmma polymer. *Welding in the World*, 62:117–130, 1 2018.

[7] H. Shahmiri, M. Movahedi, and A. H. Kokabi. Friction stir lap joining of aluminium alloy to polypropylene sheets. *Science and Technology of Welding and Joining*, 22:120–126, 2 2017.

[8] Y. Huang, X. Meng, Y. Wang, Y. Xie, and L. Zhou. Joining of aluminum alloy and polymer via friction stir lap welding. *Journal of Materials Processing Technology*, 257:148–154, 7 2018.

[9] F. Khodabakhshi, M. Haghshenas, S. Sahraeinejad, J. Chen, B. Shalchi, J. Li, and A. P. Gerlich. Microstructure-property characterization of a friction-stir welded joint between aa5059 aluminum alloy and high density polyethylene. *Materials Characterization*, 98:73–82, 2014.

[10] A. N. Correia, P. A. M. Santos, D. F. O. Braga, R. Baptista, and V. Infante. Effects of friction stir welding process control and tool penetration on mechanical strength and morphology of dissimilar aluminum-to-polymer joints. *Journal of Manufacturing and Materials Processing*, 7:106, 6 2023.

[11] J. Guo. *Handbook of Manufacturing Engineering and Technology*. Springer-Verlag London Ltd, 2015.

[12] M. Haghshenas and F. Khodabakhshi. Dissimilar friction-stir welding of aluminum and polymer: a review. *International Journal of Advanced Manufacturing Technology*, 104:333–358, 9 2019.

[13] T. Yahaba, M. Sayama, T. Kobayashi, and T. Kato. Development of friction stir welding technology for subframe for fuel cell system. 47:19–27, 5 2009.

[14] D. Gera, B. Fu, U. F. Suhuddin, A. Plaine, N. Alcantara, J. F. dos Santos, and B. Klusemann. Microstructure, mechanical and functional properties of refill friction stir spot welds on multilayered aluminum foils for battery application. *Journal of Materials Research and Technology*, 13:2272–2286, 7 2021. ISSN 22387854. doi: 10.1016/j.jmrt.2021.06.017.

[15] V. Patel, J. D. Backer, H. Hindsefelt, M. Igestrand, S. Azimi, J. Andersson, and J. Säll. High speed friction stir welding of aa6063-t6 alloy in lightweight battery trays for ev industry: Influence of tool rotation speeds. *Materials Letters*, 318, 7 2022.

[16] S. Kang, J. Kim, Y. Jang, and K. Lee. Welding deformation analysis, using an inherent strain method for friction stir welded electric vehicle aluminum battery housing, considering productivity. *Applied Sciences (Switzerland)*, 9, 9 2019.

[17] E. E. Agency. Decarbonising road transport - the role of vehicles, fuels and transport demand, 2022.

[18] E. Comission. Sustainable and smart mobility strategy – putting european transport on track for the future, 2020.

[19] R. Sacchi, C. Bauer, B. Cox, and C. Mutel. When, where and how can the electrification of passenger cars reduce greenhouse gas emissions? *Renewable and Sustainable Energy Reviews*, 162, 7 2022.

[20] A. Wanitschke and S. Hoffmann. Are battery electric vehicles the future? an uncertainty comparison with hydrogen and combustion engines. *Environmental Innovation and Societal Transitions*, 35:509–523, 6 2020.

[21] S. Chakraborty, S. K. Dash, R. M. Elavarasan, A. Kaur, D. Elangovan, S. T. Meraj, P. Kasinathan, and Z. Said. Hydrogen energy as future of sustainable mobility. *Frontiers in Energy Research*, 10, 5 2022.

[22] H. Nazir, N. Muthuswamy, C. Louis, S. Jose, J. Prakash, M. E. Buan, C. Flox, S. Chavan, X. Shi, P. Kauranen, T. Kallio, G. Maia, K. Tammeveski, N. Lymperopoulos, E. Carcadea, E. Veziroglu, A. Iranzo, and A. M. Kannan. Is the h2 economy realizable in the foreseeable future? part iii: H2 usage technologies, applications, and challenges and opportunities. *International Journal of Hydrogen Energy*, 45:28217–28239, 10 2020.

[23] M. A. Aminudin, S. K. Kamarudin, B. H. Lim, E. H. Majilan, M. S. Masdar, and N. Shaari. An overview: Current progress on hydrogen fuel cell vehicles. *International Journal of Hydrogen Energy*, 48:4371–4388, 2 2023.

[24] O. Bethoux. Hydrogen fuel cell road vehicles: State of the art and perspectives. *Energies*, 13, 11 2020.

[25] A. M. Andwari, A. Pesiridis, S. Rajoo, R. Martinez-Botas, and V. Esfahanian. A review of battery electric vehicle technology and readiness levels. *Renewable and Sustainable Energy Reviews*, 78:414–430, 2017.

[26] C. Cunanan, M. K. Tran, Y. Lee, S. Kwok, V. Leung, and M. Fowler. A review of heavy-duty vehicle powertrain technologies: Diesel engine vehicles, battery electric vehicles, and hydrogen fuel cell electric vehicles. *Clean Technologies*, 3:474–489, 6 2021.

[27] F. Danzi, R. M. Salgado, J. E. Oliveira, A. Arteiro, P. P. Camanho, and M. H. Braga. Structural batteries: A review. *Molecules*, 26, 4 2021.

[28] X. Zhang, Z. Li, L. Luo, Y. Fan, and Z. Du. A review on thermal management of lithium-ion batteries for electric vehicles. *Energy*, 238, 1 2022.

[29] D. M. Weragoda, G. Tian, A. Burkitbayev, K. H. Lo, and T. Zhang. A comprehensive review on heat pipe based battery thermal management systems. *Applied Thermal Engineering*, 224, 4 2023.

[30] M. C. Massaro, R. Biga, A. Kolisnichenko, P. Marocco, A. H. A. Monteverde, and M. Santarelli. Potential and technical challenges of on-board hydrogen storage technologies coupled with fuel cell systems for aircraft electrification. *Journal of Power Sources*, 555:232397, 2023.

[31] S. K. Dwivedi and M. Vishwakarma. Hydrogen embrittlement in different materials: A review. *International Journal of Hydrogen Energy*, 43:21603–21616, 11 2018.

[32] P. C. Okonkwo, E. M. Barhoumi, I. B. Belgacem, I. B. Mansir, M. Aliyu, W. Emori, P. C. Uzoma, W. H. Beitelmal, E. Akyüz, A. B. Radwan, and R. A. Shakoor. A focused review of the hydrogen storage tank embrittlement mechanism process. *International Journal of Hydrogen Energy*, 48: 12935–12948, 4 2023.

[33] P. Gong, A. Turk, J. Nutter, F. Yu, B. Wynne, P. R.-D. del Castillo, and W. M. Rainforth. Hydrogen embrittlement mechanisms in advanced high strength steel. *Acta Materialia*, 223:117488, 2022.

[34] Y. Manoharan, S. E. Hosseini, B. Butler, H. Alzhahrani, B. T. F. Senior, T. Ashuri, and J. Krohn. Hydrogen fuel cell vehicles; current status and future prospect. *Applied Sciences (Switzerland)*, 9, 6 2019.

[35] A. N. Correia, D. F. Braga, P. M. Moreira, and V. Infante. Review on dissimilar structures joints failure. *Engineering Failure Analysis*, 129, 11 2021.

[36] A. J. Kinloch. *Adhesion and Adhesives*. Springer Dordrecht, 1987.

[37] E. M. Petrie. *Handbook of adhesives and sealants*. McGraw-Hill, 2000.

[38] R. D. Adams. *Adhesive Bonding*. Woodhead Publishing, 2021.

[39] L. F. da Silva, A. Öchsner, and R. D. Adams. *Introduction to adhesive bonding technology*. Springer International Publishing, 2018.

[40] R. W. Messler. *Joining of Materials and Structures*. Elsevier Inc., 2004.

[41] F. Delzendehrooy, A. Akhavan-Safar, A. Q. Barbosa, R. Beygi, D. Cardoso, R. J. Carbas, E. A. Marques, and L. F. da Silva. A comprehensive review on structural joining techniques in the marine industry. *Composite Structures*, 289, 6 2022.

[42] P. Kah, R. Suoranta, J. Martikainen, and C. Magnus. Techniques for joining dissimilar materials: Metals and polymers. *Reviews on Advanced Materials Science*, 36:152–164, 2014.

[43] J. A. Speck. *Mechanical Fastening, Joining, and Assembly*. 2015.

[44] R. W. Messler. *PRINCIPLES OF WELDING Processes, Physics, Chemistry, and Metallurgy*. WILEY-VCH Verlag GmbH Co. KGaA, 2004.

[45] W. M. Thomas, E. D. Nicholas, J. C. Needham, M. G. Murch, P. Temple-Smith, and C. J. Dawes. Friction stir butt welding, international patent application pct/gb92/02203, gb patent application 9125978.8, us patent 5.460.317, 1991.

[46] P. Vilaça and W. Thomas. *Friction Stir Welding Technology*, pages 85–124. 2011.

[47] V. Infante, D. F. Braga, F. Duarte, P. M. Moreira, M. D. Freitas, and P. M. D. Castro. Study of the fatigue behaviour of dissimilar aluminium joints produced by friction stir welding. volume 82, pages 310–316. Elsevier Ltd, 1 2016.

[48] M. Milčić, Z. Burzić, I. Radisavljević, T. Vuherer, D. Milčić, and V. Grabulov. Experimental investigation of fatigue properties of fsw in aa2024-t351. volume 13, pages 1977–1984. Elsevier B.V., 2018.

[49] I. Radisavljevic, A. Zivkovic, N. Radovic, and V. Grabulov. Influence of fsw parameters on formation quality and mechanical properties of al 2024-t351 butt welded joints. *Transactions of Nonferrous Metals Society of China (English Edition)*, 23:3525–3539, 12 2013.

[50] S. Rajakumar, C. Muralidharan, and V. Balasubramanian. Influence of friction stir welding process and tool parameters on strength properties of aa7075-t6 aluminium alloy joints. *Materials and Design*, 32:535–549, 2 2011.

[51] R. Jabraeili, H. R. Jafarian, R. Khajeh, N. Park, Y. Kim, A. Heidarzadeh, and A. R. Eivani. Effect of fsw process parameters on microstructure and mechanical properties of the dissimilar aa2024 al alloy and 304 stainless steel joints. *Materials Science and Engineering: A*, 814, 5 2021.

[52] Q. Zheng, X. Feng, Y. Shen, G. Huang, and P. Zhao. Dissimilar friction stir welding of 6061 al to 316 stainless steel using zn as a filler metal. *Journal of Alloys and Compounds*, 686:693–701, 11 2016.

[53] A. Yazdipour and A. Heidarzadeh. Effect of friction stir welding on microstructure and mechanical properties of dissimilar al 5083-h321 and 316l stainless steel alloy joints. *Journal of Alloys and Compounds*, 680:595–603, 9 2016.

[54] H. Bisadi, M. Tour, and A. A. The influence of process parameters on microstructure and mechanical properties of friction stir welded al 5083 alloy lap joint. *American Journal of Materials Science*, 1:93–97, 8 2012.

[55] D. Sethi, U. Acharya, S. Shekhar, and B. S. Roy. Applicability of unique scarf joint configuration in friction stir welding of aa6061-t6: Analysis of torque, force, microstructure and mechanical properties. *Defence Technology*, 18:567–582, 4 2022.

[56] J. Martin and W. Way. Novel techniques for corner joints using friction stir. *Friction stir welding and processing VI*, 179, 2011.

[57] A. N. Correia, B. M. Gaspar, G. Cipriano, D. F. O. Braga, R. Baptista, and V. Infante. Thermomechanical characterization of metal–polymer friction stir composite joints—a full factorial design of experiments. *Polymers*, 16:602, 2 2024.

[58] W. Thomas, D. Staines, I. Norris, and R. Frias. Friction stir welding tools and developments. *Weld World*, 47:10–17, 2003.

[59] F. Lambiase, H. A. Derazkola, and A. Simchi. Friction stirwelding and friction spot stir welding processes of polymers-state of the art, 5 2020.

[60] Ákos Meilinger and I. Török. The importance of friction stir welding tool. *Production Processes and Systems*, 6:25–34, 2013.

[61] Y. Huang, X. Meng, Y. Xie, L. Wan, Z. Lv, J. Cao, and J. Feng. Friction stir welding/processing of polymers and polymer matrix composites. *Composites Part A: Applied Science and Manufacturing*, 105:235–257, 2 2018.

[62] A. I. Albannai. Review the common defects in friction stir welding. *International Journal of Scientific Technology Research*, 9:318–329, 2020.

[63] T. Jene, D. Eifler, G. Wagner, and G. Dobmann. Monitoring of the friction stir welding process to describe parameter effects on joint quality. *Fraunhofer IZFP*, 52, 9 2008.

[64] R. Mishra and Z. Ma. Friction stir welding and processing. *Materials Science and Engineering: R: Reports*, 50:1–78, 2205.

[65] D. Braga. Innovative structural joining for lightweight design. 2018.

[66] S. T. Amancio-Filho and L.-A. Blaga. Joining of polymer-metal hybrid structures: Principles and applications, 2018.

[67] G. Taguchi, S. Chowdhury, and Y. Wu. *Taguchi's Quality Engineering Handbook*. 2005.

[68] D. C. Montgomery. *Design and analysis of experiments*. Eighth edition edition, 2012.

[69] G. E. P. Box and K. B. Wilson. On the experimental attainment of optimum conditions. *Journal of the Royal Statistical Society SERIES B (METHODOLOGICAL)*, XIII:1–38, 1951.

[70] Minitab. What are response surface designs, central composite designs, and box-behnken designs?, . URL https://support.minitab.com/en-us/minitab/21/help-and-how-to/statistical-modeling/doe/supporting-topics/response-surface-designs/response-surface-central-composite-and-box-behnken-designs/#:~:text=Central%20composite%20designs%20are%20a,%2D%20and%20second%2Dorder%20terms. 24th April 2024.

[71] R. H. Myers, D. C. Montgomery, and C. M. Anderson-Cook. *RESPONSE SURFACE METHODOLOGY - Process and Product Optimization Using Designed Experiments*. Forth edition edition, 2016.

[72] A. Dean, D. Voss, and D. Draguljić. *Response Surface Methodology*. 2017.

[73] A. N. Correia, P. A. Santos, D. F. Braga, G. P. Cipriano, P. M. Moreira, and V. Infante. Effects of processing temperature on failure mechanisms of dissimilar aluminum-to-polymer joints produced by friction stir welding. *Engineering Failure Analysis*, 146, 4 2023.

[74] F. Baratzadeh, E. Boldsaikhan, R. Nair, D. Burford, and H. Lankarani. Investigation of mechanical properties of aa6082-t6/aa6063-t6 friction stir lap welds. *Journal of Advanced Joining Processes*, 1, 3 2020.

[75] L. P. Troeger and E. A. Starke. Microstructural and mechanical characterization of a superplastic 6xxx aluminum alloy, 2000.

[76] M. Ericsson and R. Sandström. Influence of welding speed on the fatigue of friction stir welds, and comparison with mig and tig. *International Journal of Fatigue*, 25:1379–1387, 12 2003.

[77] P. M. Moreira, T. Santos, S. M. Tavares, V. Richter-Trummer, P. Vilaça, and P. M. de Castro. Mechanical and metallurgical characterization of friction stir welding joints of aa6061-t6 with aa6082-t6. *Materials and Design*, 30:180–187, 1 2009.

[78] PHT. Noryl gfn2 801. URL https://www.pht-plastic.com/choice-of-materials/ppe-hips-polyphenylene-ether-1/ppe-gf20-nat-noryl-gfn2-801/. 11th April 2024.

[79] SABIC. Noryl resin gfn2, 2020. URL https://www.sabic.com/en/products/specialties/noryl-resins/noryl-resin. 11th April 2024.

[80] F. M. S. Dias. Dissimilar materials joining through friction stir welding. pages 1–106, 2022.

[81] P. A. M. dos Santos. Caracterização mecânica de juntas dissimilares alumínio-compósito produzidas através do processo de soldadura por fricção linear. pages 1–126, 2022.

[82] J. Felgueiras. Máquina fsw – manual de utilização da hmi, 2022.

[83] R. Nandan, T. DebRoy, and H. K. Bhadeshia. Recent advances in friction-stir welding - process, weldment structure and properties, 8 2008.

[84] E. G. Cole, A. Fehrenbacher, N. A. Duffie, M. R. Zinn, F. E. Pfefferkorn, and N. J. Ferrier. Weld temperature effects during friction stir welding of dissimilar aluminum alloys 6061-t6 and 7075-t6. *International Journal of Advanced Manufacturing Technology*, 71:643–652, 3 2014.

[85] A. C. Silva, J. D. Backer, and G. Bolmsjö. Temperature measurements during friction stir welding. *International Journal of Advanced Manufacturing Technology*, 88:2899–2908, 2 2017.

[86] M. Li, X. Xiong, S. Ji, W. Hu, and Y. Yue. Achieving high-quality metal to polymer-matrix composites joint via top-thermic solid-state lap joining. *Composites Part B: Engineering*, 219, 8 2021.

[87] J. Schijve, G. Campoli, and A. Monaco. Fatigue of structures and secondary bending in structural elements. *International Journal of Fatigue*, 31:1111–1123, 7 2009.

[88] J. Ekh, J. Schön, and L. G. Melin. Secondary bending in multi fastener, composite-to-aluminium single shear lap joints. *Composites Part B: Engineering*, 36:195–208, 2005.

[89] M. Skorupa, A. Korbel, A. Skorupa, and T. Machniewicz. Observations and analyses of secondary bending for riveted lap joints. *International Journal of Fatigue*, 72:1–10, 2015.

[90] SABIC. Noryl* resin - modified ppe-ps. URL `https://www.sabic.com/en/products/specialties/noryl-resins/noryl-resin`. 11th April 2024.

[91] G. R. Johnson. Fracture characteristics of three metals subjected to various strains, strain rates, temperatures and pressures, 1985.

[92] M. Rodríguez-Millán, A. Vaz-Romero, A. Rusinek, J. A. Rodríguez-Martínez, and A. Arias. Experimental study on the perforation process of 5754-h111 and 6082-t6 aluminium plates subjected to normal impact by conical, hemispherical and blunt projectiles. *Experimental Mechanics*, 54: 729–742, 2014.

[93] M. Rodriguez-Millan, D. Garcia-Gonzalez, A. Rusinek, and A. Arias. Influence of stress state on the mechanical impact and deformation behaviors of aluminum alloys. *Metals*, 8, 7 2018.

[94] M. Li, X. Xiong, S. Ji, W. Hu, and Y. Yue. Achieving high-quality metal to polymer-matrix composites joint via top-thermic solid-state lap joining. *Composites Part B: Engineering*, 219, 8 2021.

[95] A. Tongne, M. Jahazi, E. Feulvarch, and C. Desrayaud. Banded structures in friction stir welded al alloys. *Journal of Materials Processing Technology*, 221:269–278, 2015.

[96] F. Lambiase, S. I. Scipioni, C. J. Lee, D. C. Ko, and F. Liu. A state-of-the-art review on advanced joining processes for metal-composite and metal-polymer hybrid structures. *Materials*, 14, 4 2021.

[97] F. C. Liu, P. Dong, and X. Pei. A high-speed metal-to-polymer direct joining technique and underlying bonding mechanisms. *Journal of Materials Processing Technology*, 280, 6 2020.

[98] M. I. Costa, D. M. Rodrigues, and C. Leitão. Analysis of aa 6082-t6 welds strength mismatch: stress versus hardness relationships. *International Journal of Advanced Manufacturing Technology*, 79:719–727, 7 2015.

[99] Minitab. Perform stepwise regression for fit regression model, . URL https://support.minitab.com/en-us/minitab/help-and-how-to/statistical-modeling/regression/how-to/fit-regression-model/perform-the-analysis/perform-stepwise-regression/. 24th April 2024.

[100] Minitab. Model summary table for fit regression model, . URL https://support.minitab.com/en-us/minitab/help-and-how-to/statistical-modeling/regression/how-to/fit-regression-model/interpret-the-results/all-statistics-and-graphs/model-summary-table/. 24th April 2024.

Annex A

Technical Drawing - Specimen Cutting

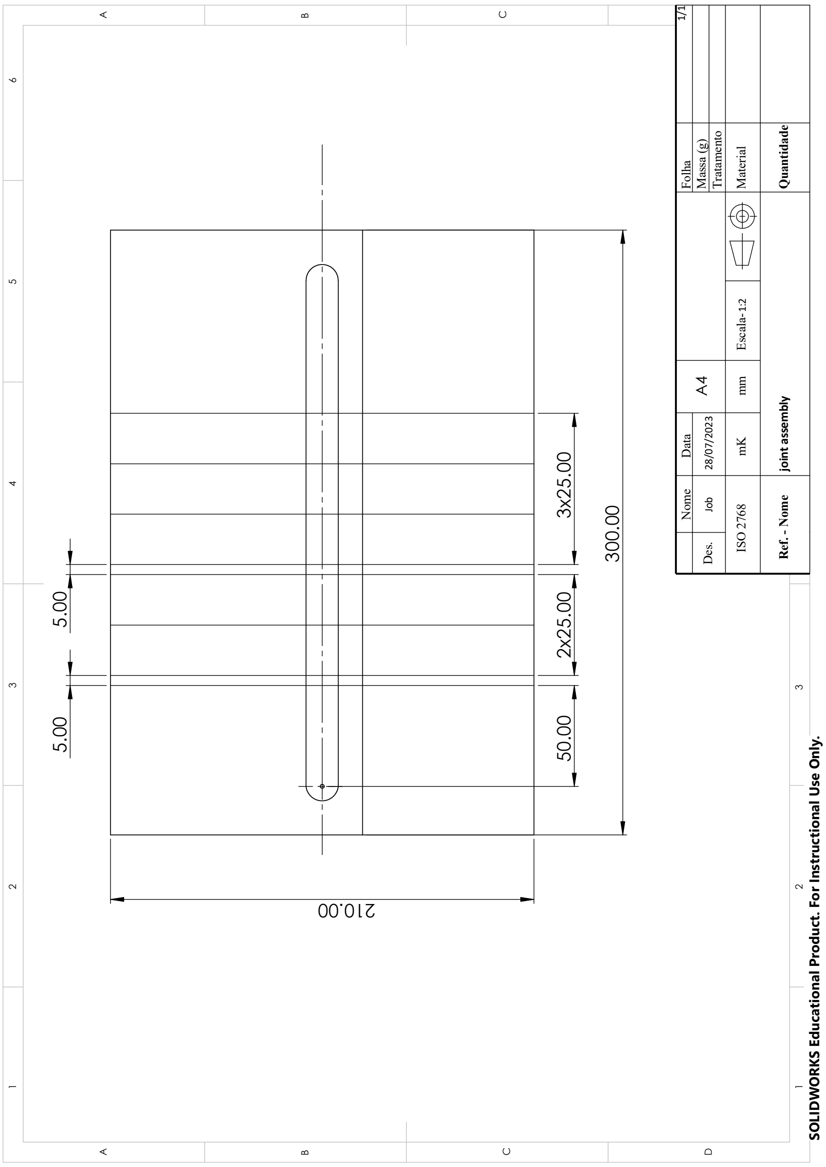

Figure A.1: Technical Drawing - Specimen Cutting

Annex B

Temperature Distribution Profiles

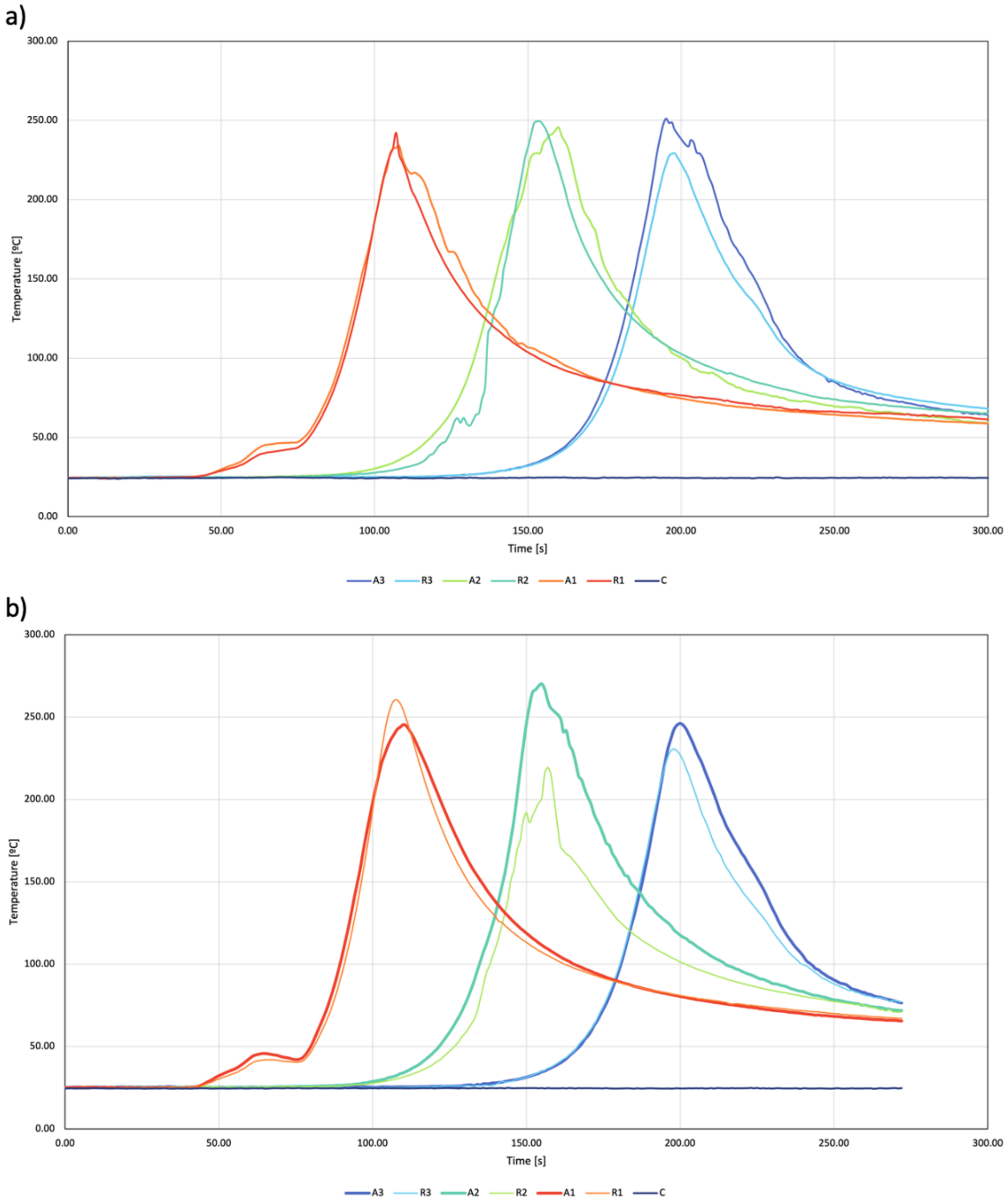

Figure B.1: Temperature distribution measured by the thermocouples during FSW process a) J1, b) J2.

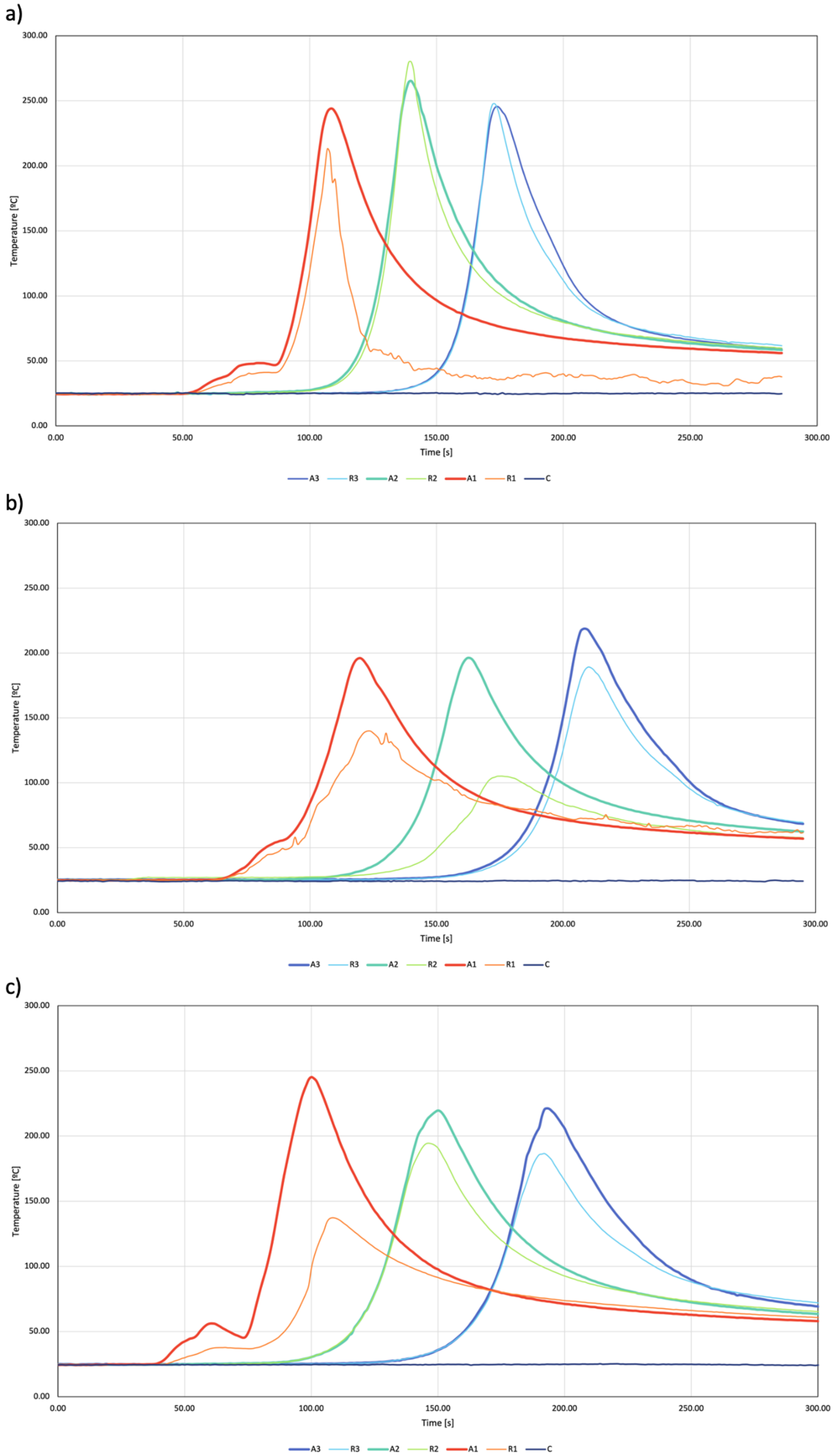

Figure B.2: Temperature distribution measured by the thermocouples during FSW process of a) J4, b) J5, c) J6.

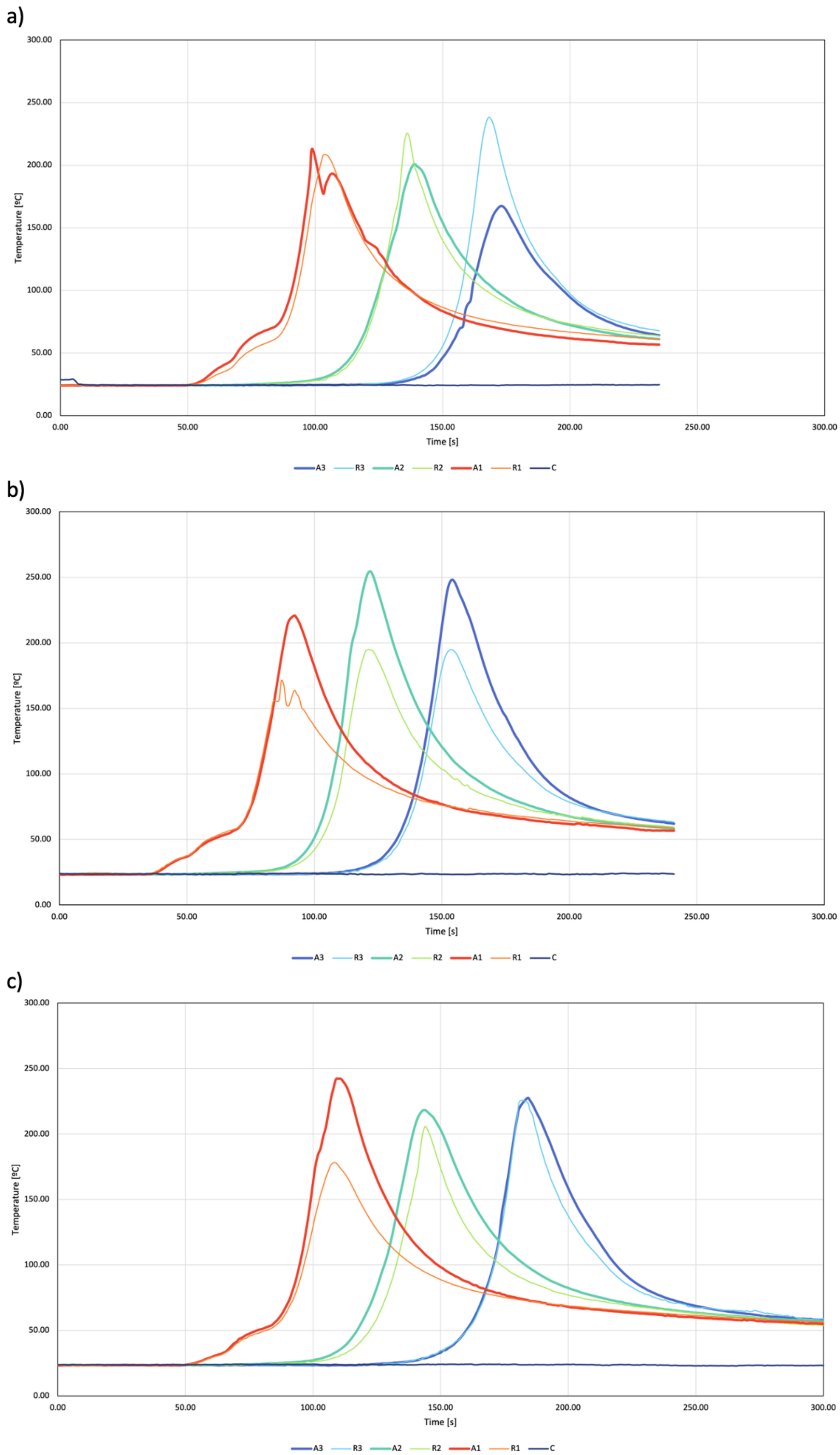

Figure B.3: Temperature distribution measured by the thermocouples during FSW process of a) J7, b) J8, c) J9.

a)

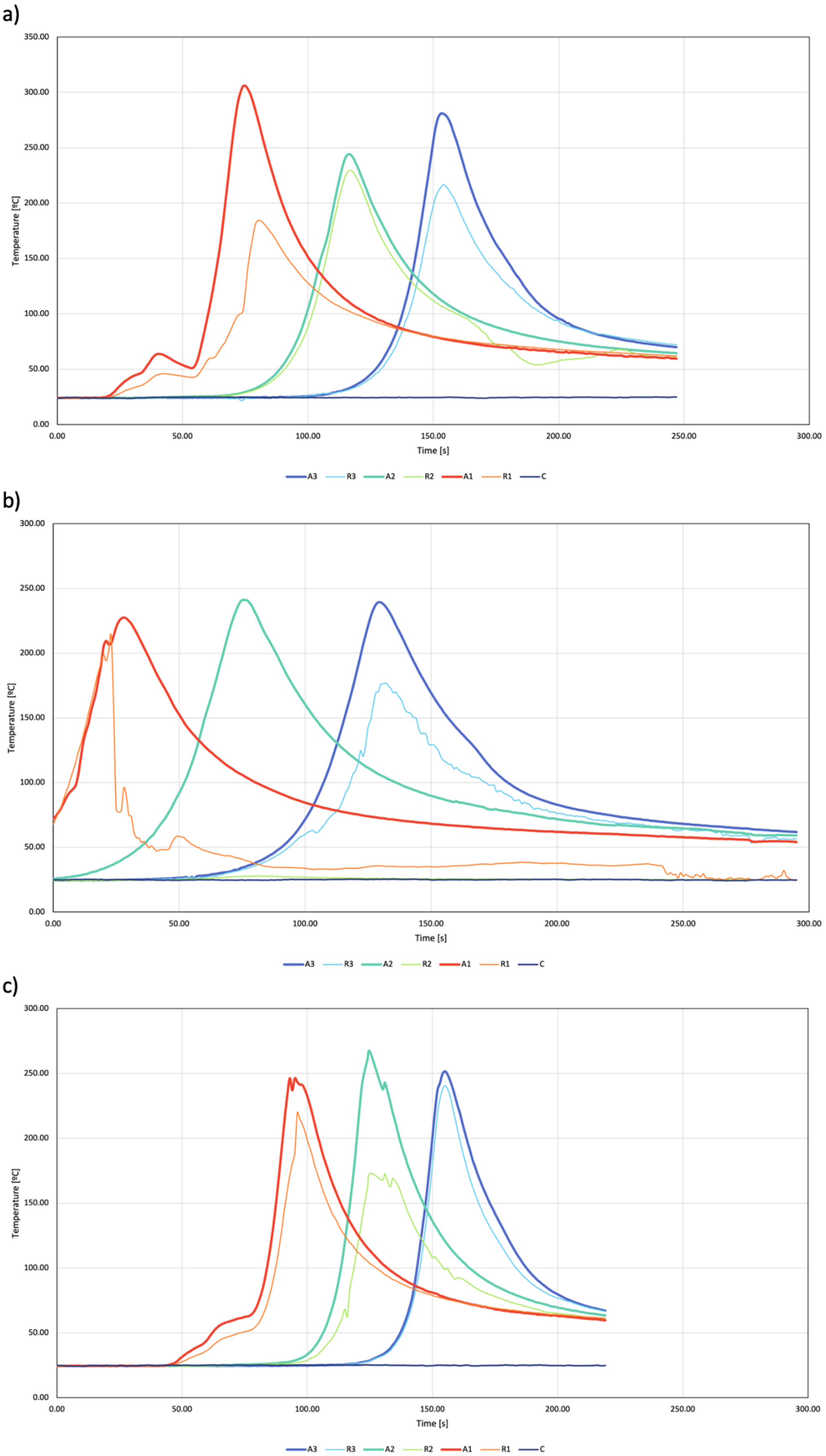

Figure B.4: Temperature distribution measured by the thermocouples during FSW process of a) J10, b) J11, c) J12.

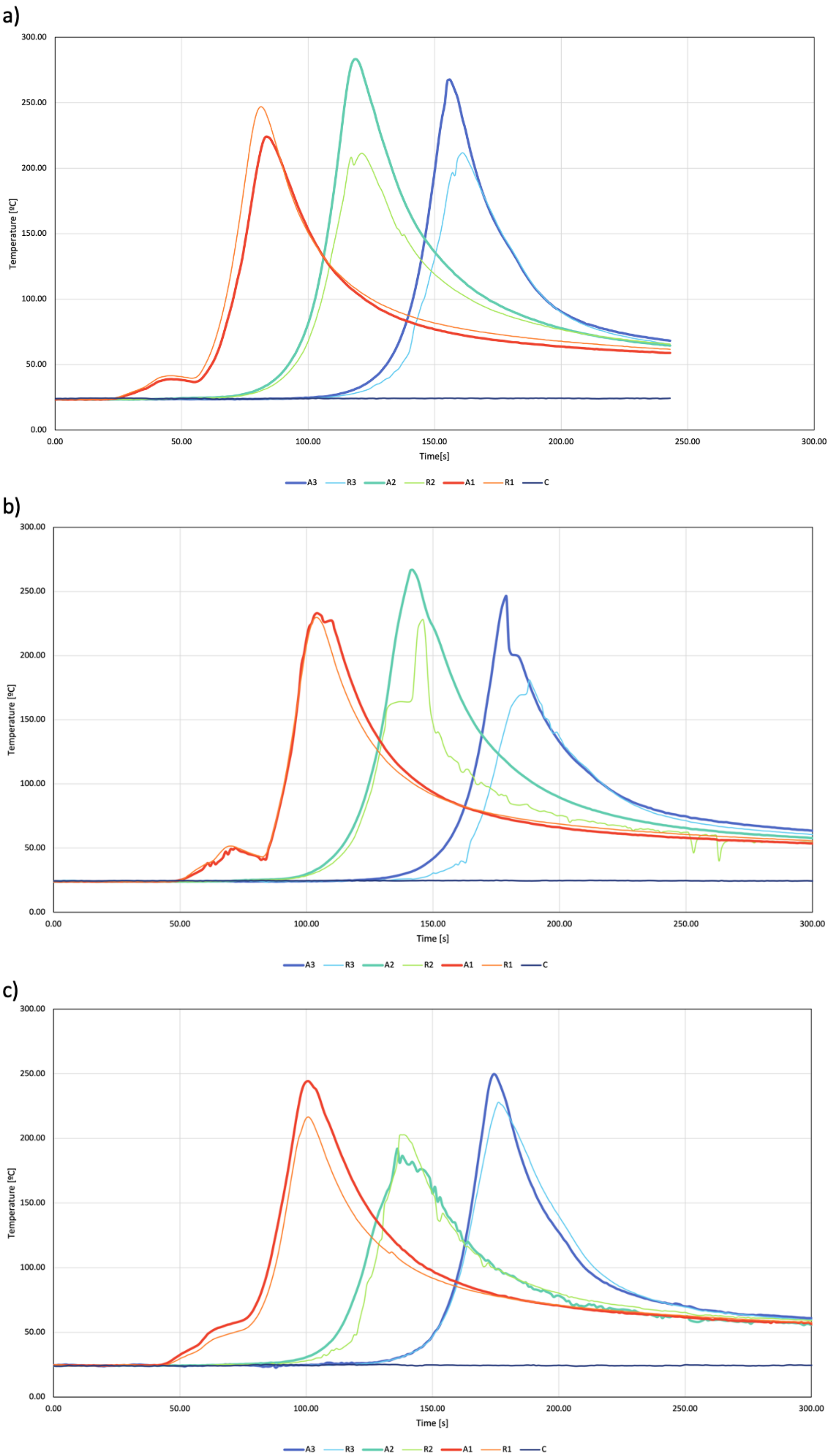

Figure B.5: Temperature distribution measured by the thermocouples during FSW process of a) J13, b) J14, c) J15.

Annex C

Energy Dispersive Spectroscopy - Reports

J6 - G

1. Region

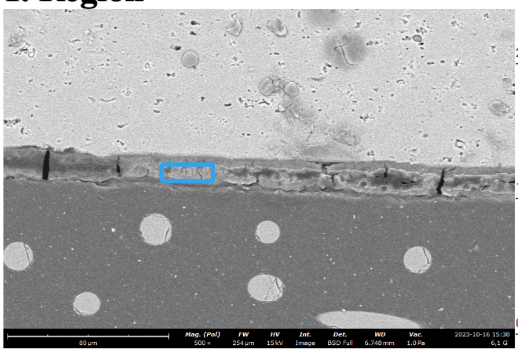

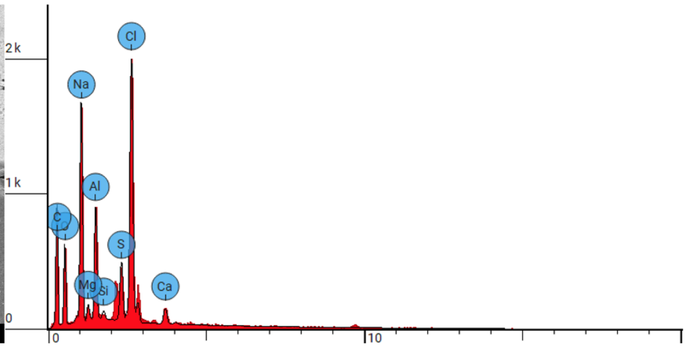

FW: 254 µm, Mode: 15 kV - Image, Detector: BSD Full, Time: 10/16/23 3:38 PM

	Element Number	Element Symbol	Element Name	Atomic Conc.	Weight Conc.
	6	C	Carbon	60.820	42.400
	8	O	Oxygen	13.028	12.100
	11	Na	Sodium	8.164	10.900
	12	Mg	Magnesium	0.425	0.600
	13	Al	Aluminum	3.896	6.100
	14	Si	Silicon	0.184	0.300
	16	S	Sulfur	1.880	3.500
	17	Cl	Chlorine	10.785	22.200
	20	Ca	Calcium	0.817	1.900

92 071 counts in 0:00:45 (2 036 c/s)

Figure C.1: Picture of the EDS report of J6, position G - interface.

J4 - D

1. Spot

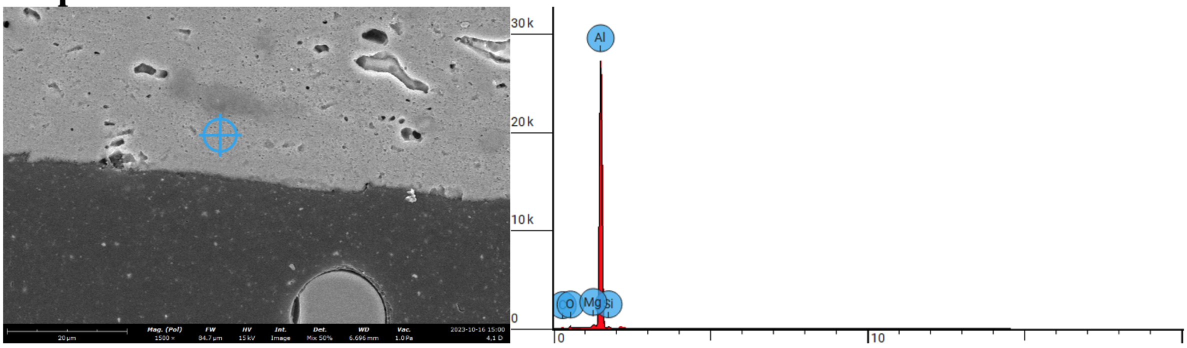

FW: 85 µm, Mode: 15 kV - Image, Detector: Mix 50%, Time: 10/16/23 3:00 PM

	Element Number	Element Symbol	Element Name	Atomic Conc.	Weight Conc.
	6	C	Carbon	2.624	1.199
	8	O	Oxygen	2.626	1.598
	12	Mg	Magnesium	0.432	0.400
	13	Al	Aluminum	93.477	95.904
	14	Si	Silicon	0.841	0.899

267 717 counts in 0:00:45 (5 923 c/s)

2. Spot

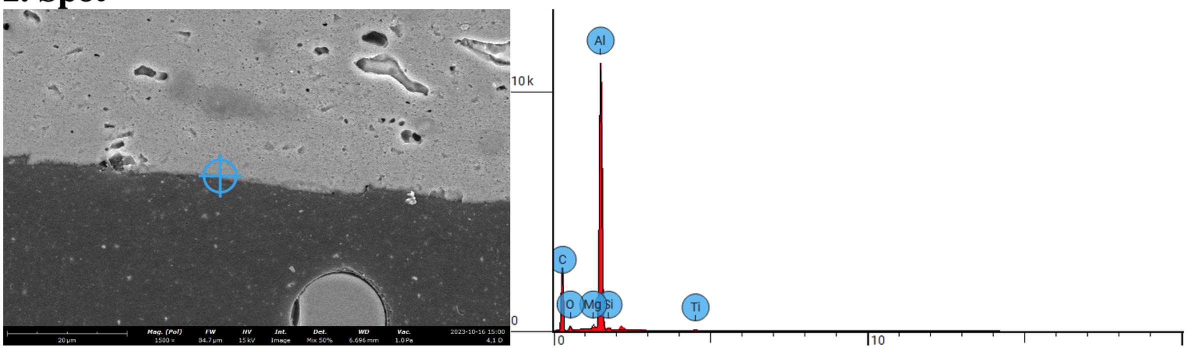

FW: 85 µm, Mode: 15 kV - Image, Detector: Mix 50%, Time: 10/16/23 3:00 PM

	Element Number	Element Symbol	Element Name	Atomic Conc.	Weight Conc.
	6	C	Carbon	71.216	53.053
	8	O	Oxygen	2.118	2.102
	12	Mg	Magnesium	0.265	0.400
	13	Al	Aluminum	25.969	43.443
	14	Si	Silicon	0.230	0.400
	22	Ti	Titanium	0.202	0.601

133 729 counts in 0:00:33 (3 935 c/s)

Figure C.2: Picture of the EDS report of J4, position D - aluminum and interface.

3. Spot

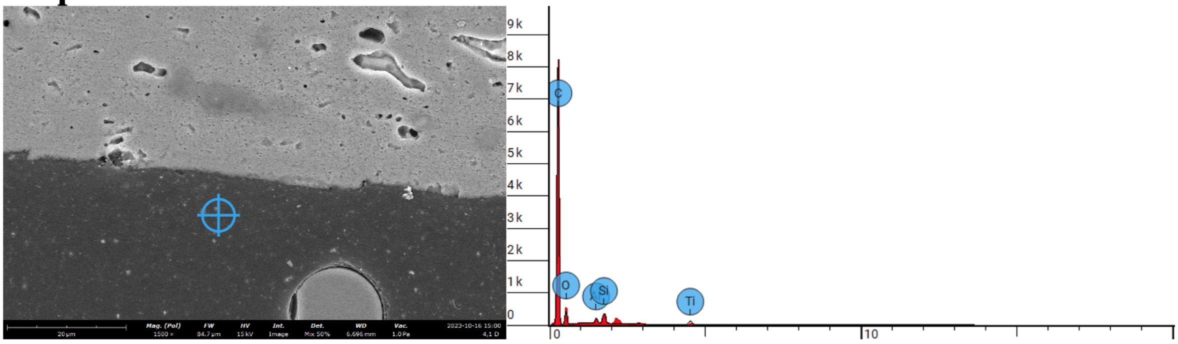

FW: 85 µm, Mode: 15 kV - Image, Detector: Mix 50%, Time: 10/16/23 3:00 PM

	Element Number	Element Symbol	Element Name	Atomic Conc.	Weight Conc.
	6	C	Carbon	87.678	81.718
	8	O	Oxygen	10.138	12.587
	13	Al	Aluminum	0.668	1.399
	14	Si	Silicon	0.871	1.898
	22	Ti	Titanium	0.645	2.398

75 615 counts in 0:00:41 (1 817 c/s)

Figure C.3: Picture of the EDS report of J4, position D - NORYL™.

J7 - C

1. Region

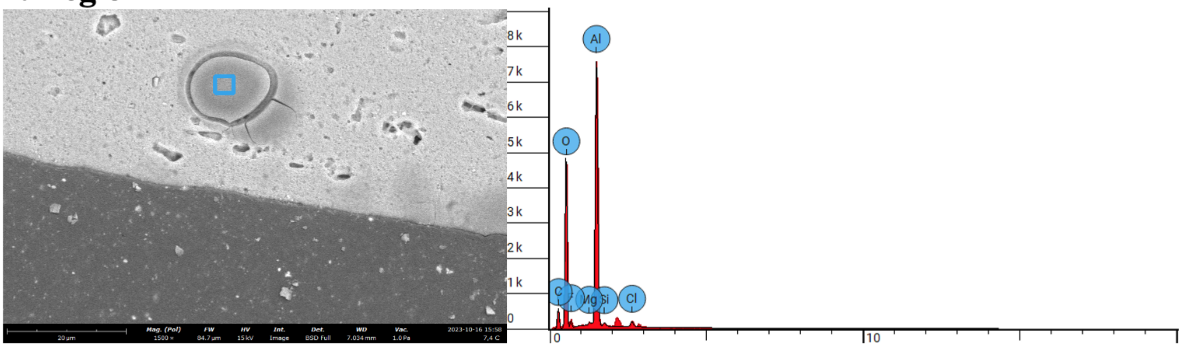

FW: 85 µm, Mode: 15 kV - Image, Detector: BSD Full, Time: 10/16/23 3:58 PM

	Element Number	Element Symbol	Element Name	Atomic Conc.	Weight Conc.
	6	C	Carbon	24.408	15.900
	8	O	Oxygen	43.557	37.800
	9	F	Fluorine	2.135	2.200
	12	Mg	Magnesium	0.152	0.200
	13	Al	Aluminum	28.575	41.800
	14	Si	Silicon	0.394	0.600
	17	Cl	Chlorine	0.780	1.500

134 035 counts in 0:00:45 (2 971 c/s)

Figure C.4: Picture of the EDS report of J7, position C - Keller's Reagent deposit.